ILLUMINATING STRAIN FIELDS GENERATED BY HYDRAULIC FRACTURING: FROM MODELING OF FIBER-OPTIC RESPONSE TO FRACTURE GEOMETRY INVERSION

A Dissertation

by

KILDARE GEORGE RAMOS GURJAO

Submitted to the Graduate and Professional School of
Texas A&M University
in partial fulfillment of the requirements for the degree of

DOCTOR OF PHILOSOPHY

Chair of Committee,	Eduardo Gildin
Committee Members,	Siddharth Misra
	Kan Wu
	Mark E. Everett
Head of Department,	Jeff Spath

December 2022

Major Subject: Petroleum Engineering

Copyright 2022 Kildare George Ramos Gurjao

ABSTRACT

The use of fiber-optics in reservoir surveillance can bring valuable insights to fracture geometry and fracture-hit identification, stage communication, and perforation cluster fluid distribution in hydraulic fracturing processes. However, the complexity of multiple information streams associated with realistic field data makes interpretation challenging for engineers and geoscientists. In this work, I generate distributed strain sensing (DSS)/low-frequency distributed acoustic sensing (LF-DAS) synthetic data of a cross-well fiber deployment. This data incorporates the physics governing hydraulic fracturing treatments. Forward modeling streamlines the interpretation task by exploring data richness, which has the potential to improve completion design and optimize production.

Forward modeling relies on analytical and numerical solutions. The analytical solution is developed by coupling two models: a 2D fracture (e.g., Khristianovic-Geertsma-de Klerk [KGD]) and Sneddon's induced stress. DSS is estimated using the plane strain approach that combines calculated stresses and rock properties (e.g., Young's modulus and Poisson's ratio). In turn, the numerical solution is implemented using the displacement discontinuity method (DDM) with net pressure and/or shear stress as the boundary condition. In this case, the fiber gauge length concept is incorporated deriving displacement (i.e., DDM output) in space to obtain DSS values. In both methods, LF-DAS is estimated by the differentiation of DSS in time.

My simulator models classic features present in field data including: the heart-shaped pattern from a fracture approaching the fiber, stress shadow, and fracture hits. Incorporating shear stress in simulation creates strain time histories that entail complexities beyond those observed in cases in which tensile stress is the unique failure mechanism, thus highlighting the significant impact promoted by natural fractures. Moreover, a large gauge length (i.e., popular 10 m size used in the field) can mask strain data richness, distorting intrinsic characteristics of fracture systems. Fracture corridor extension signature, occasionally observed in LF-DAS field data when pumping stops, is verified in synthetic results for small pressure drop gradients, revealing that fractures

continue to propagate in this scenario. Quantitatively, fracture geometry characterization is improved by estimating width in multiple locations as time increases, with the support of deep learning (DL) algorithms I developed using data from multiple monitor wells.

The model framework captures a wide range of relevant phenomena and provides a solid foundation for generating accurate and rich synthetic data representing multiple distinct scenarios leading to interpretation optimization. Also, the development of specific packages (commercial or otherwise) that explicitly model DSS/LF-DAS, incorporating the impact of fracture opening and slippage, is still in its infancy. This project is novel in this regard, and it opens new avenues of research and applications of synthetic DSS/LF-DAS in hydraulic fracturing processes.

DEDICATION

This work is dedicated to:

Jesus Christ who gave his own life to save the humanity and from whom all my faith and force to never give up comes from.

My parents, Sr. José Gurjão Netto and Sra. Robéria Nascimento Ramos Gurjão, who educated me with all the best resources available, and taught me the fundamental importance of loving Jesus.

"For with God nothing shall be impossible."

Luke 1: 37 (KJ Bible)

ACKNOWLEDGEMENTS

I would like to thank families Gurjão and Ramos, especially my parents, Sr. José Gurjão Netto and Sra. Robéria Nascimento Ramos Gurjão, and my lovely siblings, Kevin Klain Ramos Gurjão and Kethlen Katerynne Ramos Gurjão, for the unconditional love and support.

My beloved wife, Isa Silveira de Araújo Gurjão, for the enthusiasm encouraging me to continue advancing spiritually and professionally.

My advisor, Dr. Eduardo Gildin, for the incentive, assistance, attention, patience and valuable opportunity at Texas A&M University.

Dr. William D. McCain, Jr. (In Memoriam), with whom I had the honor to work at the beginning of my doctoral studies performing petroleum fluids simulations with the objective to publish results in his planned reservoir engineering book, for all the life advice and learnings.

Dr. Richard Gibson, who introduced me the fiber-optics technology applied to hydraulic fracturing, for the tireless support with clever and bright advice that help me to improve my understanding on this doctoral project.

The dissertation committee members, Dr. Siddharth Misra, Dr. Kan Wu and Dr. Mark E. Everett, for their service and advice during this PhD program, including suggestions and revisions of this dissertation.

Dr. John Lee and Ms. Gia Alexander for all important guidance and support during the preparation for the 2022 SPE student paper contest.

Harold Vance Department of Petroleum Engineering and Texas A&M University for the use of physical installations and support to develop my projects.

My friend Charles Wallace and all friends from Impact Church (College Station-TX /USA) for the assistance, encouragement and fun time.

CONTRIBUTORS AND FUNDING SOURCES

Contributors

This work was supported by a committee formed by Dr. Eduardo Gildin (committee chair), Dr. Siddharth Misra and Dr. Kan Wu from the Petroleum Engineering department at Texas A&M University, and Dr. Mark E. Everett from the department of Geology and Geophysics at Texas A&M University.

Dr. Richard Gibson from Halliburton Energy Services contributed significantly for the development of this project, engaging in multiple discussions about fiber-optics technology with valuable suggestions.

Funding Sources

During my doctoral studies I received funding through research assistantships from the Energi Simulation, Crisman Institute for Petroleum Research and Dr. Gildin's L.F. Peterson '36 Professorship. Moreover, I received funding through teaching assistantships from the Petroleum Engineering and Statistics departments at Texas A&M University.

NOMENCLATURE

Latin

A	Boundary influence coefficient matrix for stress
a	Fracture half-length
$Adam$	Adaptive moment estimation optimizer
D_n	Normal displacement discontinuity
D_s	Shear displacement discontinuity
D_x	Displacement discontinuity along x-axis
D_y	Displacement discontinuity along y-axis
DAS	Distributed acoustic sensing
DSS	Distributed strain sensing
E	Young's modulus
E'	Plane strain modulus
$f(x, y)$	Solution of constant displacement discontinuity problem
G	Shear modulus
h_f	Fracture height
i	Injection rate in a single wing of symmetrical fracture
L_e	Element length
L_G	Fiber gauge length
LF-DAS	Low-frequency distributed acoustic sensing
MAE	Mean absolute error (L1 loss)
MSE	Mean squared error (L2 loss)
N	Total number of segments
n	Total number of observations
n	Fiber core refractive index
P_0	Linear coefficient of net pressure equation
P_1	Angular coefficient of net pressure equation

P_{net}	Net pressure
R	Geometric relation
r	Geometric relation
S_{Hmax}	Maximum horizonal stress
S_{hmin}	Minimum horizontal stress
t	Time
t_0	Initial simulation time
$tanh$	Hyperbolic tangent activation function
u_x	Displacement along x-axis
u_y	Displacement along y-axis
w	Fracture width
x	x-axis cartesian coordinate system
x_f	Fracture half-length
y	y-axis cartesian coordinate system
Y_i	True output
$\widehat{Y_i}$	Predicted output
Z	Unnormalized variable
Z_{max}	Maximum variable value
Z_{min}	Minimum variable value
$Z_{normalized}$	Normalized variable (ranges between 0 and 1)

Greek

β	Angle between global and local coordinate systems
ΔP_{net}	Change in net pressure
ΔS_H	Horizontal stress difference
Δt	Time step
$\Delta \sigma_s$	Change in shear stress
$\Delta \Phi$	Optical phase change

$\Delta\dot{\Phi}$	Optical phase change differentiated in time
ϵ or ϵ_y	Absolute strain along fiber axis
$\dot{\epsilon}$ or $\dot{\epsilon}_y$	Strain rate
Θ	Geometric relation
θ	Geometric relation
λ	Laser light wavelength
μ	Fluid viscosity
σ_n	Normal stress
σ_s	Shear stress
σ_{xx}	Stress along x-axis
σ_{xy}	Shear stress in cartesian coordinate system
σ_{yy}	Stress along y-axis
υ	Poisson's ratio
ψ	Pockels coefficient of fiber

Superscript

i	i-th element
j	j-th element
n	Current time step
$n+1$	Next time step

TABLE OF CONTENTS

Page

ABSTRACT ii

DEDICATION iv

ACKNOWLEDGEMENTS v

CONTRIBUTORS AND FUNDING SOURCES vi

NOMENCLATURE vii

TABLE OF CONTENTS x

LIST OF FIGURES xii

LIST OF TABLES xix

1. INTRODUCTION 1

1.1. Hydraulic Fracturing Technology and Surveillance Methods 1
1.2. Literature Review of Distributed Fiber-Optic Sensing 2
1.3. Research Objectives 7
1.3.1. Analytical Solution 7
1.3.2. Numerical Solution 7
1.3.3. Deep Learning Algorithm and Fracture Width Estimation 8
1.4. Research Scope and Contributions 8
1.5. Organization 9

2. METHODS 10

2.1. Analytical Solution 10
2.2. Numerical Solution 13
2.2.1. Numerical Solution Validation 18
2.3. Machine Learning and Deep Learning 20
2.3.1. Deep Learning Algorithm and Fracture Width Estimation 22
2.4. Fracture Width Estimation in the Field Using “Discontinuity Length” Method 27

3. RESULTS AND DISCUSSIONS 29

3.1. Analytical Solution 29

3.2. Numerical Solution 38
3.2.1. Fiber Gauge Length Impact on Strain 44
3.2.2. Natural Fracture Impact on Cluster Efficiency 45
3.2.3. Characterization of Strain Fields When Pumping Stops 47
3.2.4. Identification of Fracture Hit Moment 49
3.2.5. Stress Shadow Transmissibility 51
3.3. Deep Learning Algorithm and Fracture Width Estimation 54
3.3.1. Case 1: Single Hydraulic Fracture 54
3.3.2. Case 2: Multiple Hydraulic Fractures 60
3.4. Fracture Width Estimation Using Strain Dataset from the Stress Shadow Zone 64

4. CONCLUSIONS 69

4.1. Recommendations for Future Work 70

REFERENCES 72

APPENDIX A. DISPLACEMENT DISCONTINUITY METHOD SUPPLEMENTARY EQUATIONS 86

APPENDIX B. MODELING OF STRAIN FIELDS INCORPORATING HYDRAULIC AND NATURAL FRACTURE INTERACTIONS 88

APPENDIX C. MONITOR WELL SENSITIVITY TO STRAIN SIGNAL ARRIVALS 94

LIST OF FIGURES

Page

Figure 1.1–Hypothetic deployment scenario of geophysical survey equipment (point and distributed sensors): on the top, smooth curve representing point sensors theoretical output data; on the bottom, conceptual curve rich in details (missed by geophones). Adapted from Silixa (2019). 3

Figure 1.2–Signal arriving at oblique angle (θ) to the fiber-optic cable. Fiber has the greatest sensitivity to parallel arrivals ($\theta = 0°$). 3

Figure 1.3–Schematic showing typical distributed sensing system equipment (interrogator unit and glass fiber) and sources (thermal and acoustic) about which the backscattered light carries information. 4

Figure 1.4–Spectrum of fiber-optics backscattered light (stokes and anti-stokes) detailing Rayleigh (DAS), Brillouin (DSS) and Raman (DTS) recorded signals based on frequency. Adapted from Silixa (2019). 4

Figure 1.5–Schematic showing fiber-optic cable, measurement point associated with particular gauge length, and channel spacing defined as the distance between two consecutive measurements. 4

Figure 1.6–(a) Cross-well (operation and monitor wells distancing 100 ft are depicted as 1 and 2, respectively), and (b) in-well (single well represented by 1, works simultaneously as operation and monitor well) fiber configurations. 6

Figure 2.1–Flowchart of DSS and LF-DAS calculation using the analytical solution. ...11

Figure 2.2–Geometric representation of a crack with parameters to estimate induced stresses. 12

Figure 2.3–Representation of a crack (left) discretized by N displacement discontinuities (right). 14

Figure 2.4–Flowchart of DSS and LF-DAS calculation using the numerical solution. ...16

Figure 2.5–Represented by dashed lines, possible propagation pathways that hydraulic fractures (red) follow after intersecting natural fractures (dark aqua): (a) along its original direction, (b) along natural fracture creating a new path at the end, and (c) along natural fracture kinking out in a weak point. 17

Figure 2.6–Map view ($xy - plane$) of strain at the end of numerical simulation (100 time steps) of a fracture with 500 ft half-length. 18

Figure 2.7–Fracture width estimated by analytical and numerical methods are represented by full red curve and dashed red curve, respectively. The relative error at the end of a simulation comprised by 100 time steps is shown by the full black curve. 20

Figure 2.8–Schematic architecture of a deep learning model. It is represented by a combination of input, hidden and output layers containing neurons. Adapted from Bahi and Batouche (2018). 21

Figure 2.9–Linear combination of neurons from input layer and respective weights working as input of activation function. The function incorporates nonlinearities in the process and outputs one neuron of subsequent layer. 22

Figure 2.10–Generic meshgrid dataset for the specific case where monitor and operation wells are separated by distance X, with details for components of each grid point (i.e., space, time, and displacement y). 23

Figure 2.11– Selected architecture of ANN algorithm used in this project: (1) The input layer is composed of three features (X, Y, and time); (2) There are seven hidden layers with the number of neurons varying from 10 to 100; and (3) The output layer consists of the uy variable. 23

Figure 2.12– Dataset of specific scenario composed by 3 hydraulic fractures. On the left, axial displacement component (uy) of 7 monitor wells deployed in different locations (i.e., X = 0, 100, 200, 300, 400, 500 and 600 ft). On the right, corresponding LF-DAS data of each X position obtained deriving uy sequentially in space and time. 25

Figure 2.13–Dataset of specific fracture scenario characterized by: (1) single hydraulic fracture located at y = 100 ft; (2) monitor well placed at X = 300 ft (i.e., the distance between operation and monitor wells); and (3) fracture hit at t = 54.7 min. In this graph, predicted axial displacement of four time steps before fracture hit are plotted against channel location (continuous data). As time advances, fracture approaches the fiber and rock deformation at monitor well location increases. 26

Figure 2.14–Dataset of specific fracture scenario characterized by: (1) single hydraulic fracture located at y = 100 ft; (2) monitor well placed at X = 300 ft (i.e., the distance between operation and monitor wells); and (3) fracture hit at t = 54.7 min. In this graph, predicted axial displacement of four time steps after fracture hit are plotted against channel location (discontinuous data). As time increases, rock pulls apart even more at monitor well location. 26

Figure 2.15–Dataset of specific fracture scenario characterized by: (1) single hydraulic fracture located at y = 100 ft; (2) monitor well placed at X = 300 ft (i.e., the distance between operation and monitor wells); and (3) fracture hit at t = 54.7 min. In this graph, predicted axial displacement at t = 58 min (after fracture hit) is plotted against channel location (discontinuous data). The magnitude of "Discontinuity length" is 0.122 in, and it is approximately the fracture width. 27

Figure 3.1–Low-frequency DAS field data highlighting classic features associated with propagation of hydraulic fractures: (1) heart-shaped pattern, (2) fracture hits, and (3) stress shadow surrounding the opening fracture. Adapted from Richter et al. (2019). 31

Figure 3.2–(a) DSS and (b) LF-DAS synthetic data of base case scenario applying the analytical solution. (c) Net pressure calculated using the 2D KGD fracture model for this specific case. Typical features present in field data are observed: heart-shaped pattern of a fracture approaching the fiber, stress shadow, and fracture-hit (t = 86.9s) followed by its propagation. 31

Figure 3.3–DSS and LF-DAS results of Sensitivity Analysis 1. Fracture hits monitor well faster in scenario *b* where Young's modulus is higher. 33

Figure 3.4–Average fracture width over time of scenarios *a* and *b* (Sensitivity Analysis 1: varying Young's modulus). 33

Figure 3.5–DSS and LF-DAS results of Sensitivity Analysis 2. Fracture hits monitor well faster in scenario *a* where the fluid viscosity is lower. 34

Figure 3.6–Average fracture width over time of scenarios *a* and *b* (Sensitivity Analysis 2: varying fluid viscosity). 35

Figure 3.7–DSS and LF-DAS results of Sensitivity Analysis 3. Fracture hits monitor well faster in scenario *b* where injection rate is higher. 36

Figure 3.8–Average fracture width over time of scenarios *a* and *b* (Sensitivity Analysis 3: varying injection rate). 37

Figure 3.9–(a) DSS and (b) LF-DAS modeling results of base case scenario consisting of 5 perforation clusters. Typical characteristics present in field data can be observed more clearly in the LF-DAS waterfall plot: fracture approaching the fiber pictured as heart-shaped pattern, fracture hits, and stress shadow. 39

Figure 3.10–Four LF-DAS field examples showing traditional features modeled by the numerical framework developed in this project: the heart-shaped pattern of a fracture approaching the fiber, stress shadow and fracture hit. 40

Figure 3.11–Strain rate sum of base case scenario. Individual spikes and distance between consecutives spikes represent the cluster location and spacing, respectively. 40

Figure 3.12–Map view of lateral section of horizontal wells varying NF orientation and length. 42

Figure 3.13–DSS and LF-DAS modeling results of sensitivity analysis varying NF orientation and length. 43

Figure 3.14–(a, b, c) LF-DAS waterfall plots using 1 m, 5 m, and 10 m gauge lengths, respectively. 44

Figure 3.15–Map view of lateral section of horizontal wells varying NF length (a and c) and respective LF-DAS modeling results (b and d). 46

Figure 3.16–Net pressure profile at operation well location assumed in studies 1 and 2. Pressure: (1) increases linearly for 60 min when the pump is on; (2) Drops 20 psi immediately at the pump off instant; and (3) Lastly drops following a linear trend for 30 min. Six different pressure drop gradients are analyzed when pumping stops. 48

Figure 3.17–LF-DAS results of study 1 (fracture propagation terminates when pumping is finished) for all six pressure drop gradients. 48

Figure 3.18–LF-DAS results of study 2 (fracture propagation doesn't terminate when pumping is finished) for all six pressure drop gradients. 49

Figure 3.19–LF-DAS results of four cluster spacing scenarios (i.e., 25, 50, 100, and 150 ft) in this study, consisting of three hydraulic fractures. 50

Figure 3.20–Plot of the second derivative of stress acquired by channel located at y = -75 ft. 51

Figure 3.21–(a) DSS and (b) LF-DAS modeling results of a single hydraulic fracture. Following fracture hit at time = 30.7 min, DSS waterfall plot indicates that the extension sign surrounding opening fracture delays before switching to compression. This phenomenon is not observed in the LF-DAS plot, which presents an immediate polarity change above and below the fracture face. 52

Figure 3.22– Stress of 10 time steps after fracture hit versus distance from fracture face (stress shadow transmissibility). 53

Figure 3.23–Fractures observed in the Eagle Ford pilot. (a) Dipping fractures in the core; (b) Computed Tomography (CT) scan image of the same section of core

shown in a; (c) 18 ft of an image log taken from the same well showing several closely spaced fractures. Adapted from Raterman et al. (2018). 53

Figure 3.24–Fractures observed in Midland Basin pilot. Top: 3-ft long core-back sample containing eight parallel/subparallel fractures. Bottom: CT scan image of corresponding core sample. Adapted from Fu et al. (2021). 54

Figure 3.25–(a) Map view of scenario composed by single hydraulic fracture located at y = 100 ft where operation and monitor wells are distancing 300 ft, and (b) corresponding true axial displacement obtained with DDM code.....55

Figure 3.26–Histogram of axial displacement (machine learning algorithm supervisor variable) of scenario composed by single hydraulic fracture. The total number of observations is 13,660,920 (normal distribution), with magnitudes ranging between -0.4 and +0.4 in, and greatest concentration around 0. 55

Figure 3.27–Plot of L2 loss against n° of epochs obtained during training stage of dataset representing scenario composed by single hydraulic fracture. There is pretty much no overfitting and greatest reduction in error function occurs at the phase onset. 56

Figure 3.28–(a) Predicted uy at monitor well location (X = 300 ft) using developed spatio-temporal machine learning scheme. (b) Relative error between predicted and true uy at X = 300 ft. DL model has an overall consistent performance: (1) error is negligible in the entire waterfall plot region (except at early time steps); and (2) instant of fracture hit is correctly captured (t = 54.7 min). 57

Figure 3.29–LF-DAS data calculated at X = 300 ft based on estimated uy with developed spatio-temporal machine learning model (case 1). Classic features are observed: (1) hart-shaped pattern; (2) fracture hit; and (3) stress shadow. 58

Figure 3.30–Results obtained following fracture hit (t = 54.7 min) at monitor well location (X = 300 ft). Red curve shows upward trend of predicted fracture width (estimated using proposed "discontinuity length" method), while green curve displays the relative error between predicted and true widths falling near 0% after an initial 15% at fracture hit instant. 59

Figure 3.31–Plot of predicted fracture width (estimated using proposed "discontinuity length" method and data obtained from developed DL model) against position (X ranges from 300 to near 700 ft) for 8 consecutive time steps (t varies from 85 to 126.7 min). For all time steps, curves have an elliptic shape resembling fracture contour. 60

Figure 3.32–Plot of relative error between predicted width (estimated using proposed "discontinuity length" method and data obtained from developed DL model) and the true one (generated with DDM code) versus location (X ranges from 300 to near 700 ft) for 8 consecutive time steps (t varies from 85 to 126.7 min). Magnitude of error drops near 0% in each X location as time goes up (i.e., right after fracture hit). 60

Figure 3.33–(a) Map view of scenario composed by 3 hydraulic fractures located at y = -200, 0, +200 ft where operation and monitor wells are distancing 300 ft, and (b) corresponding true axial displacement obtained with DDM code. 61

Figure 3.34–Histogram of axial displacement (machine learning algorithm supervisor variable) of scenario composed by 3 hydraulic fractures. The total number of observations is 6,505,200 (normal distribution), with magnitudes ranging between -0.4 and +0.4 in, and greatest concentration around 0. 61

Figure 3.35–Plot of L1 loss against n° of epochs obtained during training stage of dataset representing scenario composed by 3 hydraulic fractures. There is pretty much no overfitting and error function drops consistently as n° of epochs increases.....62

Figure 3.36–(a) Predicted uy at monitor well location (X = 300 ft) using developed spatio-temporal machine learning scheme. (b) Relative error between predicted and true uy at X = 300 ft. DL model has an overall consistent performance: (1) error is negligible in the entire waterfall plot region (except at extremely early time steps); and (2) instant of fracture hit is correctly captured (HFs 1 and 3 at t = 23.2 min, and HF 2 at t = 26.4 min).....63

Figure 3.37–LF-DAS data calculated at X = 300 ft based on estimated uy with developed spatio-temporal machine learning model (case 2). Classic features are observed: (1) hart-shaped pattern; (2) fracture hit; and (3) stress shadow. 64

Figure 3.38–LF-DAS waterfall plot detailing the fracture corridor and stress shadow region. Adapted from Jin and Roy (2017). 65

Figure 3.39–Histogram of fracture width (output variable) of machine learning model. The total number of observations is 2400 (log-normal distribution), with magnitudes ranging between 3.3 x 10^{-5} and 0.34 in.....66

Figure 3.40–Pairplots comparing true and predicted width values applying multilinear regression, SVR, ANN and random forest algorithms with the testing dataset. The R2 metric indicates random forest as champion model.....67

Figure A.1–Global (xy) and local (xy) coordinate systems separated by the angle β. ...86

Figure B.1–Map view of lateral section of horizontal wells varying the number of NF. 88

Figure B.2–DSS and LF-DAS modeling results of sensitivity analysis varying the number of NF. 89

Figure B.3–Strain rate sum for scenario *c* of sensitivity analysis varying the number of NF. Spikes aid determining cluster location. 90

Figure B.4–Map view of lateral section of horizontal wells varying NF length. 91

Figure B.5–DSS and LF-DAS modeling results of sensitivity analysis varying NF length. 93

Figure C.1–Map view of lateral section of horizontal wells showing a particular configuration with 100 ft well distance. 94

Figure C.2–DSS and LF-DAS results varying distance between monitor and operation wells. 96

LIST OF TABLES

Page

Table 2.1–Parameters used in the validation of numerical solution. 19

Table 3.1–Parameters used in base case scenario. 30

Table 3.2–Parameters used in sensitivity analysis 1. 32

Table 3.3–Parameters used in sensitivity analysis 2. 33

Table 3.4–Parameters used in sensitivity analysis 3. 35

Table 3.5–Qualitative review of fracture propagation speed when the specified 37

Table 3.6–Parameters used in numerical simulation. 38

Table 3.7– Hydraulic fracture propagation speed. 38

Table 3.8–Performance results of multilinear regression, SVR, ANN and random forest algorithms with testing dataset. 68

Table C.1–Natural fractures details. 94

1. INTRODUCTION

1.1. Hydraulic Fracturing Technology and Surveillance Methods

The combination of hydraulic fracturing and horizontal drilling technologies were the pillars for the hydrocarbon production boost in unconventional reservoirs in the US (i.e., shale revolution) (Wiley et al., 2004; Roudakov and Rohwer, 2006; Weijers et al., 2019). Multistage hydraulic fracturing (Salah et al., 2017), plug and perf completion technique (Jamaloei, 2021), and zipper fracturing (Schofield et al., 2015) speeded up the shale stimulation process. Completion designs were improved varying well, stage and cluster spacings (Huckabee et al., 2021). Nanoparticles improved the performance of fracturing fluids in high-pressure and high-temperature (HPHT) downhole conditions (Al-Muntasheri et al., 2017). Advanced materials contributed for the development of high strength (required in deep wells) and ultra-lightweight (desirable to reduce proppant settling and increase the propped fracture length) proppants (Liang et al., 2015). These technologies significantly enhanced oil/gas production in tiny permeability reservoirs.

Monitoring of fracture propagation during the treatment is a fundamental task that has the potential to improve completion design and optimize production. Surveillance technologies used in fracturing operations include: downhole cameras to inspect perforation erosion, microseismic, distributed fiber-optic sensing, downhole pressure/temperature gauges, sealed wellbore pressure monitoring (SWPM), tracers, electromagnetic fluid monitoring, and borehole pressure-wave reflections (acoustics) (Gutierrez et al., 2010; Hickey et al., 2017; Dalamarinis et al., 2020; Haustveit et al., 2020; Filev et al., 2021; Cipolla et al., 2022a; Cipolla et al., 2022b ; McKimmy et al., 2022; Zang, 2022).

Microseismic based on geophone recording was for a long time the primary diagnostic for estimating stage-level fracture geometry. The need for technologies with high spatio-temporal resolution able to provide measurement details on cluster-level, influenced the application of distributed fiber-optic sensing in the stimulation process of unconventional reservoirs. The popularity of this method is expanding rapidly, and the

deployment costs are reducing especially when disposable fiber is selected (Mantell et al., 2022). Due to the relevance of this topic, the focus of this study is on distributed fiber-optic sensing surveillance technology.

1.2. Literature Review of Distributed Fiber-Optic Sensing

Fiber-optic-based sensing is a versatile technology that is being adopted for monitoring by the oil and gas industry in many upstream areas such as: well stimulation (matrix acidizing and hydraulic fracturing), hydrocarbon recovery, production operations (flow monitoring and artificial lift), well integrity and geophysical surveys (seismic methods) (Koelman et al., 2011; Holley and Kalia, 2015; Hull et al., 2017; Jin et al., 2021). According to Molenaar et al. (2012) this surveillance technique was first introduced in wells in the 1990s with single point pressure and temperature sensors followed by distributed temperature sensing.

According to Silixa (2019), the distinct advantages of distributed fiber-optics sensing compared to point sensors (i.e., geophones) include: (1) substantial spatial coverage capturing details maybe missed by geophones (**Figure 1.1**); (2) high resolution (e.g., sampling rate typically ranges from 5 to 10 kHz) collecting highly transient spatio-temporal processes; (3) flexible deployment options including hazardous/harsh environments (e.g., measurements can be done in injector wells). This surveillance method is a single component sensor that primarily measures parallel microseismic signal arrivals to the fiber with sensitivity to influxes at oblique angles θ (**Figure 1.2**) decreasing roughly by $cos^2\theta$ factor (Hartog, 2017; Hull et al., 2017; Sherman et al., 2019). According to Mateeva et al. (2014) it is possible to enhance fiber sensitivity by winding it into a helical structure, which would allow the cable to simultaneously sample signals over a great range of orientations.

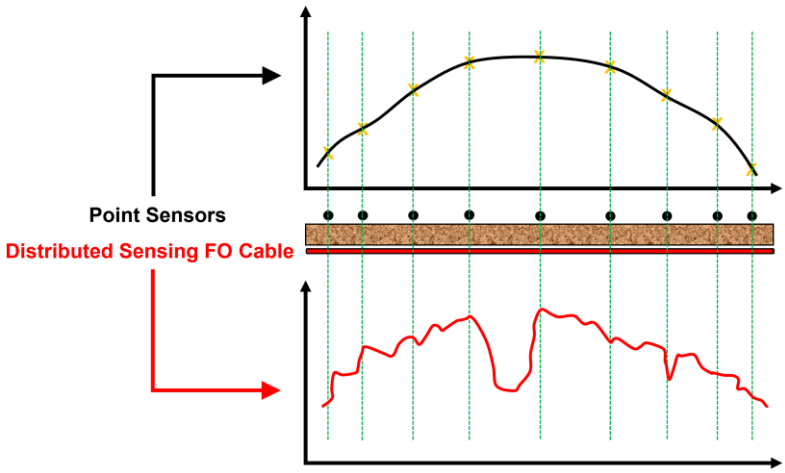

Figure 1.1–Hypothetic deployment scenario of geophysical survey equipment (point and distributed sensors): on the top, smooth curve representing point sensors theoretical output data; on the bottom, conceptual curve rich in details (missed by geophones). Adapted from Silixa (2019).

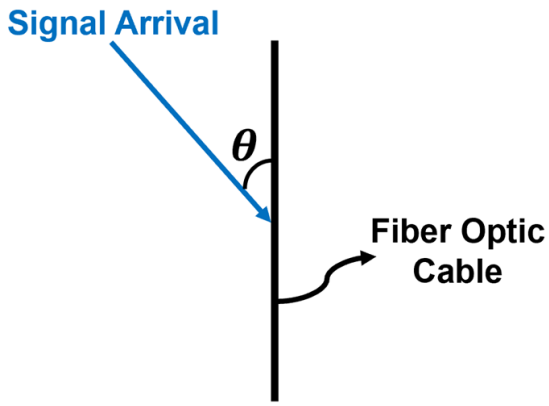

Figure 1.2–Signal arriving at oblique angle (θ) to the fiber-optic cable. Fiber has the greatest sensitivity to parallel arrivals ($\theta = 0°$).

Fiber-optic cable can be permanently cemented behind the casing or deployed in wellbores via retrievable wireline (Richter et al., 2019). The general principle associated with distributed sensing is briefly described as follows: (1) an interrogator unit generates a light pulse that propagates along the fiber and interacts with glass microscopic defects; (2) local conditions (thermal and acoustic) slightly affect the glass fiber changing its light transmission characteristics (**Figure 1.3**); (3) modified light signal (Brillouin, Raman and Rayleigh) is backscattered and recorded at the interrogator unit (**Figure 1.4**) (Dickenson et al., 2016). As shown in **Figure 1.5**, each measurement represents an average over a specific fiber interval, referred to as gauge length (GL), and the distance between two

consecutive measurements is called channel spacing (Karrenbach et al., 2017; Ugueto et al., 2019).

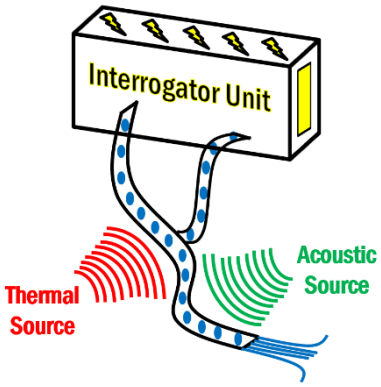

Figure 1.3–Schematic showing typical distributed sensing system equipment (interrogator unit and glass fiber) and sources (thermal and acoustic) about which the backscattered light carries information.

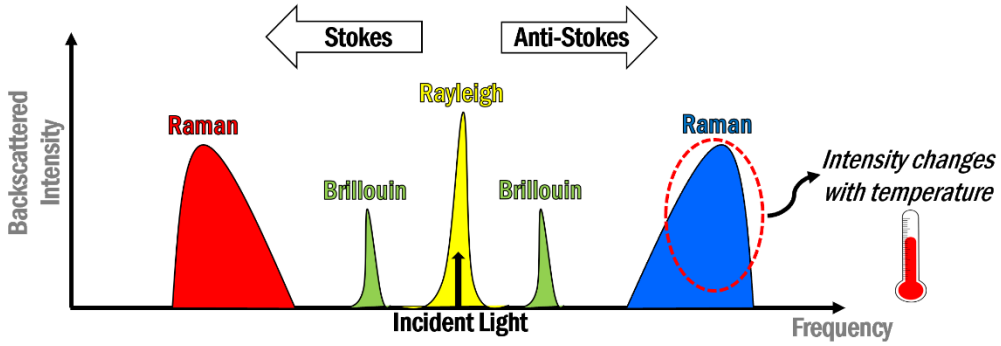

Figure 1.4–Spectrum of fiber-optics backscattered light (stokes and anti-stokes) detailing Rayleigh (DAS), Brillouin (DSS) and Raman (DTS) recorded signals based on frequency. Adapted from Silixa (2019).

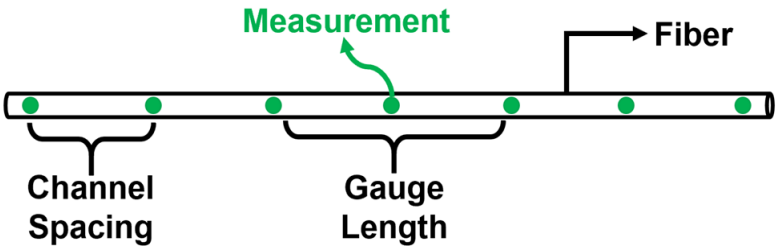

Figure 1.5–Schematic showing fiber-optic cable, measurement point associated with particular gauge length, and channel spacing defined as the distance between two consecutive measurements.

Rayleigh, Brillouin and Raman scatterings are traditionally associated with Distributed Acoustic Sensing (DAS), Distributed Strain Sensing (DSS) and Distributed

Temperature Sensing (DTS) techniques, respectively. During hydraulic fracturing treatments when wells are equipped with fiber-optic cable, DSS and DAS responses carry primarily acoustic information (in some instances thermal correction is required). Raw DAS data is registered in the form of optical phase change measured in radians, which at low-frequency band is directly related to strain perturbation (Lindsey et al., 2020) and it can be regarded as equivalent to strain rate according to Daley et al. (2016). On the other hand, Brillouin-based DSS data represents absolute strain, and it is obtained at frequency and levels of sensitivity lower than DAS (Kechavarzi et al., 2019).

According to Febus Optics (2019), one main advantage of DTS compared with DSS/DAS is the fact that it is only sensitive to temperature and consequently there is no need for strain correction. However, Raman scattered light is weak and hard to detect, so the frequency of acquisition of DTS signals is much smaller than DAS signals for instance (Johannessen et al., 2012). Pakhotina et al. (2020) mention the importance of acquiring temperature and strain fiber-optics data to support the interpretation process.

Jin and Roy (2017), Ichikawa et al. (2020), Li et al. (2020) and White et al. (2020) mention and show with field examples that different frequency bands of DAS signal can be used for various purposes in hydraulic fracturing operations: (1) low-frequency band (< 0.05 Hz) of cross-well fiber (**Figure 1.6a**) can be applied to assist fracture geometry characterization and identify fracture hits; (2) high-frequency band (> 1 Hz) of in-well fiber (**Figure 1.6b**) can be used to estimate perforation cluster fluid/proppant distribution and detect potential fracture communication.

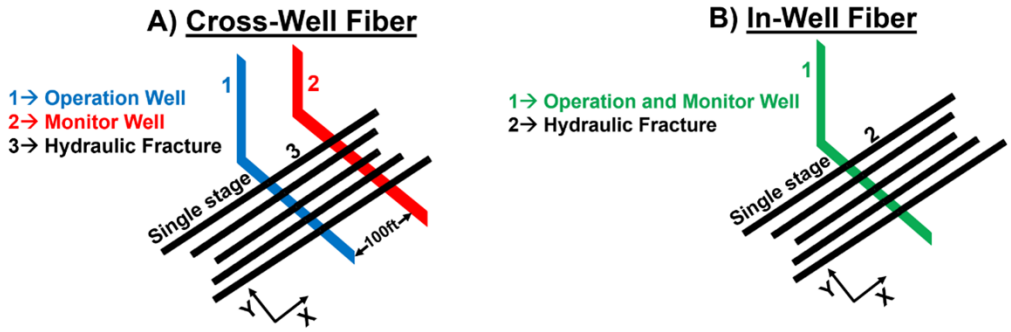

Figure 1.6–(a) Cross-well (operation and monitor wells distancing 100 ft are depicted as 1 and 2, respectively), and (b) in-well (single well represented by 1, works simultaneously as operation and monitor well) fiber configurations.

DSS (absolute strain) and low-frequency DAS (strain rate) are massive datasets with vast applicability in hydraulic fracturing operations. However, given the complexity associated with field data, its potential is not fully explored yet. Special techniques are required to assist engineers and geoscientists in the interpretation process of strain type data to improve completion design and, consequently, to optimize production of unconventional reservoirs. Numerical simulation is a potential tool that may add value in the qualitative and quantitative interpretation tasks of strain type of data acquired by distributed fiber-optics.

Qualitatively, recent studies have modeled fiber-optic strain response considering the following points:

1. Single and multiple hydraulic fractures (HF) failing in tensile mode using the Displacement Discontinuity Method (DDM) (Liu et al., 2020; Zhang et al., 2020; Shahri et al., 2021).
2. Single hydraulic fracture opening and associated with Discrete Fracture Network (DFN) integrating the Finite Element Method (FEM) and Finite Volume Method (FVM) (Sherman et al., 2019).
3. Single and multiple hydraulic fractures failing in tensile mode, and single hydraulic fracture associated with DFN using FEM (Tan et al., 2021).

Quantitatively, Liu et al. (2021a, 2021b) has developed the Green's function-based inversion model attempting to estimate fracture width in a single location (i.e., monitor well).

1.3. Research Objectives

In this work, I develop a simulation framework that relies on analytical and numerical solutions to model strain fields generated by hydraulic fracturing (i.e., DSS and low-frequency DAS responses). The main goal is to assist specialists in the interpretation process of strain field data.

The synthetic data generated by the numerical simulator is used to train and test machine learning algorithms able to improve the fracture geometry characterization.

1.3.1. Analytical Solution

Evaluate the behavior of strain time histories in terms of fracture propagation speed (i.e., fracture hit), performing a sensitivity study on rock (i.e., Young's modulus) and fluid (i.e., viscosity and flow rate) parameters.

1.3.2. Numerical Solution

1. Determine the influence of natural fracture geometry (e.g., orientation angle and length) on strain.
2. Quantify fiber gauge length impact on strain time histories.
3. Determine natural fracture impact on cluster efficiency using strain datasets.
4. Characterize strain fields when pumping stops to verify the potential continuation of fracture extension.
5. Identify fracture hit moment based on derivative of stress.
6. Analyze stress shadow transmissibility with distance from fracture face.

1.3.3. Deep Learning Algorithm and Fracture Width Estimation

1. Develop deep learning (DL) models to estimate the magnitude of strain fields for any spatio-temporal input, using synthetic data from multiple monitor wells generated by the numerical technique (fiber sensitivity is restricted to a region near the monitor well).
2. Predict fracture width in multiple locations over time with the support of developed DL algorithm.

1.4. Research Scope and Contributions

For the first time, the strain problem is solved analytically by coupling a 2D fracture model (e.g., Khristianovic-Geertsma-de Klerk [KGD]) and the induced stress solution established by Sneddon (1946). The analytical technique can model a single hydraulic fracture failing in tensile mode. In turn, I implement the numerical technique using the Displacement Discontinuity Method (DDM), which is able to model multiple fractures failing in tensile mode and more complex scenarios not contemplated by previous studies considering shear failure of natural fractures.

This work is one of the first to include hydraulic and natural fracture interactions when modeling fiber-optics strain response using the numerical solution. This leads the project to study the impact of natural fractures on DSS/LF-DAS data, which is often interpreted purely in terms of opening fractures.

The model framework based on the numerical solution (i.e., DDM) captures a range of significant phenomena present in the field data and can be a foundation for the generation of rich strain synthetic data encompassing multiple scenarios: (1) planar hydraulic fractures; (2) hydraulic and natural fracture interactions; and (3) natural fractures with variable distribution and/or geometry. I suspect that this great volume of synthetic data combined with processed (filtered to remove noise and compressed to reduce memory size requirements) field data (Brankovic et al. 2021) can be used to train a deep learning image recognition model such as convolutional neural networks also

known as CNN or ConvNet (Bishop 2006; Krizhevsky et al. 2017; Géron 2019), to be applied in the test stage classifying the governing physical scenario associated with field data. This physics-based machine learning framework (Yao and Yang, 2016) can represent a positive breakthrough assisting engineers and geoscientists interpreting complex strain type of data coming from unconventional reservoirs.

1.5. Organization

This work is organized in four chapters. Chapter 1 corresponds to literature review of hydraulic fracturing technology and distributed fiber-optic sensing, along with research contributions and objectives. Chapter 2 describes the methodology adopted to model analytically and numerically strain fields generated during hydraulic fracturing treatments, and the approach based on deep learning algorithms developed using data from multiple monitor wells to improve the fracture geometry characterization. Chapter 3 summarizes the main results and discussions. Chapter 4 ends with conclusions and suggestions for future work.

2. METHODS

In this work, I model absolute strain (DSS) and strain rate (low-frequency DAS) responses of parallel signal arrivals to fiber, examining a cross-well fiber deployment and considering a perfect mechanical coupling of fiber to surrounding media. Analytical and numerical solutions are used to generate fiber-optics strain synthetic data.

Synthetic data from the numerical technique is used to train and test deep learning (DL) models to predict strain fields in any position/time. Integration of DL algorithms and proposed "discontinuity length" method able to estimate fracture width in a single point, improves the fracture geometry characterization estimating such property in multiple locations as a function of time.

2.1. Analytical Solution

I apply the analytical technique to simulate a single hydraulic fracture opening. The solution is obtained coupling 2D fracture and induced stress models, represented in this study by Khristianovic-Geertsma-de Klerk (KGD) (Valkó and Economides, 1995) and Sneddon (1946), respectively. Assumptions include: (1) plane strain holding in horizontal plane (i.e., problem dimensionality reduction); (2) no fluid leak-off; (3) Newtonian fluid; (4) linear elastic deformation, which implies reversible changes; (5) homogeneous (i.e., uniform composition) and isotropic material (i.e., properties are independent of direction and two elastic constants are sufficient to describe the material behavior); (6) uniform stress on fracture face.

Figure 2.1 shows a flowchart detailing the process to estimate DSS and LF-DAS based on the analytical solution. Inputs of the KGD fracture model are: (1) initial simulation time (t_0); (2) fracture height (h_f) not exceeding reservoir height (i.e., controlled stimulation process); rock mechanical properties consisting of (3) Young's modulus (E) on the order of 10^6 psi and (4) Poisson's ratio (υ) that is dimensionless and ranges between 0 and 0.5; fluid mechanical properties such as (5) viscosity (μ) and (6) injection rate used in a single wing of symmetrical hydraulic fracture (i).

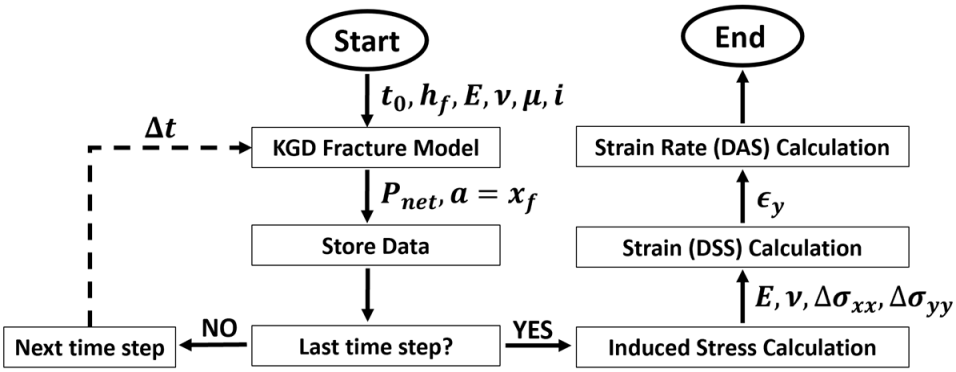

Figure 2.1–Flowchart of DSS and LF-DAS calculation using the analytical solution.

Net pressure (P_{net}) on the order of 10^2 psi in the field, which is assumed uniform on the fracture face, and fracture half-length ($a = x_f$) are the estimates of the KGD model that I select to store[1]:

$$P_{net} = 1.09(E'^2\mu)^{\frac{1}{3}}t^{-\frac{1}{3}}, \tag{1}$$

$$x_f = 0.539\left(\frac{i^3E'}{\mu h_f^3}\right)^{\frac{1}{6}}t^{\frac{2}{3}}, \tag{2}$$

where E' is the plane strain modulus defined as:

$$E' = \frac{E}{1-\upsilon^2}. \tag{3}$$

The average fracture width of the KGD model (in the field it generally assumes tiny magnitudes on the order of inches) can be estimated with the following equation in SI units:

$$\overline{w} = 2.53\left(\frac{\mu i x_f^2}{h_f E'}\right)^{\frac{1}{4}}. \tag{4}$$

At the end of each time step, I add a time (Δt) increment in the simulation and fracture continues propagating. Once 2D fracture model reaches last time step, stored

[1] Eqs. 1 and 2 in SI Units.

synthetic data is used to calculate induced stresses ($\Delta\sigma_{xx}$ and $\Delta\sigma_{yy}$) along fiber for the simulation time span applying Sneddon solution:

$$\Delta\sigma_{xx} = P_{net}[rR^{-1}\,cos(\theta - \Theta) - 1 - a^2 rR^{-3}\,sin\,\theta\,sin\,3\Theta]\,, \tag{5}$$

$$\Delta\sigma_{yy} = P_{net}[rR^{-1}\,cos(\theta - \Theta) - 1 + a^2 rR^{-3}\,sin\,\theta\,sin\,3\Theta]\,, \tag{6}$$

where $r,\ R,\ \theta$ and Θ (**Figure 2.2**) are defined as follows:

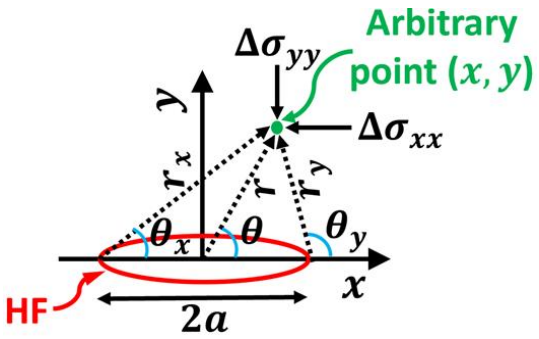

Figure 2.2–Geometric representation of a crack with parameters to estimate induced stresses.

$$r = \sqrt{x^2 + y^2}\,, \tag{7}$$

$$R = \sqrt{r_x r_y}\,, \tag{8}$$

$$\theta = tan^{-1}\frac{y}{x}, \tag{9}$$

$$\Theta = \frac{\theta_x + \theta_y}{2}, \tag{10}$$

and parameters r_x, r_y, θ_x and θ_y can be obtained by:

$$r_x = \sqrt{y^2 + (x + a)^2}\,, \tag{11}$$

$$r_y = \sqrt{y^2 + (x - a)^2}\,, \tag{12}$$

$$\theta_x = tan^{-1}\frac{y}{x + a}, \tag{13}$$

$$\theta_y = tan^{-1}\frac{y}{x-a}. \tag{14}$$

These calculations result in incorrect estimates of induced stresses if any angle θ, θ_x and θ_y assume a negative value. Therefore, in such a case, π should be added to the parameter.

In the following step, using rock mechanical properties (E and υ) and calculated induced stresses ($\Delta\sigma_{xx}$ and $\Delta\sigma_{yy}$), I assume a plane strain model (Economides and Nolte, 1989) to estimate absolute strain (DSS) along the horizontal lateral placed in the y-direction (ϵ_y):

$$\epsilon_y = \frac{1+\upsilon}{E}\left[(1-\upsilon)\Delta\sigma_{yy} - \upsilon\Delta\sigma_{xx}\right]. \tag{15}$$

Once DSS is obtained, LF-DAS along the fiber is estimated by differentiation of absolute strain in time applying the forward difference approximation:

$$\dot{\epsilon}_y = \frac{\epsilon_y(t^{n+1}) - \epsilon_y(t^n)}{t^{n+1} - t^n}. \tag{16}$$

2.2. Numerical Solution

The second method I use to model strain fields is a numerical solution based on the Displacement Discontinuity Method (DDM) (Crouch, 1976; Crouch and Starfield, 1983; Wu, 2014; Gurjao et al., 2021). In this case, complex scenarios composed of multiple fractures failing in tensile or shear mode can be included in simulations.

The DDM is modeled by distributing a series of constant displacement discontinuities (normal: D_n; shear: D_s) generated by opening/slippage of associated fractures, and of unknown magnitude over a finite segment ($xy-plane$) in an infinite elastic body (**Figure 2.3**). In this study, normal (σ_n) and shear (σ_s) stresses are assigned as boundary conditions for elements representing hydraulic fractures (tensile failure) and natural fractures (shear failure), respectively.

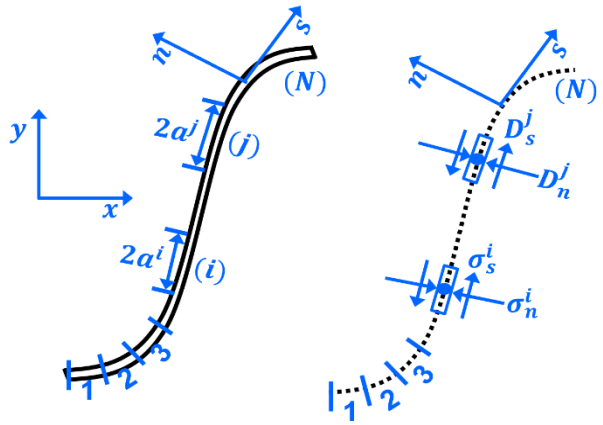

Figure 2.3–Representation of a crack (left) discretized by *N* displacement discontinuities (right).

Based on normal (i.e., net pressure) and shear stresses imposed on the i^{th} boundary element, shear and normal displacement discontinuities at any element j can be computed solving the following system of equations for $i = 1\ to\ N$ (total number of segments) using for instance the Gaussian elimination method (i.e., system of $2N$ simultaneous linear equations in $2N$ unknowns):

$$\sigma_s^i = \sum_{j=1}^{N} A_{ss}^{ij} D_s^j + \sum_{j=1}^{N} A_{sn}^{ij} D_n^j \,, \tag{17}$$

$$\sigma_n^i = \sum_{j=1}^{N} A_{ns}^{ij} D_s^j + \sum_{j=1}^{N} A_{nn}^{ij} D_n^j \,, \tag{18}$$

where $\boldsymbol{A_{ss}^{ij}}$, $\boldsymbol{A_{sn}^{ij}}$, $\boldsymbol{A_{ns}^{ij}}$ and $\boldsymbol{A_{nn}^{ij}}$ are boundary influence coefficient matrices for the stresses defined respectively as: shear stress at element i^{th} induced by shear displacement discontinuity at element j^{th}, shear stress at element i^{th} induced by normal displacement discontinuity at element j^{th}, normal stress at element i^{th} induced by shear displacement discontinuity at element j^{th}, and normal stress at element i^{th} induced by normal displacement discontinuity at element j^{th}. Finally, $xy - plane$ displacements (u) and stresses (σ) due to opening and/or slippage of discretized elements ($j = 1\ to\ N$) can be calculated for any arbitrary point in the domain using an appropriate coordinate system transformation and the principle of superposition associated with the following equations:

Displacement

$$u_x = D_x\left[2(1-\upsilon)f_y - yf_{xx}\right] + D_y\left[-(1-2\upsilon)f_x - yf_{xy}\right], \tag{19}$$

$$u_y = D_x\left[(1-2\upsilon)f_x - yf_{xy}\right] + D_y\left[2(1-\upsilon)f_y - yf_{yy}\right], \tag{20}$$

Stress

$$\sigma_{xx} = 2GD_x\left[2f_{xy} + yf_{xyy}\right] + 2GD_y\left[f_{yy} + yf_{yyy}\right], \tag{21}$$

$$\sigma_{yy} = 2GD_x\left[-yf_{xyy}\right] + 2GD_y\left[f_{yy} - yf_{yyy}\right], \tag{22}$$

$$\sigma_{xy} = 2GD_x\left[f_{yy} + yf_{yyy}\right] + 2GD_y\left[-yf_{xyy}\right], \tag{23}$$

where G is the shear modulus, υ is the Poisson's ratio, and D_x and D_y are displacement discontinuities in x and y direction, respectively. Function $f(x,y)$ represents the solution of the constant displacement discontinuity problem with a segment length of $2a$:

$$\begin{aligned} f(x,y) = -\frac{1}{4\pi(1-\upsilon)}\Big[y\left(tan^{-1}\frac{y}{x-a} - tan^{-1}\frac{y}{x+a}\right) \\ - (x-a)\ln\left(\sqrt{(x-a)^2+y^2}\right) \\ + (x+a)\ln\left(\sqrt{(x+a)^2+y^2}\right)\Big]. \end{aligned} \tag{24}$$

DDM has 2 main advantages compared with Finite Element Method (FEM) for modeling fracture mechanics: (1) computation cost is relatively low since discretization is not required in the entire simulation domain, but only along crack segments; (2) fracture propagation does not involve potential remeshing issues and it is a simple process achieved by the addition of elements at the tip. On the other hand, shortcomings associated with DDM may include: (1) potential inability to deal with nonlinearities and heterogeneities; (2) linear elastic deformation, which might not be the most accurate assumption to be used in the fracture vicinity and tip.

A flowchart detailing the process applied to estimate DSS and LF-DAS based on the numerical solution is present in **Figure 2.4**. DDM inputs are: (1) Young's modulus (E); (2) Poisson's ratio (υ); (3) horizontal stress difference ($\Delta S_H = S_{Hmax} - S_{hmin}$); (4)

element length (L_e); (5) net pressure or normal stress (P_{net}) for hydraulic fracture elements (tensile failure); (6) shear stress (σ_s) for natural fracture elements (shear failure). At the end of each time step, the tangent displacement component (u_y) (parallel to monitor well) is the DDM output that I select to store.

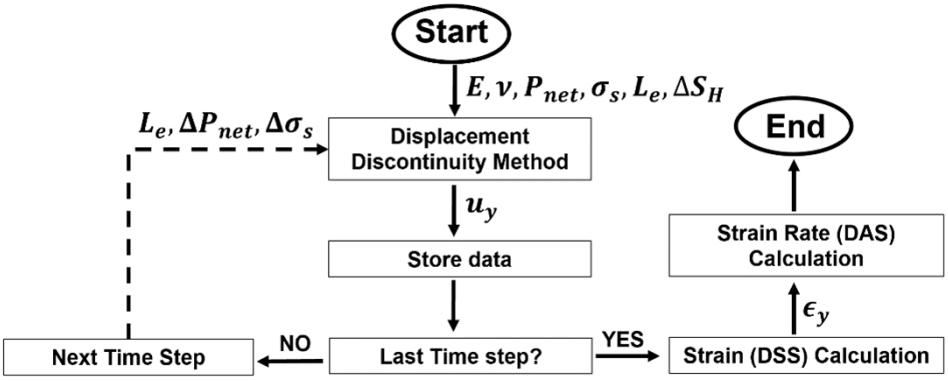

Figure 2.4–Flowchart of DSS and LF-DAS calculation using the numerical solution.

Hydraulic fracture propagation is represented in the simulation by adding rectangular elements (L_e) at the fracture tip, and fluid mechanics associated with such fractures are incorporated in the analysis by a constant adjustment of net pressure (ΔP_{net}) in each element at the end of a time step.

Taleghani and Olson (2014) proposed three different propagation-path scenarios that may take place when hydraulic and natural fractures interact: (a) hydraulic fracture crosses natural fracture and continues propagating along original path; (b) hydraulic fracture intersects natural fracture and diverts towards natural fracture system, creating a new fracture path at the end of the natural fracture; (c) hydraulic fracture intersects natural fracture and diverts along natural fracture path, however at some weak point it kinks out (**Figure 2.5**).

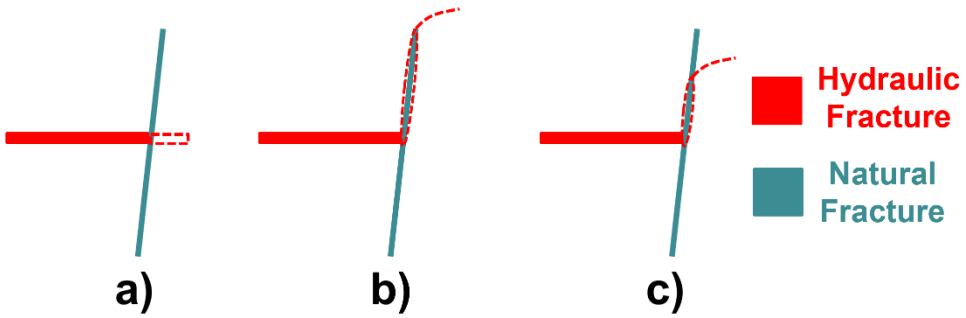

Figure 2.5–Represented by dashed lines, possible propagation pathways that hydraulic fractures (red) follow after intersecting natural fractures (dark aqua): (a) along its original direction, (b) along natural fracture creating a new path at the end, and (c) along natural fracture kinking out in a weak point.

I assume interaction between hydraulic and natural fractures when the former crosses the latter and keeps propagating along maximum horizontal stress (S_{Hmax}) direction. The aftermath is fluid leak-off, natural fracture reactivation, and posterior slippage phenomenon (motion). Fluid leak-off is represented by a constant increase in natural fracture shear stress ($\Delta\sigma_s$), which is equivalently compared to a reduction in effective normal stress on the planar discontinuity due to pore pressure increase.

In the next step of the simulation, when fracture propagation reaches the last time step, DSS is calculated. Absolute strain along the y-direction (ϵ_y) is defined as:

$$\epsilon_y = \frac{\partial u_y}{\partial y}. \tag{25}$$

Therefore, absolute strain at j^{th} position along the fiber is estimated deriving displacement in space by the application of central difference approximation and incorporation of fiber gauge length (L_G) concept, which is a topic associated with data resolution and typically ranges from 1 to 10 m in the field (Hartog, 2017; Sherman et al., 2019):

$$\epsilon_y^j = \frac{u_y^{j+\frac{L_G}{2}} - u_y^{j-\frac{L_G}{2}}}{y^{j+\frac{L_G}{2}} - y^{j-\frac{L_G}{2}}} = \frac{u_y^{j+\frac{L_G}{2}} - u_y^{j-\frac{L_G}{2}}}{L_G}. \tag{26}$$

Once DSS is calculated, LF-DAS along the fiber is estimated using the same methodology applied in the analytical solution (Eq. 16).

Time derivative of strain may enhance the numerical noise (Tan et al., 2021) of data acquired specially from simulations including hydraulic and natural fracture interactions. Thus, application of 2D Gaussian smoothing filter in some cases can simplify the interpretation process of waterfall plots.

2.2.1. Numerical Solution Validation

To validate the numerical solution, I performed a simulation of single fracture failing in tensile mode (**Figure 2.6**) and compared the magnitude of calculated normal displacement discontinuities (i.e., fracture width) with results obtained by the analytical method (Eq. 27) (Olson, 1990; Valkó and Economides 1995).

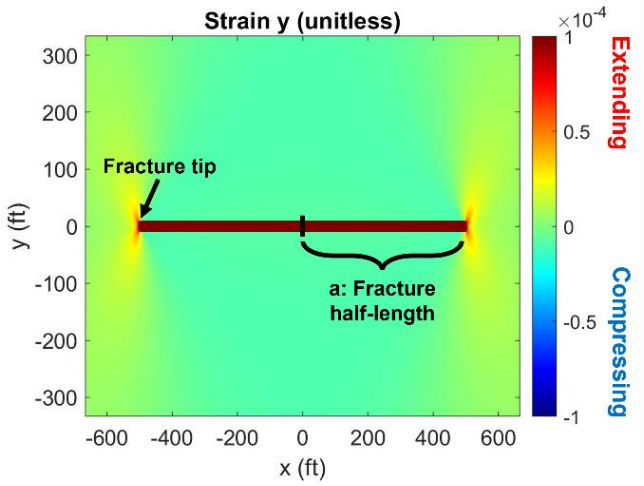

Figure 2.6–Map view ($xy-plane$) of strain at the end of numerical simulation (100 time steps) of a fracture with 500 ft half-length.

$$w(x) = \frac{4}{E'\pi}\left[(P_0\pi + P_1 a)\sqrt{(a^2 - x^2)} + P_1 x^2 \ln\left(\frac{a + \sqrt{(a^2 - x^2)}}{x}\right)\right], \qquad (27)$$

Where $w(x)$ is the fracture width as a function of space for a linear net pressure distribution in the fracture, E' is the plane strain modulus (Eq. 3), a is the fracture half-

length, and P_0 and P_1 are the linear and angular coefficients of the net pressure equation (Eq. 28), respectively.

$$P_{net}(x) = P_0 + P_1 x \, . \tag{28}$$

In this case, 200 rectangular elements are used to discretize a fracture with constant net pressure (i.e., $P_{net} = P_0$). Consequently, Equation 27 is simplified to:

$$w(x) = \frac{4P_0}{E'}\left[\sqrt{(a^2 - x^2)}\right]. \tag{29}$$

Table 2.1 shows the magnitude of variables used in the validation process of numerical solution.

Table 2.1–Parameters used in the validation of numerical solution.

Fracture half-length (ft)	Net pressure (psi)	Poisson's Ratio (Unitless)	Young's Modulus (psi)
500	50	0.25	$4x10^6$

Figure 2.7 shows that fracture aperture estimated by the numerical solution is slightly above results obtained with analytical solution. The absolute error is negligible along fracture half-length, reaching maximum values near the fracture tip (i.e., x/a ratio close to 1).

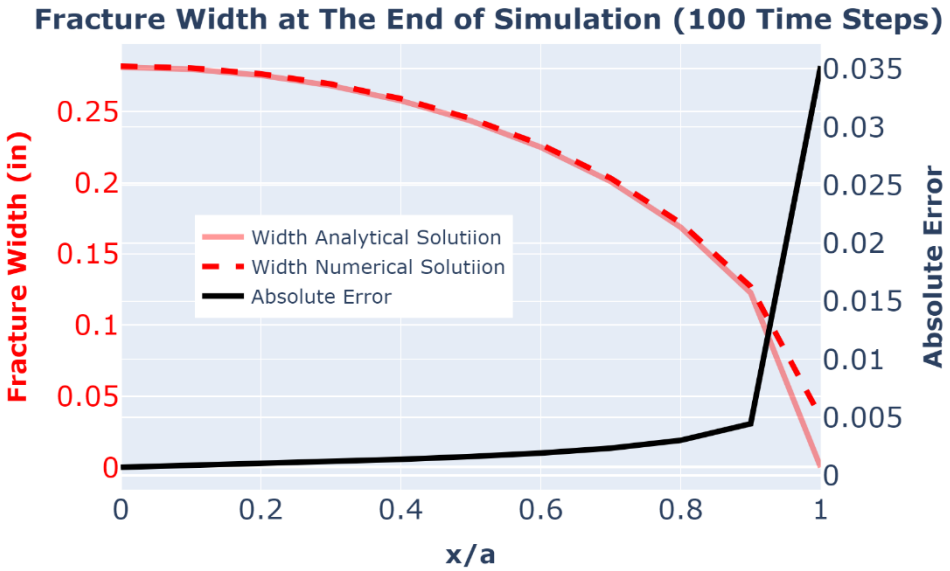

Figure 2.7–Fracture width estimated by analytical and numerical methods are represented by full red curve and dashed red curve, respectively. The relative error at the end of a simulation comprised by 100 time steps is shown by the full black curve.

2.3. Machine Learning and Deep Learning

Machine learning is a field of study that gives computers the ability to learn without explicitly being programed (Samuel, 1967). The technology takes the approach of letting computers learn to program themselves through experience when exposed to data (i.e., training stage). The model performance is evaluated using data that is held out from the training data (i.e., testing stage). The result is a model that can be used in the future with different sets of data.

Successful machine learning algorithms may have three different functions (Malone et al., 2020): (1) descriptive, meaning that the system uses the data to explain what happened; (2) predictive, meaning the system uses the data to predict what will happen; or (3) prescriptive, meaning the system will use the data to make suggestions about what action to take.

According to James et al. (2021) there are three subcategories of machine learning models: (1) supervised, which is trained with labeled datasets and may be applied in regression or classification problems; (2) unsupervised, which looks for patterns or trends

in unlabeled data; and (3) reinforcement, which trains machines through trial and error to take the best action by establishing a reward system.

Deep learning (DL) is a subset of machine learning in which the tasks are broken down and distributed onto algorithms that are organized in consecutive layers (Huang et al., 2019). Each layer builds up on the output from the previous layer. Together the layers constitute an artificial neural network (ANN) that mimics the distributed approach to problem-solving carried out by neurons in a human brain (**Figure 2.8**).

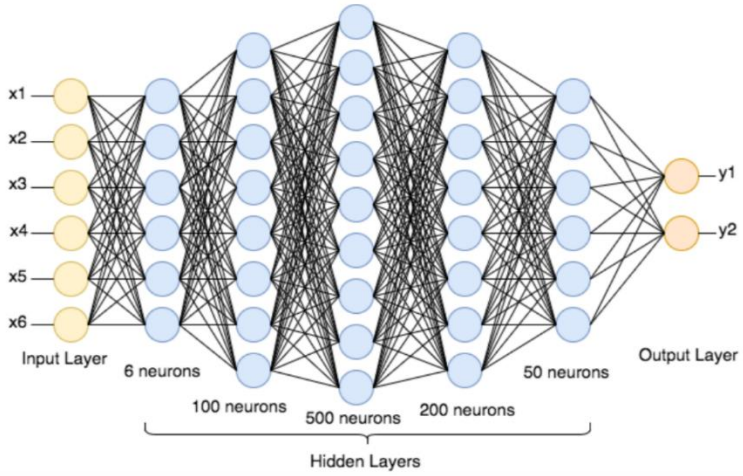

Figure 2.8–Schematic architecture of a deep learning model. It is represented by a combination of input, hidden and output layers containing neurons. Adapted from Bahi and Batouche (2018).

The deep learning model is composed by input, hidden and output layers, each with multiple neurons. Weights are parameters connecting neurons from adjacent layers. The linear combination of neurons from input layer and respective weights is the input of a nonlinear activation function (e.g., Sigmoid, Hyperbolic Tangent [Tanh], Rectified Linear Unit [ReLU], Leaky ReLU, Exponential Linear Unit [ELU]), which outputs the neuron of a subsequent hidden layer (i.e., forward propagation) during the training process (**Figure 2.9**) (Alanis et al., 2019).

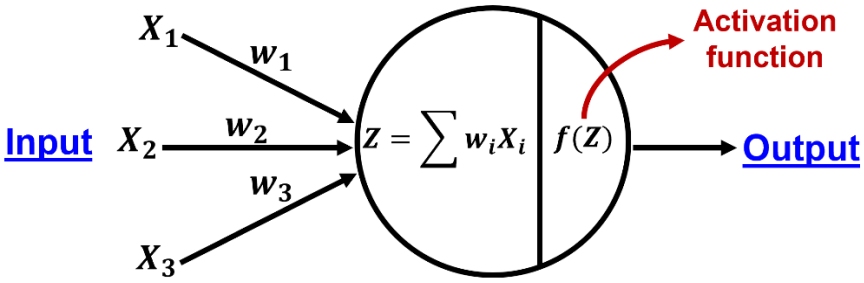

Figure 2.9–Linear combination of neurons from input layer and respective weights working as input of activation function. The function incorporates nonlinearities in the process and outputs one neuron of subsequent layer.

A specific loss function (e.g., mean squared error, mean absolute error) is selected to calculate the error between estimated and true output values at the end of a forward pass. The backward propagation is performed considering loss function derivatives with respect to weights coupled with a specific learning rate (e.g., gradient descent optimizer). The purpose of backward pass is to update the model weights and consequently minimize the loss function (Hastie et al., 2009). Therefore, the loss function magnitude of a model that works properly during training stage will tend to reduce as the number of forward/backward cycles (i.e., epochs) increases.

2.3.1. Deep Learning Algorithm and Fracture Width Estimation

In this project, the numerical framework generates all necessary data to train and test the deep learning (DL) algorithm. For fracturing scenarios composed of single and multiple hydraulic fractures, the DDM software performs simulations in which several observation wells are deployed in the field to monitor fracture propagation (Gurjao et al., 2022a). Tangent displacement component (u_y) is the output I select to store for posterior application with the DL model.

For each monitor well at a certain distance from the operation well (i.e., X location), data is generated in meshgrid style (i.e., image format). Each grid point is located at a specific position in space (X and Y) and has time (t); moreover, it is characterized by one u_y value (**Figure 2.10**).

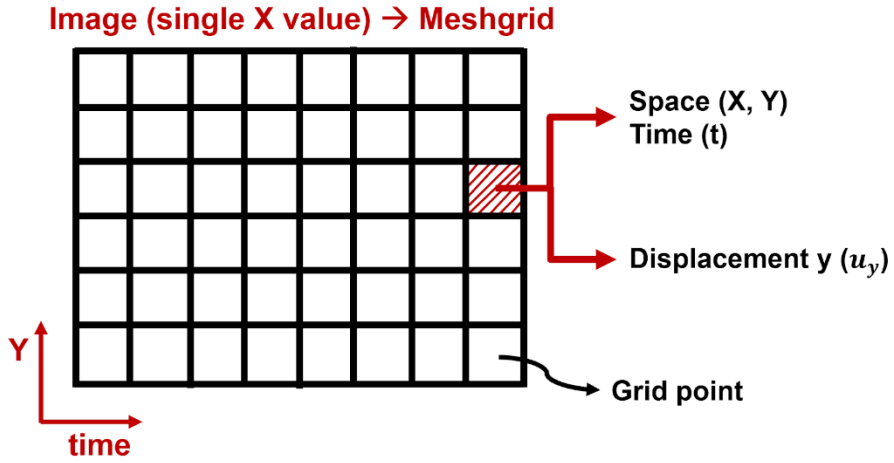

Figure 2.10–Generic meshgrid dataset for the specific case where monitor and operation wells are separated by distance X, with details for components of each grid point (i.e., space, time, and displacement y).

In the next phase, I work with the Artificial Neural Network (ANN) algorithm. Space (X and Y) and time (t) are used as input features, and axial displacement (u_y) as output variable (Gurjao et al., 2022b). The selected architecture of ANN is composed of seven hidden layers with the number of neurons varying from 10 to 100 per layer (**Figure 2.11**).

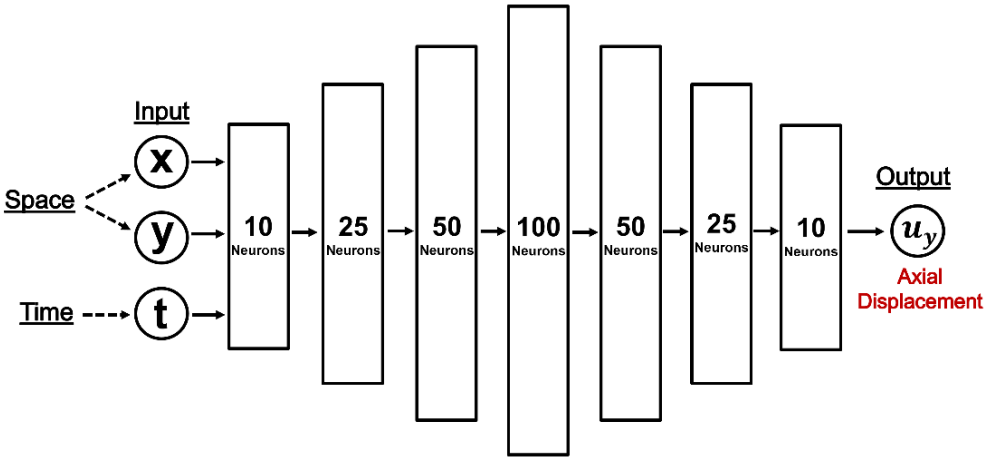

Figure 2.11– Selected architecture of ANN algorithm used in this project: (1) The input layer is composed of three features (X, Y, and time); (2) There are seven hidden layers with the number of neurons varying from 10 to 100; and (3) The output layer consists of the u_y variable.

I apply hyperbolic tangent ($tanh$) as the nonlinear activation function in each hidden layer. The adaptive moment estimation (*Adam*) optimizer is used with a constant learning rate of $1e^{-4}$. The batch size and number of epochs are specified to be 1000. In terms of loss function, mean squared error (MSE) or L2 loss is used in the dataset representing the scenario composed by single hydraulic fracture, and mean absolute error (MAE) or L1 loss with data representing the scenario consisting of multiple hydraulic fractures:

$$MSE = \frac{1}{n}\sum_{i=1}^{n}(Y_i - \hat{Y}_i)^2, \tag{30}$$

$$MAE = \frac{1}{n}\sum_{i=1}^{n}\left|Y_i - \hat{Y}_i\right|, \tag{31}$$

where n is the total number of observations, Y_i is the true output, and $\hat{Y}_i$ is the predicted output from the ANN model.

Since I'm working with tiny outputs, squaring the difference between true and predicted values can result in negligible errors even when the magnitude of these elements is far from close, consequently some weights and biases of ANN may be barely updated, and the algorithm will tend to don't present an optimum performance. Thus, in the dataset composed by multiple fractures opening, I use L1 instead of L2 loss function to examine if regression model could achieve better results.

In data wrangling stage: (1) there is no need to clean up data since it is generated by my simulator; (2) image raw data is reorganized in column-wise format; and (3) ANN inputs and outputs are normalized to range between 0 and 1:

$$Z_{normalized} = \frac{Z - Z_{min}}{Z_{max} - Z_{min}}. \tag{32}$$

In data splitting, out of 13 monitor wells, a dataset of 12 is used for training and 1 for testing. The training stage is performed with two objectives: (1) avoid overfitting and (2) minimize ANN loss function as the number of epochs increases. During the testing

stage, the trained model is applied to predict axial displacement in the left monitor well. Once u_y is estimated, I calculate the relative error between estimated and true values (results are displayed in the waterfall plot). In the next step, low-frequency distributed acoustic sensing (LF-DAS) is calculated by deriving predicted tangent displacement component sequentially in space and time (**Figure 2.12**).

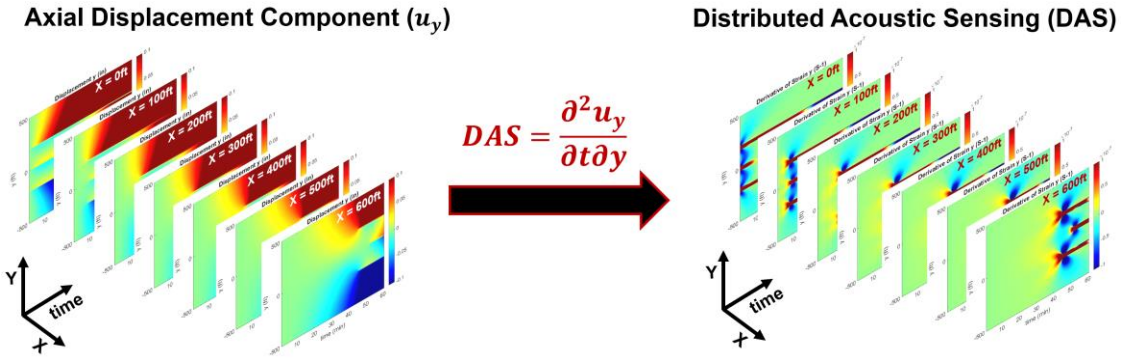

Figure 2.12– Dataset of specific scenario composed by 3 hydraulic fractures. On the left, axial displacement component (u_y) of 7 monitor wells deployed in different locations (i.e., X = 0, 100, 200, 300, 400, 500 and 600 ft). On the right, corresponding LF-DAS data of each X position obtained deriving u_y sequentially in space and time.

I observe that u_Y is a continuous variable before fracture hit at monitor well (**Figure 2.13**), and it becomes discontinuous right at the hit moment (**Figure 2.14)**. The former is interpreted as a direct effect of rock deformation, and the latter as a consequence of rock breakdown.

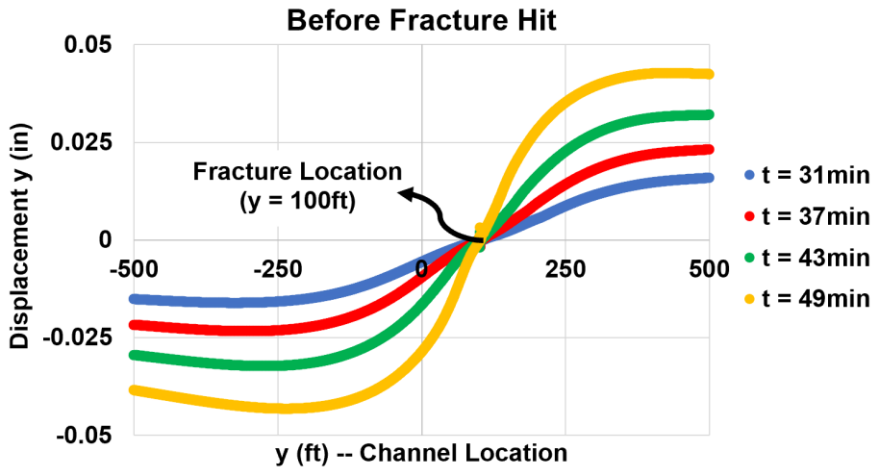

Figure 2.13–Dataset of specific fracture scenario characterized by: (1) single hydraulic fracture located at y = 100 ft; (2) monitor well placed at X = 300 ft (i.e., the distance between operation and monitor wells); and (3) fracture hit at t = 54.7 min. In this graph, predicted axial displacement of four time steps before fracture hit are plotted against channel location (continuous data). As time advances, fracture approaches the fiber and rock deformation at monitor well location increases.

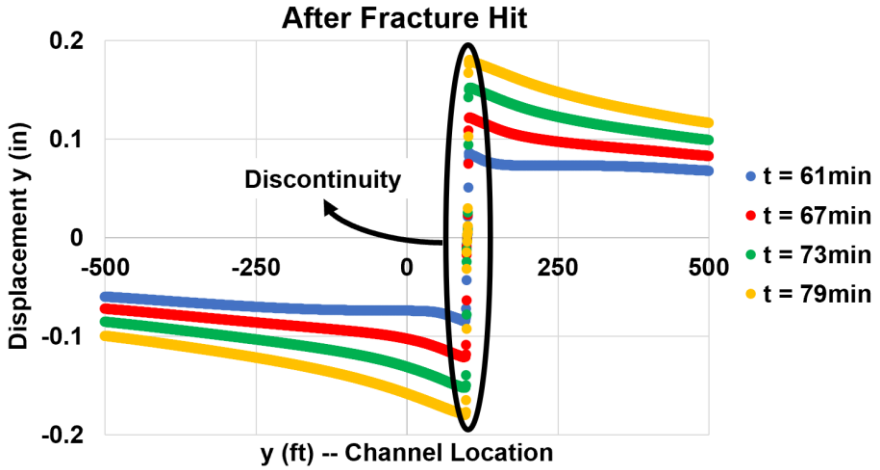

Figure 2.14–Dataset of specific fracture scenario characterized by: (1) single hydraulic fracture located at y = 100 ft; (2) monitor well placed at X = 300 ft (i.e., the distance between operation and monitor wells); and (3) fracture hit at t = 54.7 min. In this graph, predicted axial displacement of four time steps after fracture hit are plotted against channel location (discontinuous data). As time increases, rock pulls apart even more at monitor well location.

Starting at the hit moment at a specific location, I measure for each time step the "discontinuity length" (term coined in this work) observed in the plot of predicted tangent displacement component versus channel location (**Figure 2.15**). Errors between this term and the true fracture width calculated by DDM software are negligible. Therefore, I

demonstrate for the first time that "discontinuity length" may be related to fracture aperture.

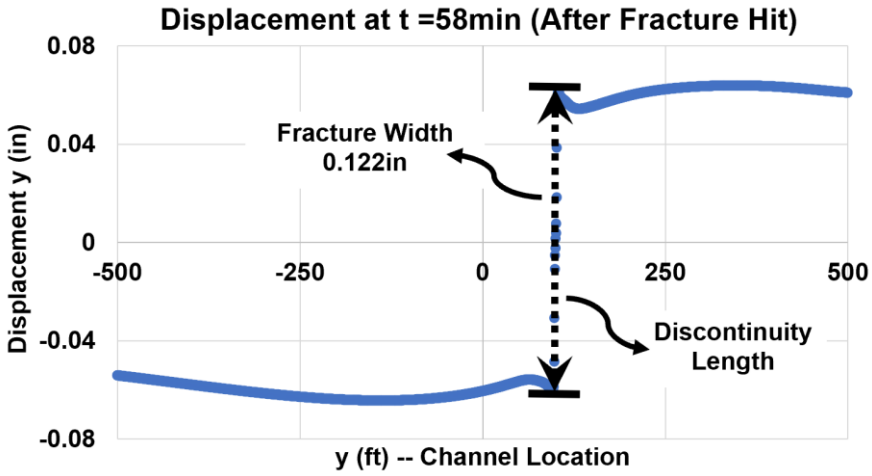

Figure 2.15–Dataset of specific fracture scenario characterized by: (1) single hydraulic fracture located at y = 100 ft; (2) monitor well placed at X = 300 ft (i.e., the distance between operation and monitor wells); and (3) fracture hit at t = 54.7 min. In this graph, predicted axial displacement at t = 58 min (after fracture hit) is plotted against channel location (discontinuous data). The magnitude of "Discontinuity length" is 0.122 in, and it is approximately the fracture width.

Using the developed spatio-temporal deep learning model, I predict the tangent displacement component in multiple X locations. The "discontinuity length" method is applied in each of these places to estimate fracture width along time, which leads to improvement of hydraulic fracture geometry characterization beyond the near wellbore region. Finally, the relative error between estimated and true widths is calculated.

2.4. Fracture Width Estimation in the Field Using "Discontinuity Length" Method

LF-DAS field data is acquired in the form of optical phase change ($\Delta\Phi$) in radian units (Lindsey et al., 2020), which is linear proportional to strain perturbation according to Lindsey and Martin (2021):

$$\Delta\Phi = \frac{4\pi n L_G \psi}{\lambda}\epsilon, \tag{33}$$

where n is fiber core refractive index (≈1.45 for pure silica glass), L_G is fiber gauge length in meters (known value in the field), ψ is the Pockels coefficient of fiber (≈0.79 for pure silica glass), λ is the laser light wavelength that commonly falls in the near-infrared range (≈1,550nm), and ϵ is the unitless axial strain measurement along fiber axis. According to Liu et al. (2020), recorded optical phase change in the field should be differentiated in time (after filtering process to remove noise) in order to be linear correlated with strain rate along the fiber:

$$\dot{\Delta\Phi} = \frac{4\pi n L_G \psi}{\lambda} \dot{\epsilon}, \tag{34}$$

where $\dot{\Delta\Phi}$ is optical phase change derived in time, and $\dot{\epsilon}$ is strain rate. I can solve for strain rate multiplying $\dot{\Delta\Phi}$ by the constant $\frac{\lambda}{4\pi n L_G \psi}$. Then, axial displacement can be calculated integrating strain rate sequentially in time and space:

$$u_y = \iint \dot{\epsilon} dt dy. \tag{35}$$

Finally, I propose to use calculated field u_y to estimate fracture width at monitor well location along time (starting at fracture hit instant) measuring discontinuity magnitudes (i.e., applying the "discontinuity length" method).

3. RESULTS AND DISCUSSIONS

This chapter is divided in four sections: (1) analytical solution, (2) numerical solution, (3) deep learning algorithm and fracture width estimation, and (4) fracture width estimation using strain dataset from the stress shadow zone.

I apply the analytical technique in a sensitivity analysis to evaluate the impact of rock and fluid parameters on strain time histories generated by single fracture failing in tensile mode. The numerical technique is used to model strain fields of advanced scenarios composed by multiple fractures failing in tensile and shear modes. In this case five objectives are listed: (1) determine the influence of natural fracture (NF) geometry on strain and cluster efficiency, (2) quantify fiber gauge length (GL) impact on strain, (3) characterize strain fields when pumping stops, (4) identify fracture hit moment based on stress derivative, and (5) analyze how stress varies as a function of perpendicular distance from the fracture face (i.e., stress shadow transmissibility).

The third section is dedicated to develop deep learning (DL) models using numerical synthetic data (two scenarios: single and multiple hydraulic fractures) from multiple monitor wells to predict strain fields in any position and time. The goal is to integrate the DL model and "discontinuity length" method (proposed in this project) to improve fracture geometry characterization estimating width in multiple locations as a function of time. In the last section, synthetic data generated by the numerical model is used to train and test machine learning algorithms (e.g., multilinear regression, support vector regression, artificial neural network, and random forest) inputting strain fields from the stress shadow region and outputting fracture aperture.

3.1. Analytical Solution

In this work applying the analytical technique for simulation time span of 300 seconds, I consider a single perforation cluster opening and cross-well fiber deployment with monitor and operation wells distancing 100 ft. Fracture height and Poisson's ratio are constant in all simulated scenarios assuming 150 ft and 0.25, respectively. In the

sensitivity analysis studies, Young's modulus rages from $1x10^6$ to $7x10^6$ psi, fluid viscosity varies from 5 to 20 cp, and injection rate from 5 to 20 bbl/min.

Table 3.1 shows rock property (i.e., Young's modulus) and fluid properties (i.e., viscosity and injection rate) used in base case scenario.

Table 3.1–Parameters used in base case scenario.

Young's Modulus (psi)	Fluid Viscosity (cp)	Injection Rate (bbl/min)
$4x10^6$	10	10

Typical characteristics present in field data (**Figure 3.1**) can be observed in the synthetic absolute strain (DSS) and strain rate (LF-DAS) waterfall plots (**Figure 3.2a** and **Figure 3.2b**) such as heart-shaped pattern from a fracture approaching the fiber, stress shadow (i.e., compression zone adjacent to an opening fracture) and fracture-hit. This comparison indicates that the analytical technique captures important features properly and represents its qualitative validation.

Propagation of hydraulic fracture right after its hit in monitor well at t = 86.9 seconds is revealed in LF-DAS synthetic data by hot colors that represent the extension phenomena. Furthermore, strain rate magnitude decreases following the hit, which is a direct effect of the net pressure reduction typically associated with KGD fracture model (**Figure 3.2c**). I recognize the potential artificiality of drop in net pressure estimated by KGD model and anticipate that the same principle applies to an increase in net pressure along time (i.e., it will result in an increase in strain magnitude along time after the hit).

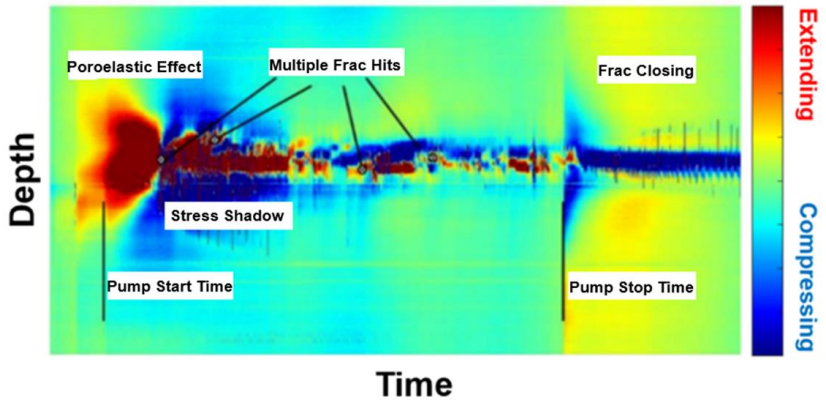

Figure 3.1–Low-frequency DAS field data highlighting classic features associated with propagation of hydraulic fractures: (1) heart-shaped pattern, (2) fracture hits, and (3) stress shadow surrounding the opening fracture. Adapted from Richter et al. (2019).

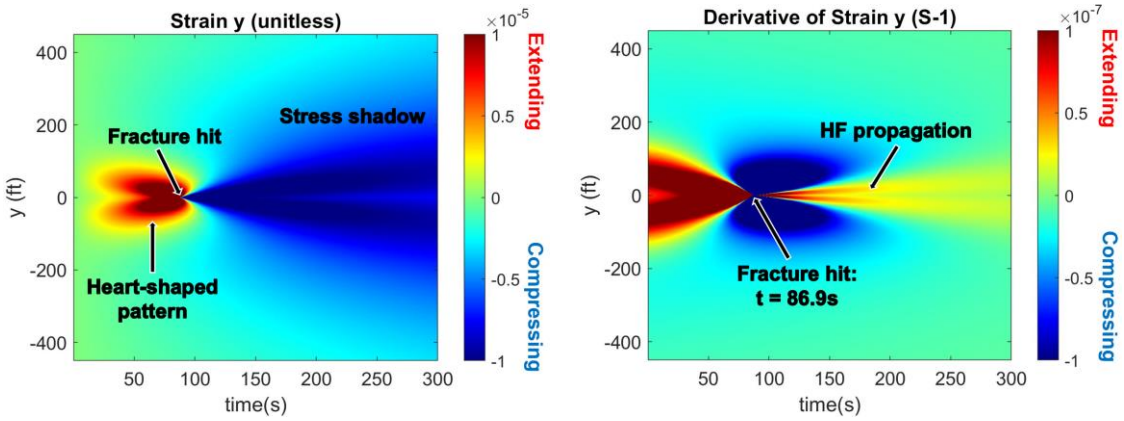

a. Distributed Strain Sensing (DSS)

b. Low-Frequency Distributed Acoustic Sensing (LF-DAS)

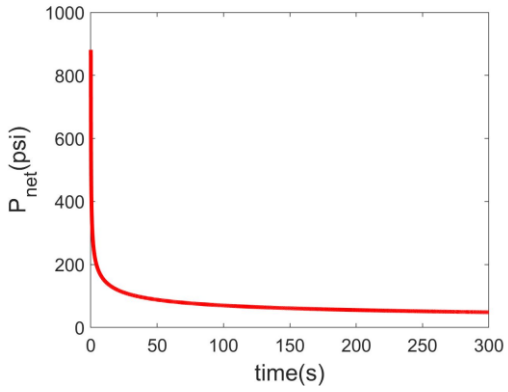

c. Net pressure plot

Figure 3.2–(a) DSS and (b) LF-DAS synthetic data of base case scenario applying the analytical solution. (c) Net pressure calculated using the 2D KGD fracture model for this specific case. Typical features present in field data are observed: heart-shaped pattern of a fracture approaching the fiber, stress shadow, and fracture-hit (t = 86.9s) followed by its propagation.

I perform the first sensitivity analysis by varying Young's modulus and keeping constant fluid viscosity and injection rate with the same values of the base case scenario. **Table 3.2** shows parameters used in simulations.

Table 3.2–Parameters used in sensitivity analysis 1.

	Young's Modulus (psi)	Fluid Viscosity (cp)	Injection Rate (bbl/min)
Scenario *a*	$1x10^6$	10	10
Scenario *b*	$7x10^6$	10	10

Figure 3.3 shows DSS and LF-DAS synthetic data obtained in Sensitivity Analysis 1. Fracture hits monitor well at t = 122.9 seconds and t = 75.6 seconds in scenarios *a* and *b*, respectively. Comparing these results with the base case scenario (**Table 3.1**), where the hit takes place at t = 86.9 seconds, I observe that the fracture propagates faster in formations with high Young's modulus.

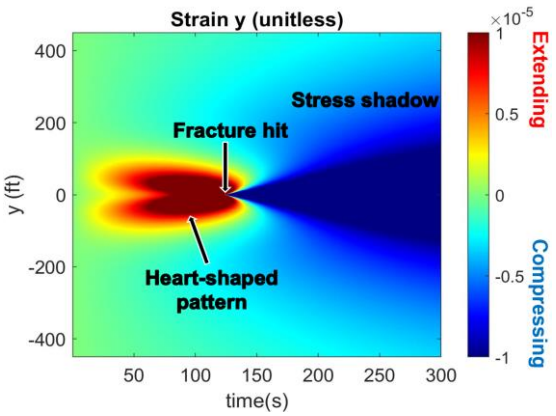

a. DSS → Scenario *a*

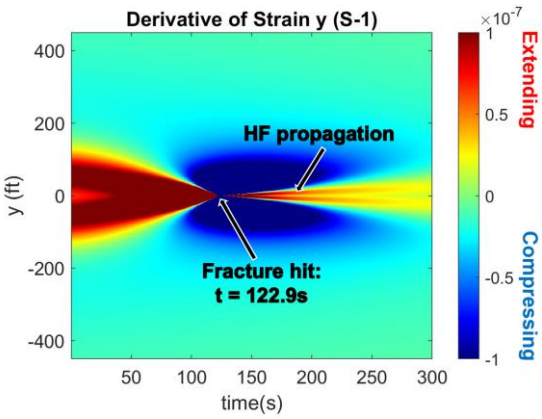

b. LF-DAS → Scenario *a*

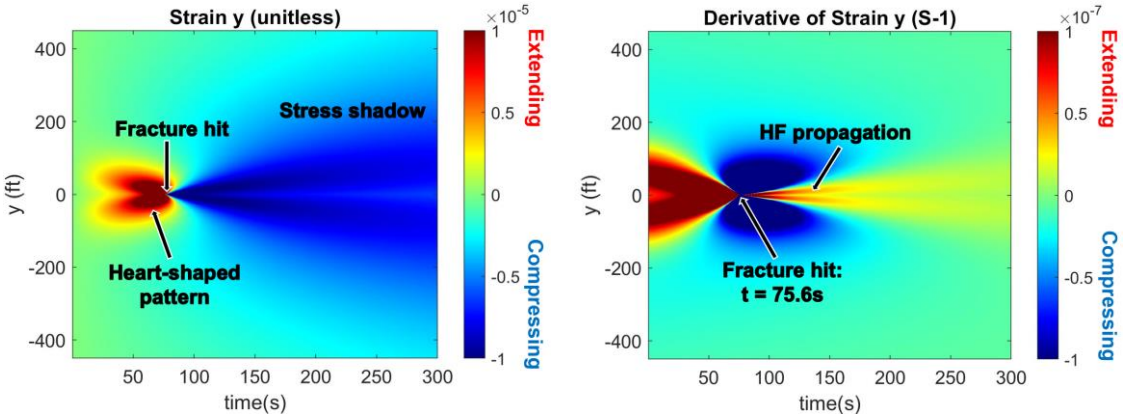

c. DSS → Scenario *b* d. LF-DAS → Scenario *b*

Figure 3.3–DSS and LF-DAS results of Sensitivity Analysis 1. Fracture hits monitor well faster in scenario *b* where Young's modulus is higher.

Figure 3.4 shows that over time the fracture generated in scenario *a* (lower Young's modulus) has greater average width.

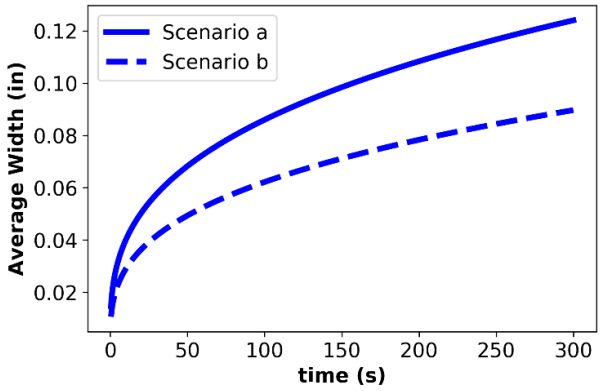

Figure 3.4–Average fracture width over time of scenarios *a* and *b* (Sensitivity Analysis 1: varying Young's modulus).

I perform the second sensitivity analysis by varying fluid viscosity and keeping constant Young's modulus and injection rate with the same values of the base case scenario. **Table 3.3** shows the parameters used in simulations.

Table 3.3–Parameters used in sensitivity analysis 2.

	Young's Modulus (psi)	Fluid Viscosity (cp)	Injection Rate (bbl/min)
Scenario *a*	$4x10^6$	5	10
Scenario *b*	$4x10^6$	20	10

Figure 3.5 shows DSS and LF-DAS synthetic data obtained in Sensitivity Analysis 2. Fracture hits monitor well at t = 73.1 seconds and t = 103.4 seconds in scenarios *a* and *b*, respectively. Comparing these results with the base case scenario (**Table 3.1**), where the hit takes place at t = 86.9 seconds, I note that the fracture propagates faster when low viscosity fluids are used.

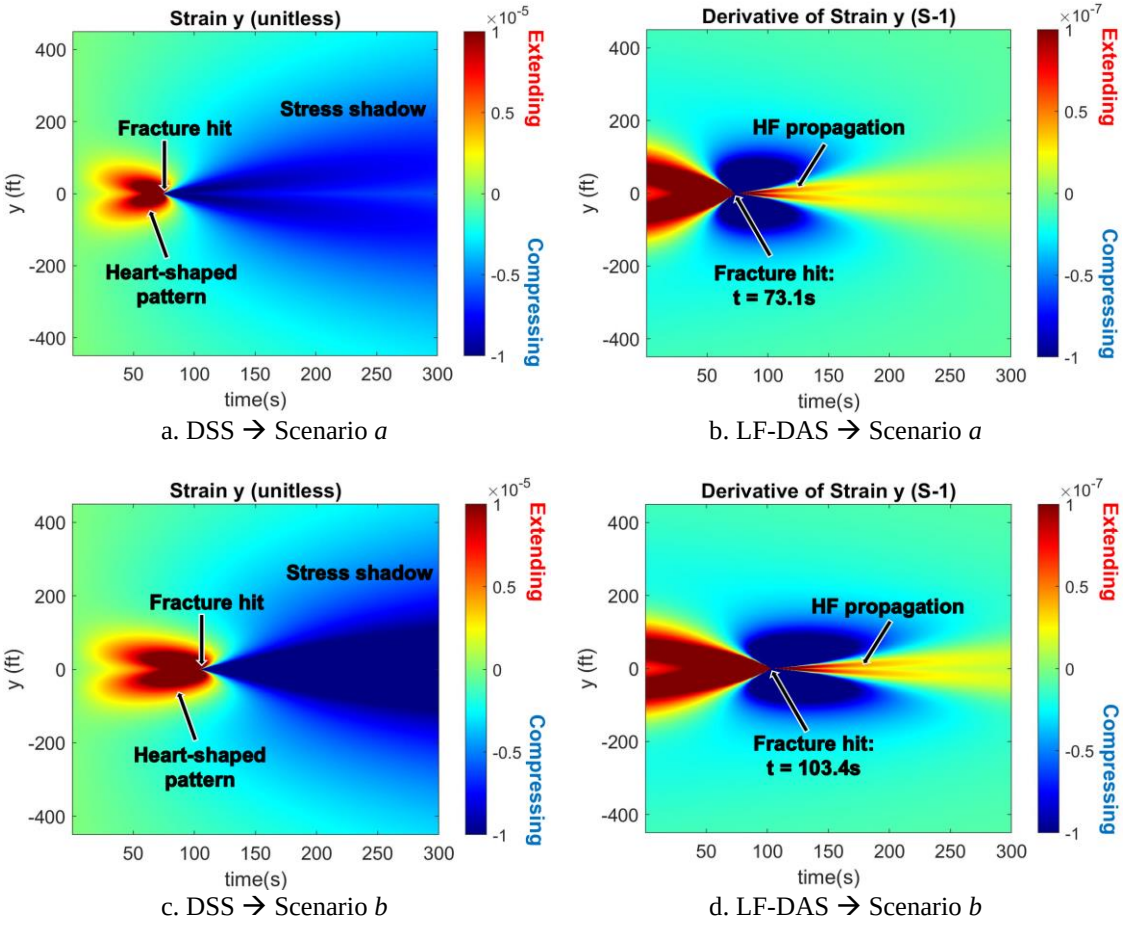

a. DSS → Scenario *a*

b. LF-DAS → Scenario *a*

c. DSS → Scenario *b*

d. LF-DAS → Scenario *b*

Figure 3.5–DSS and LF-DAS results of Sensitivity Analysis 2. Fracture hits monitor well faster in scenario *a* where the fluid viscosity is lower.

Figure 3.6 shows that over time the fracture generated in scenario *b* (higher fluid viscosity) has greater average width.

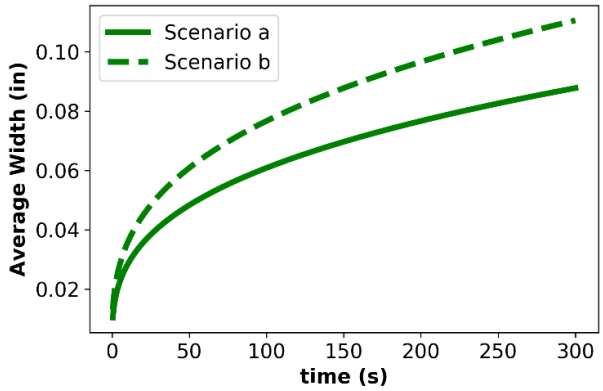

Figure 3.6–Average fracture width over time of scenarios *a* and *b* (Sensitivity Analysis 2: varying fluid viscosity).

I perform the third sensitivity analysis varying injection rate and keeping constant Young's modulus and fluid viscosity with the same values of the base case scenario. **Table 3.4** shows the parameters used in simulations.

Table 3.4–Parameters used in sensitivity analysis 3.

	Young's Modulus (psi)	**Fluid Viscosity (cp)**	**Injection Rate (bbl/min)**
Scenario *a*	$4x10^6$	10	5
Scenario *b*	$4x10^6$	10	20

Figure 3.7 shows DSS and LF-DAS synthetic data obtained in Sensitivity Analysis 3. Fracture hits monitor well at t = 146.2 seconds and t = 51.7 seconds in scenarios *a* and *b*, respectively. Comparing these results with the base case scenario (**Table 3.1**), where the hit takes place at t = 86.9 seconds, I note that under the assumption of high fluid efficiency, the fracture propagates faster at injecting high rates.

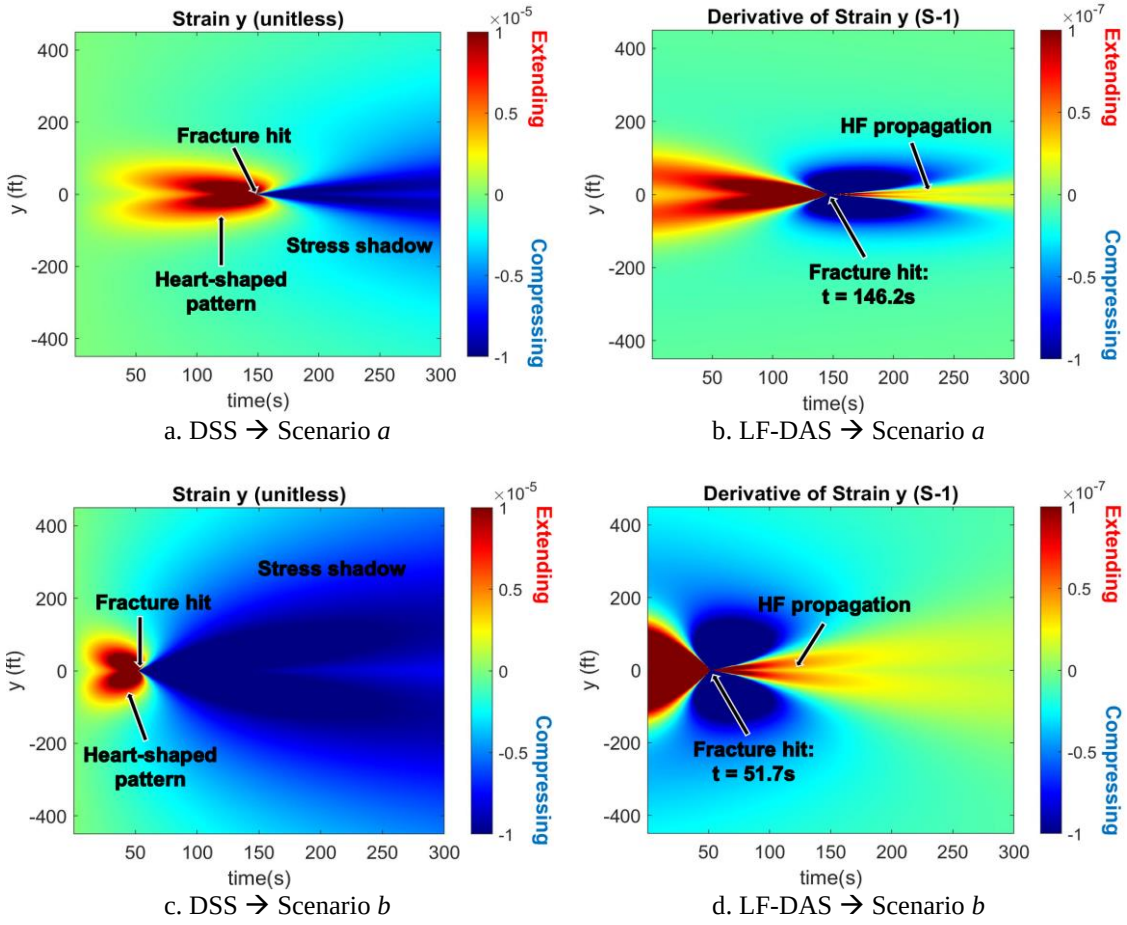

a. DSS → Scenario *a*

b. LF-DAS → Scenario *a*

c. DSS → Scenario *b*

d. LF-DAS → Scenario *b*

Figure 3.7–DSS and LF-DAS results of Sensitivity Analysis 3. Fracture hits monitor well faster in scenario *b* where injection rate is higher.

Figure 3.8 shows that over time the fracture generated in scenario *b* (higher injection rate) has greater average width.

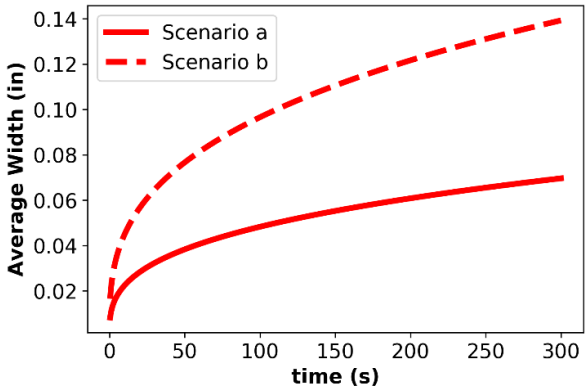

Figure 3.8–Average fracture width over time of scenarios *a* and *b* (Sensitivity Analysis 3: varying injection rate).

Table 3.5 summarizes qualitatively how an increase in Young's modulus (E), fluid viscosity (μ), or injection rate (i) can impact the fracture propagation speed (i.e., fracture hit) detected in strain waterfall plots. These results (1) confirm important known trends (Valkó and Economides 1995), (2) indicate that strain type of data is sensitive to a series of properties associated with the hydraulic fracturing treatment, (3) reveal that assuming a high fluid efficiency, injection rate is the variable with greatest impact on fracture propagation speed and average fracture width, and (4) indicate that field data may be used to infer the magnitude of a variety of rock/fluid parameters.

Table 3.5–Qualitative review of fracture propagation speed when the specified parameter is increased individually.

Parameter	Fracture propagation speed
$\uparrow E$	High
$\uparrow \mu$	Low
$\uparrow i$	High

The integration of DSS data and fracture geometry characteristics reveals: (1) if injection rate is constant, the heart-shaped pattern size is directly proportional to average fracture width, and (2) if injection rate varies, the heart-shaped pattern size is inversely proportional to average fracture width.

3.2. Numerical Solution

I apply the numerical technique for simulation time span of 1 hour, to model multiple perforation clusters (e.g., 5) and a cross-well fiber deployment in the base case scenario. Both horizontal wells are drilled perpendicular to maximum horizontal stress (S_{Hmax}); consequently, transverse hydraulic fractures are generated in a non-reverse stress regime. Adopted fiber gauge length is on the order of 1 m. Pressure distribution in each perforation cluster is linear, decreasing from wellbore location towards the fracture tip. Fluid leak-off is represented by an adjustment of 1.75 psi in shear and normal stresses at the end of each time step. Completion and geomechanical parameters applied in simulations appear in **Table 3.6**.

Table 3.6–Parameters used in numerical simulation.

Completion Parameters		**Geomechanical Parameters**		
Stage Length (ft)	Cluster Spacing (ft)	Poisson's Ratio (Unitless)	Young's Modulus (psi)	Hori. Stress Diff. (psi)
200	50	0.25	$4x10^6$	$1x10^3$

Hydraulic fracture propagation speed (**Table 3.7**) is predefined with HFs 1 and 5 located respectively on top and bottom of the stage advancing with greatest speed, and HF 3 placed in the center propagating with smallest speed due to stress shadow effect.

Table 3.7– Hydraulic fracture propagation speed.

HFs 1 and 5 (ft/min)	HFs 2 and 4 (ft/min)	HF 3 (ft/min)
2.75	2.45	2.05

DSS and LF-DAS modeling results (**Figure 3.9**) properly represent classic features present in field data: the heart-shaped pattern from a fracture approaching the fiber, stress shadow (i.e., compression zone adjacent to an opening fracture), and fracture-hit.

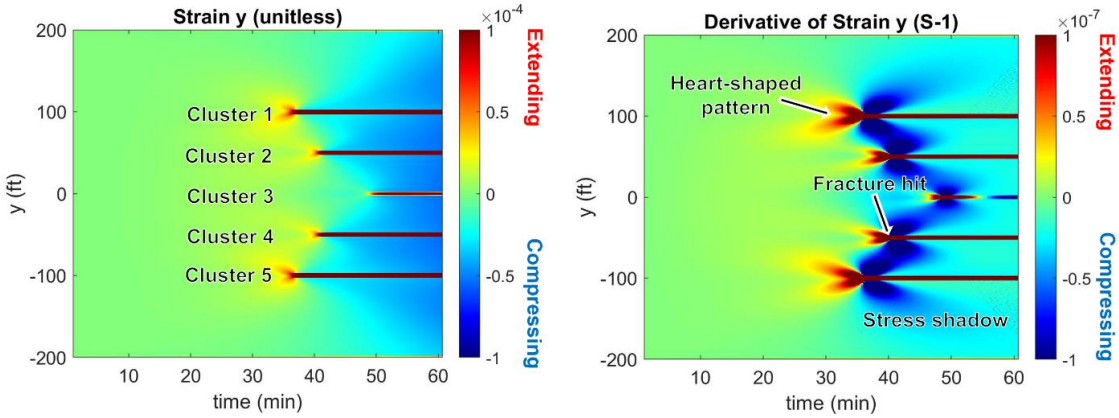

a. Distributed Strain Sensing (DSS)

b. Low-Frequency Distributed Acoustic Sensing (LF-DAS)

Figure 3.9–(a) DSS and (b) LF-DAS modeling results of base case scenario consisting of 5 perforation clusters. Typical characteristics present in field data can be observed more clearly in the LF-DAS waterfall plot: fracture approaching the fiber pictured as heart-shaped pattern, fracture hits, and stress shadow.

Figure 3.10 shows four different examples of LF-DAS field data highlighting traditional patterns that are observed in the synthetic data. This comparison represents a qualitative validation of the numerical framework developed in this project to simulate strain fields generated during the propagation of fracture systems.

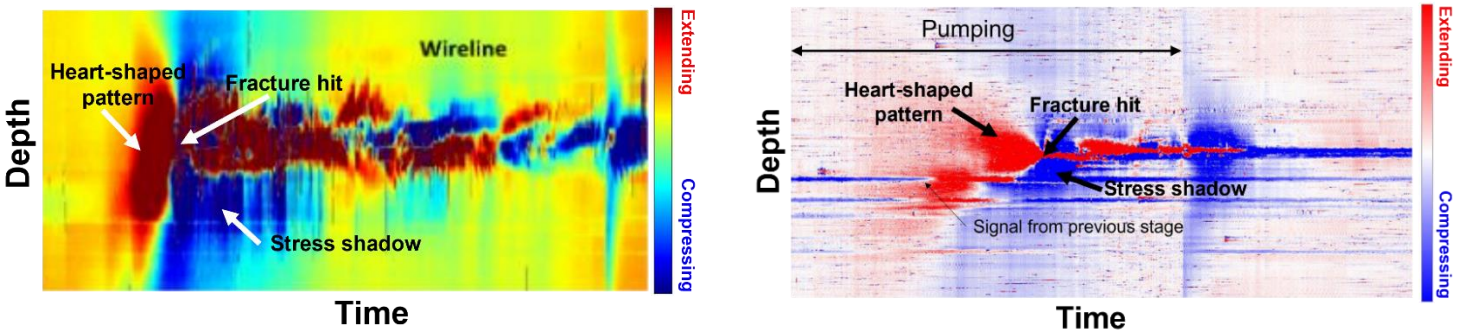

a. LF-DAS [Adapted from Richter et al. (2019)].

b. LF-DAS [Adapted from Wang et al. (2021)].

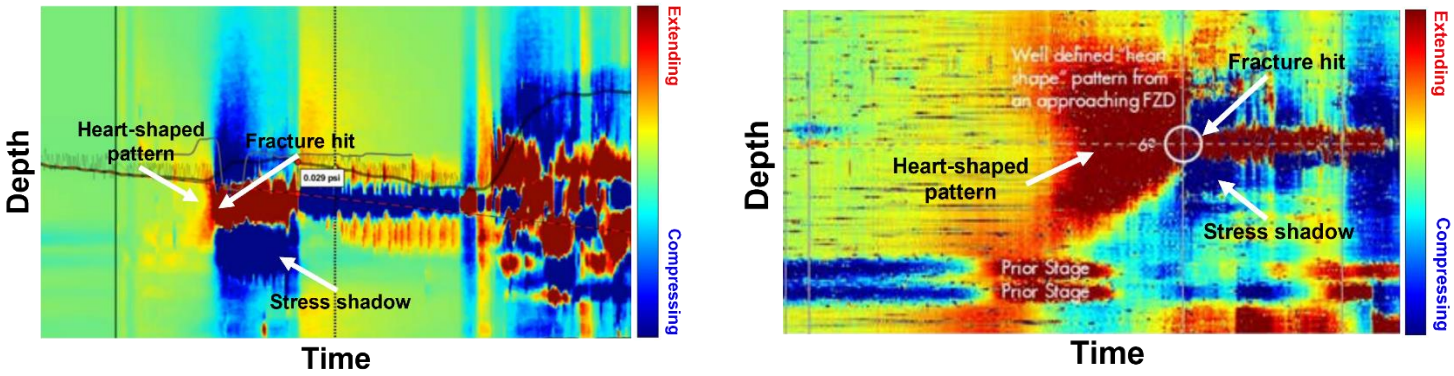

c. LF-DAS [Adapted from Elliott et al. (2022)].

d. LF-DAS [Adapted from Ugueto et al. (2022)].

Figure 3.10–Four LF-DAS field examples showing traditional features modeled by the numerical framework developed in this project: the heart-shaped pattern of a fracture approaching the fiber, stress shadow and fracture hit.

The sum of strain rate is an approach that may be used to identify fracture hit location and estimate cluster spacing (**Figure 3.11**).

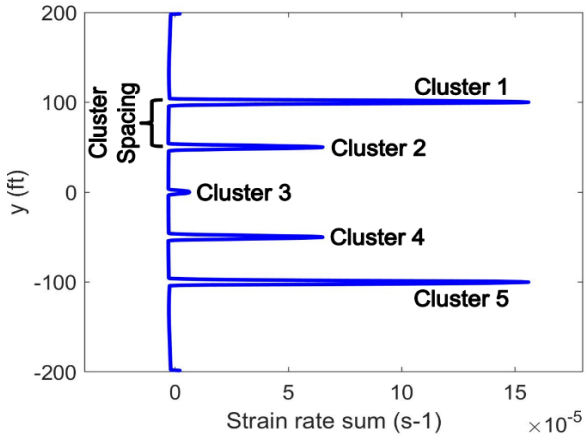

Figure 3.11–Strain rate sum of base case scenario. Individual spikes and distance between consecutives spikes represent the cluster location and spacing, respectively.

Reviewing the synthetic strain data from numerical and analytical techniques, I observe that both present different polarities in the fracture corridor immediately after the fracture hit. The former is associated with extension agreeing with field data, and the latter is associated with compression. This difference is related to the method applied in both techniques to measure strain fields. The fiber gauge length concept is used in numerical simulations and in field operations to estimate the approximate strain magnitude over a

specific length, whereas Hooke's law approach is applied in analytical simulations to assess strain magnitudes pointwise.

The presence of natural fractures (NF) in many unconventional reservoirs has been confirmed by several geological studies (Curtis, 2002; Gale and Holder, 2010). Many shale outcrops, cores, and image logs contain fractures or fracture traces, and microseismic event patterns associated with hydraulic fracture stimulation have been ascribed to natural fracture reactivation (Gale et al., 2014; Gamboa et al., 2014). Moreover, natural fractures have long been suspected as a factor impacting hydrocarbon production in shale reservoirs when the observed production exceeds expected rates (Gale et al., 2014).

Natural fractures are a fundamental aspect of the geological structure of numerous unconventional reservoirs. Therefore, to study their potential impact in DSS and LF-DAS results, I model strain and strain rate considering the interaction between natural and hydraulic fractures failing in shear and tensile modes, respectively.

Distribution of natural fractures in the field is an element with a high level of uncertainty. In reservoir simulation for instance, the traditional discrete fracture networks (DFN) is a probabilistic approach used to model such type of fractures. Since one of the purposes of this work is to investigate if strain results are affected by the modification of natural fractures geometric characteristics, I have designed natural fractures in which their configuration (e.g., orientation angle and length) can be controlled (not possible using DFN).

In this case a sensitivity analysis consisting of three scenarios (**Figure 3.12**) is performed by varying the orientation angle (strike in 3D mode) and length of natural fractures. The simulation accounts for 10 natural fractures per cluster, the orientation varies from ±20 to ±60°, and the length ranges from 13.3 to 25 ft.

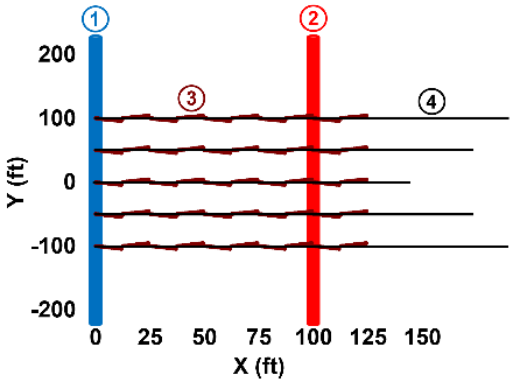

a. Scenario *a*: Orientation: ±20°, Length:13.3 ft

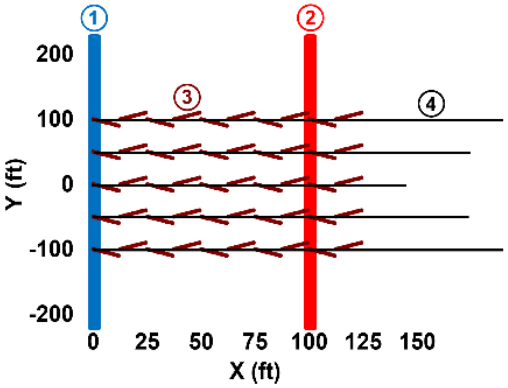

b. Scenario *b*: Orientation: ±40°, Length:16.3 ft

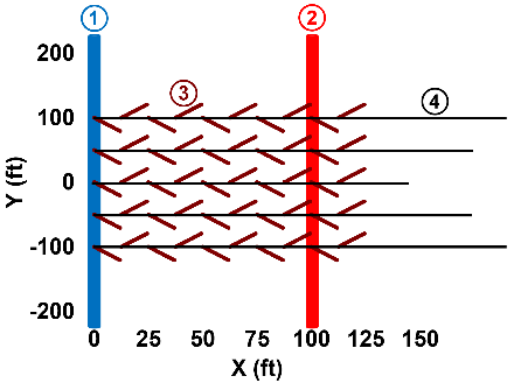

c. Scenario *c*: Orientation: ±60°, Length:25 ft

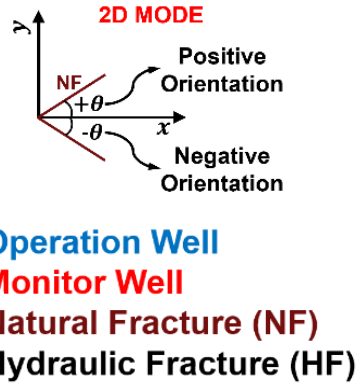

Figure 3.12–Map view of lateral section of horizontal wells varying NF orientation and length.

Figure 3.13 shows DSS and LF-DAS modeling results of scenarios *a*, *b* and *c*.

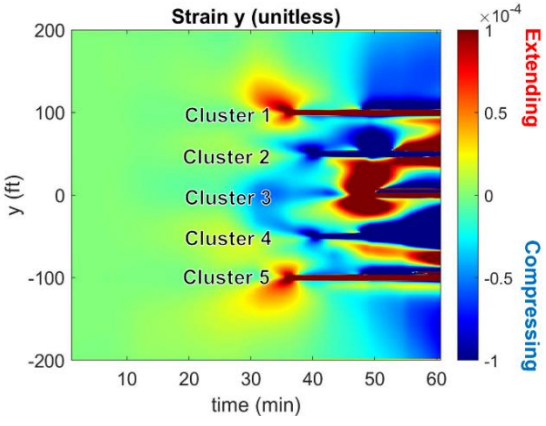

a. DSS → Scenario *a*

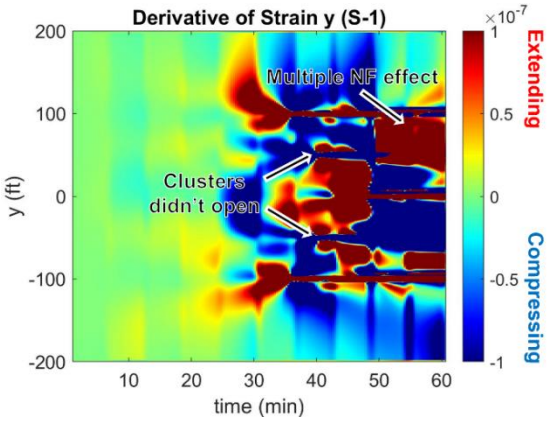

b. LF-DAS → Scenario *a*

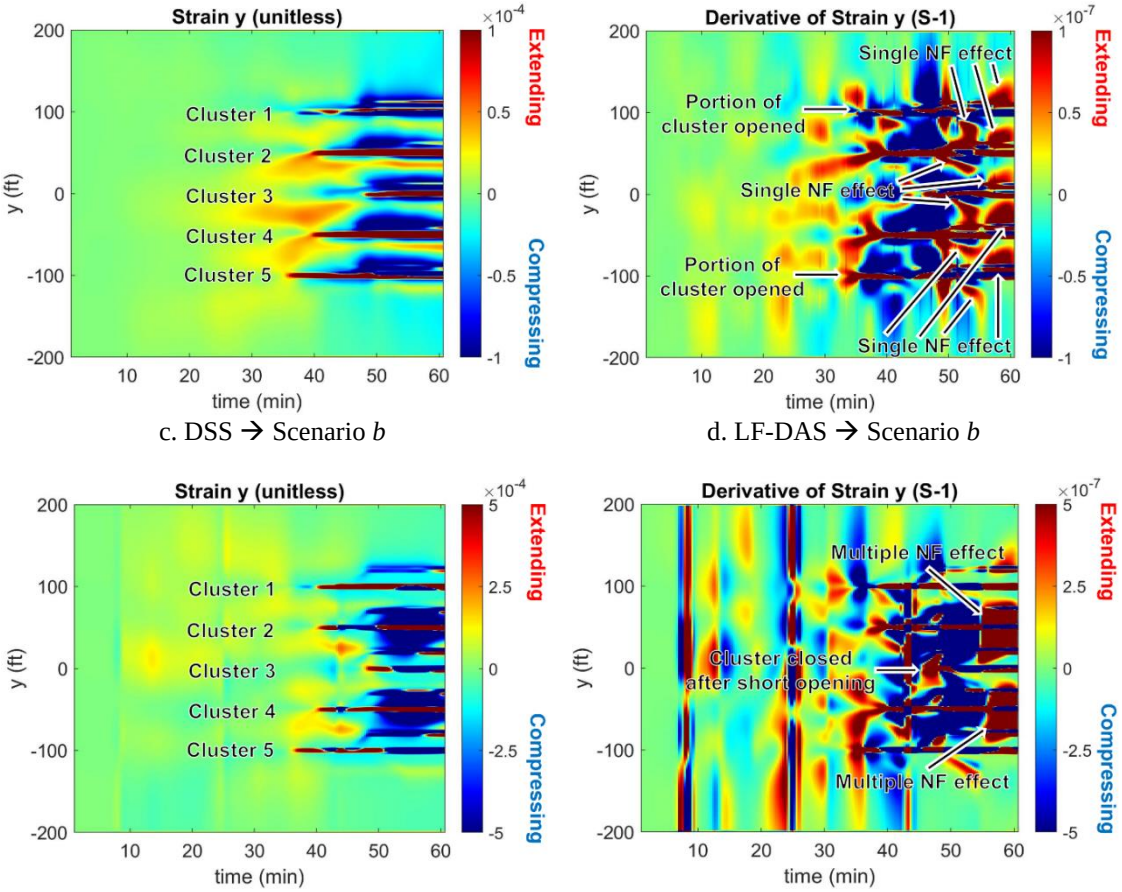

c. DSS → Scenario *b*

d. LF-DAS → Scenario *b*

e. DSS → Scenario *c*

f. LF-DAS → Scenario *c*

Figure 3.13–DSS and LF-DAS modeling results of sensitivity analysis varying NF orientation and length.

Evaluation of LF-DAS results in **Figure 3.13** reveals the following:

1. LF-DAS waterfall plots display details that are not observed in DSS waterfall plots.
2. Interaction between natural and hydraulic fractures, results in DSS/LF-DAS time histories plots entailing complexities not observed in the base case scenario (**Figure 3.9**). Moreover, it modifies stress shadow effect impacting the generation of throughgoing hydraulic fractures from different clusters.
3. Geometric details of natural fractures are not evident (lack of spatial resolution) if such planar discontinuities are located near in individual (i.e., scenario *a*) or adjacent clusters (i.e., scenario *c*).

3.2.1. Fiber Gauge Length Impact on Strain

In the previous numerical simulations, I have modeled strain fields generated during hydraulic fracturing treatments applying a small fiber gauge length (i.e., 1 m), attempting to obtain time histories catching detailed geometric features of fractures failing in shear and tensile modes. In this section, scenario *b* (**Figure 3.12b**) is modeled by considering 5 and 10 m gauge lengths to study the impact it may have on LF-DAS results (**Figure 3.14**).

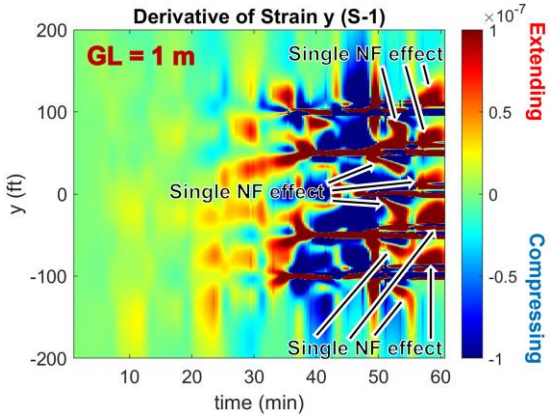

a. LF-DAS → 1 m fiber gauge length

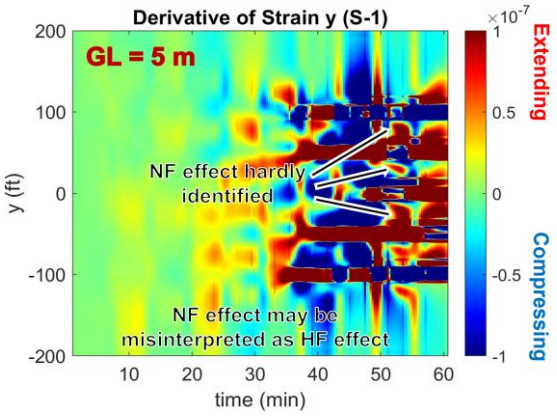

b. LF-DAS → 5 m fiber gauge length

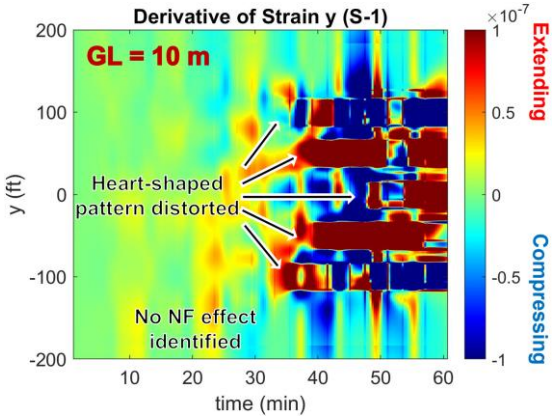

c. LF-DAS → 10 m fiber gauge length

Figure 3.14–(a, b, c) LF-DAS waterfall plots using 1 m, 5 m, and 10 m gauge lengths, respectively.

LF-DAS waterfall plots in **Figure 3.14a**, **Figure 3.14b**, and **Figure 3.14c** indicate that an increase in fiber gauge length has the potential to mask strain data richness. I can distinguish the effects associated with natural and hydraulic fractures using 1 m gauge length (**Figure 3.14a**). However, for the 10 m gauge length (**Figure 3.14c**), the heart-

shaped pattern of a fracture approaching the fiber is completely distorted, and to make things worse, no details linked to natural fractures are observed. Consequently, in this case, I am inclined to interpret the data purely in terms of opening fractures (data misinterpretation).

3.2.2. Natural Fracture Impact on Cluster Efficiency

The increment of oil and gas production in nanopore reservoirs is a topic that has a great dependence on cluster uniformity, one of the main challenges behind fracturing operations (Fragachan et al., 2019). In order to create hydraulic fractures that grow evenly and ultimately contact the maximum reservoir area, completion activities should be optimized using specialized tools such as simulation.

Natural fractures (NF) can be densely distributed in shale reservoirs, and they may have the potential to impact cluster efficiency (i.e., cluster uniformity). Romberg et al. (2021) published a Marcellus field case where clusters placed in naturally fractured rock were preferentially taking the treatment slurry and perforation clusters away from pre-existing fractures stopped propagating. Since it is a topic of great importance, in this work I perform simulations modeling strain type of data to investigate peculiarities associated with such case.

Simulations consist of a cross-well fiber deployment with monitor and operation wells distancing 100 ft, and 5 perforation clusters with only one located in naturally fractured area (i.e., central position) comprised by10 natural fractures oriented ±50° and ±65°.

Two scenarios are simulated varying natural fracture length and keeping constant its distribution and orientation (strike in 3D mode) as mentioned in the previous paragraph. Natural fractures in scenario *a* are 6.5 and 9.86 ft long while 19.4 and 29.6 ft in scenario *b*. **Figure 3.15a** and **Figure 3.15c** present adopted geometry of both scenarios (*a* and *b*).

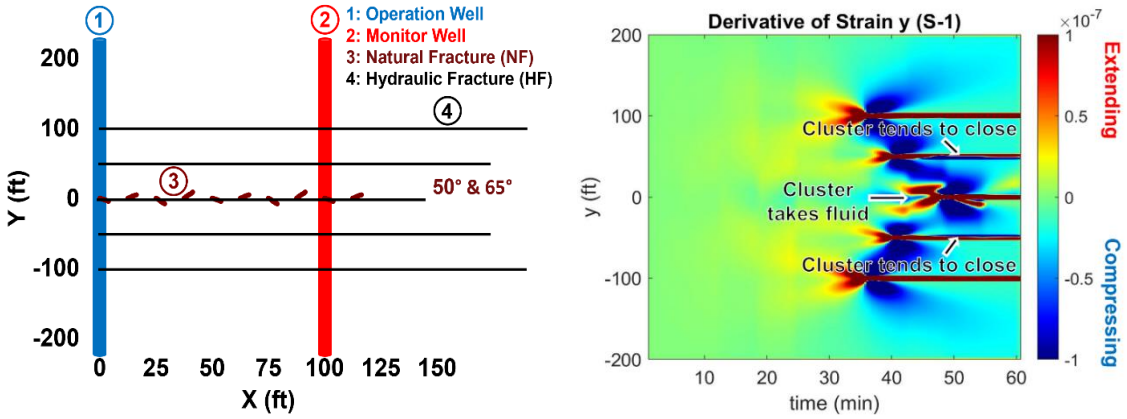

a. Length: 6.5 and 9.86 ft → Scenario *a*

b. LF-DAS → Scenario *a*

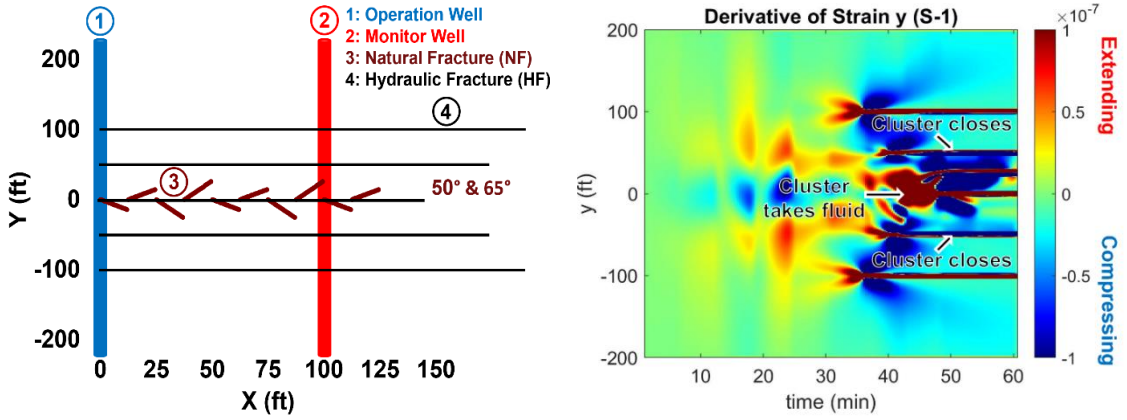

c. Length: 19.4 and 29.6 ft → Scenario *b*

d. LF-DAS → Scenario *b*

Figure 3.15–Map view of lateral section of horizontal wells varying NF length (a and c) and respective LF-DAS modeling results (b and d).

Simulation results in **Figure 3.15b** and **Figure 3.15d** comply with Marcellus field data and do not exhibit great complexity.

Evaluation of LF-DAS results in **Figure 3.15b** and **Figure 3.15d** reveals the following aspects:

1. Scenario *a*: Small portion of clusters immediately above and below the naturally fractured rock closes. Therefore, the impact promoted by short natural fractures on stress shadow is limited.

2. Scenario *b*: Increasing natural fracture length results in greater stress shadowing effect surrounding central cluster. Thus, clusters immediately

above and below naturally fractured formation close completely right after short opening.

The following interpretation is proposed for the phenomena shown in simulations:

1. Fluid leaks-off perforation cluster placed in NF region and moves towards pre-existing fractures promoting: (1) NF stress increase, (2) NF motion, and (3) stress shadow.
2. Stress shadow impacts clusters away from NF.
3. Clusters occupying region without NF need additional net pressure to keep propagating.
4. Required net pressure is not achieved, consequently clusters located in region with no NF will stop propagating.

Simulation of low-frequency DAS may be a valuable tool to assist engineers defining proper cluster spacing in naturally fractured formations in order to avoid low cluster efficiency and thus optimize completion design.

3.2.3. Characterization of Strain Fields When Pumping Stops

At the end of the fracturing treatment, when pumps are turned off, specialists have reported (Bourne et al., 2021) based on field datasets (e.g., microseismic and fiber-optics) that fractures might continue to grow. For the first time using fiber synthetic data, I characterize strain fields when pumping stops and thus demonstrate the physics of this question.

The simulation setup consists of a single hydraulic fracture and cross-well fiber deployment with operation and monitor wells distancing 300 ft. Fracturing lasts about 60 min and, when pumping stops, fiber monitors 30 min strain fields of 6 pressure drop gradients representing distinct fluid leak-off scenarios (**Figure 3.16**). I perform two studies to determine the pair extension-compression (i.e., polarity changes) in LF-DAS

time history plots when pumping is over: in study 1 (**Figure 3.17**) fracture propagation terminates and, in study 2 (**Figure 3.18**) it does not.

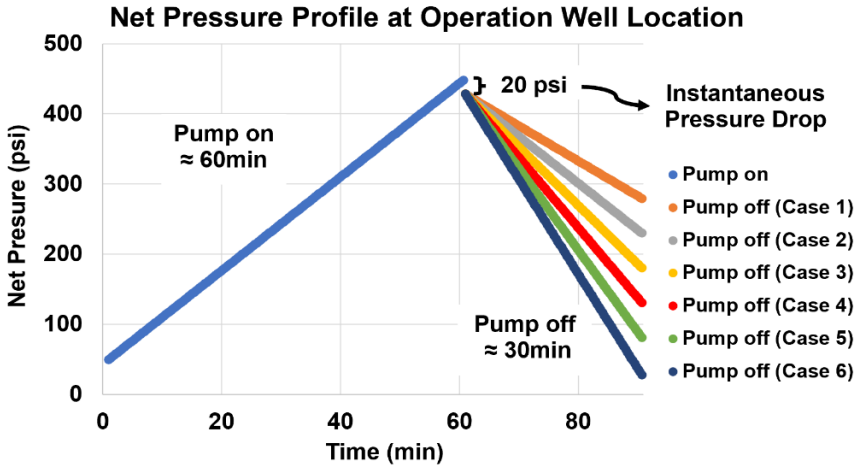

Figure 3.16–Net pressure profile at operation well location assumed in studies 1 and 2. Pressure: (1) increases linearly for 60 min when the pump is on; (2) Drops 20 psi immediately at the pump off instant; and (3) Lastly drops following a linear trend for 30 min. Six different pressure drop gradients are analyzed when pumping stops.

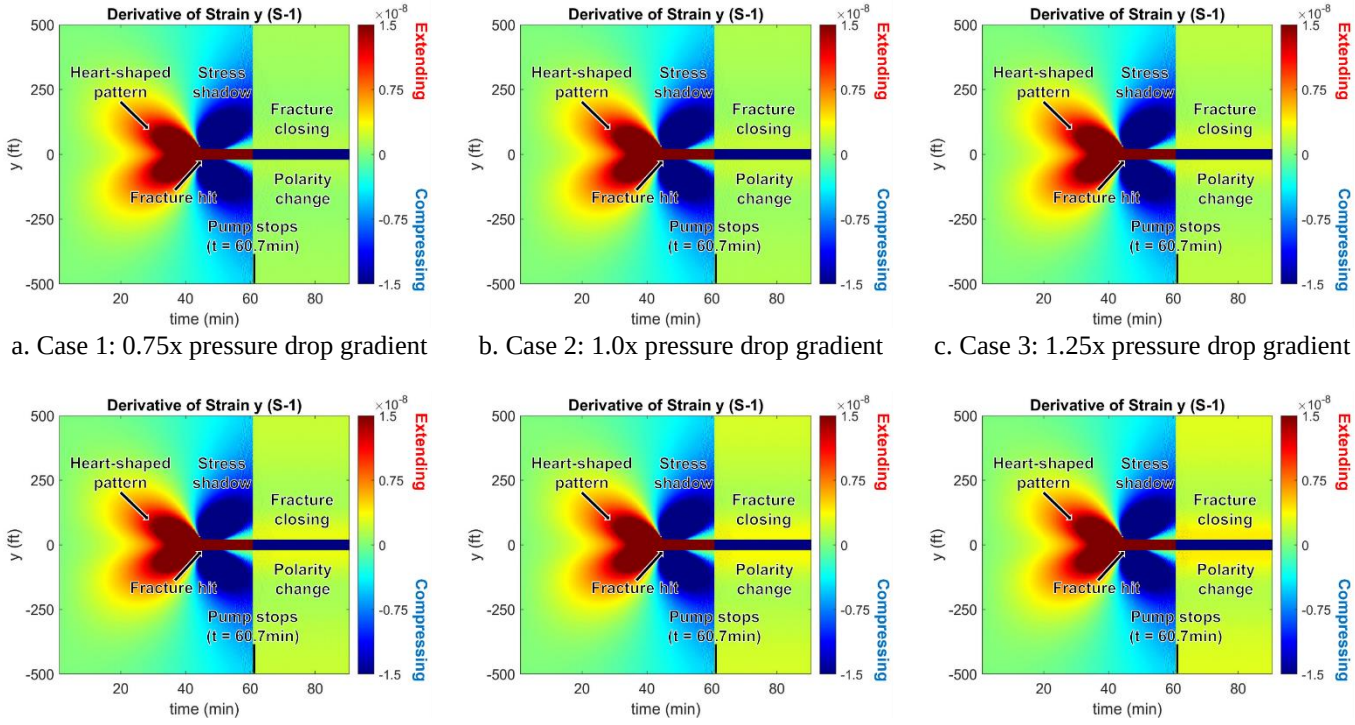

a. Case 1: 0.75x pressure drop gradient b. Case 2: 1.0x pressure drop gradient c. Case 3: 1.25x pressure drop gradient

d. Case 4: 1.5x pressure drop gradient e. Case 5: 1.75x pressure drop gradient f. Case 6: 2.02x pressure drop gradient

Figure 3.17–LF-DAS results of study 1 (fracture propagation terminates when pumping is finished) for all six pressure drop gradients.

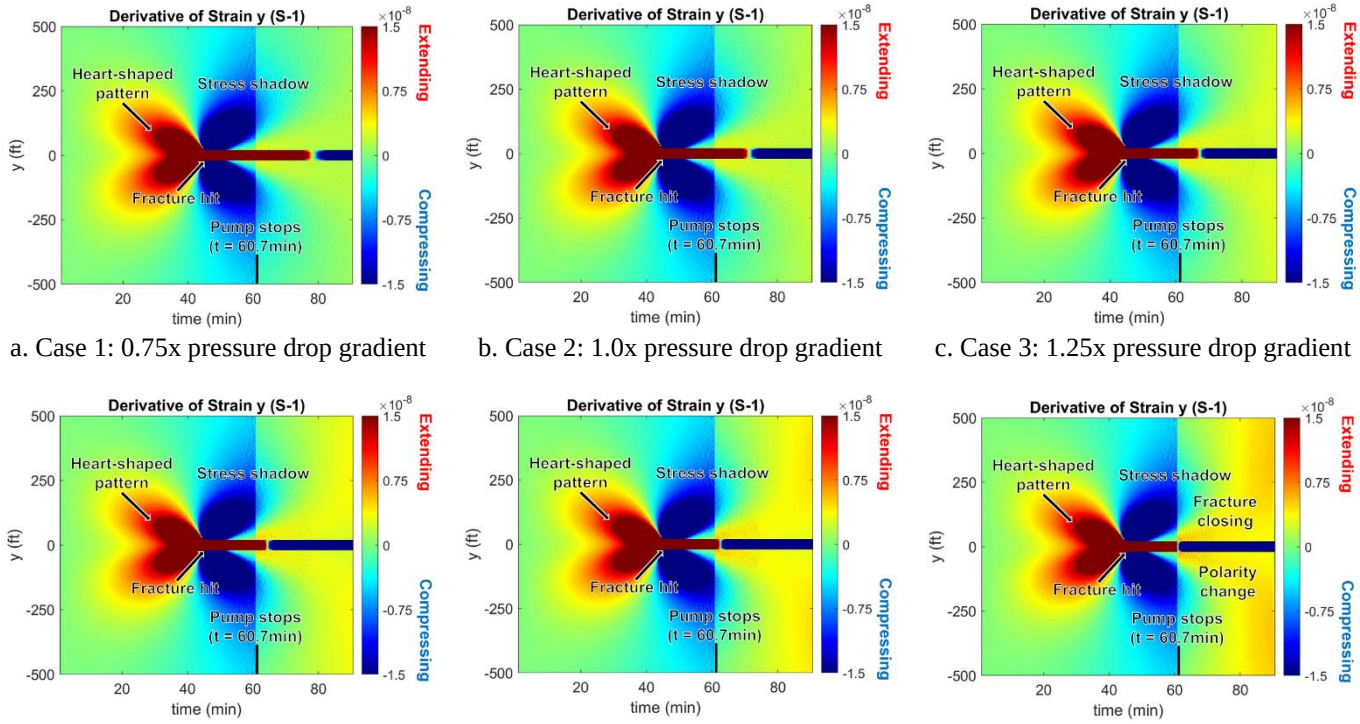

a. Case 1: 0.75x pressure drop gradient b. Case 2: 1.0x pressure drop gradient c. Case 3: 1.25x pressure drop gradient

d. Case 4: 1.5x pressure drop gradient e. Case 5: 1.75x pressure drop gradient f. Case 6: 2.02x pressure drop gradient

Figure 3.18–LF-DAS results of study 2 (fracture propagation doesn't terminate when pumping is finished) for all six pressure drop gradients.

Strain rate results of study 1 (**Figure 3.17**) indicate polarity changes immediately at the pump off instant for all fluid leak-off scenarios: (1) fracture corridor sign switches from extension (i.e., opening) to compression (i.e., closing) and (2) fracture neighboring sign shifts from compression to extension. On the other hand, the LF-DAS dataset of study 2 (**Figure 3.18**) reveals that the fracture may not close at the monitor well location when pumping stops. The smaller the pressure drop gradient, the later the fracture begins to close. Therefore, I infer that after the treatment phase, the hydraulic fracture continues propagating if no compression signature is identified in the fracture corridor present on the LF-DAS waterfall plot.

3.2.4. Identification of Fracture Hit Moment

The bottomhole pressure gauge (BHPG) is a surveillance tool installed at the monitor well with the response as a function of stress shadow (Haustveit et al., 2022). In addition to

fiber-optic strain response (i.e., DSS/LF-DAS), the model framework developed in this project can generate induced stresses associated with fracture propagation (i.e., stress shadow). In this section, it is observed that the second derivative of induced stress has the potential to identify the fracture hit moment, and I anticipate that the same principle may be applied in the field with BHPG data.

The simulation consists of three hydraulic fractures (HF) and cross-well fiber deployment with the operation and monitor wells distancing 300 ft. **Figure 3.19** shows the LF-DAS results (10 m fiber gauge length) of four different cluster spacing (i.e., 25, 50, 100, and 150 ft) evaluated in this work.

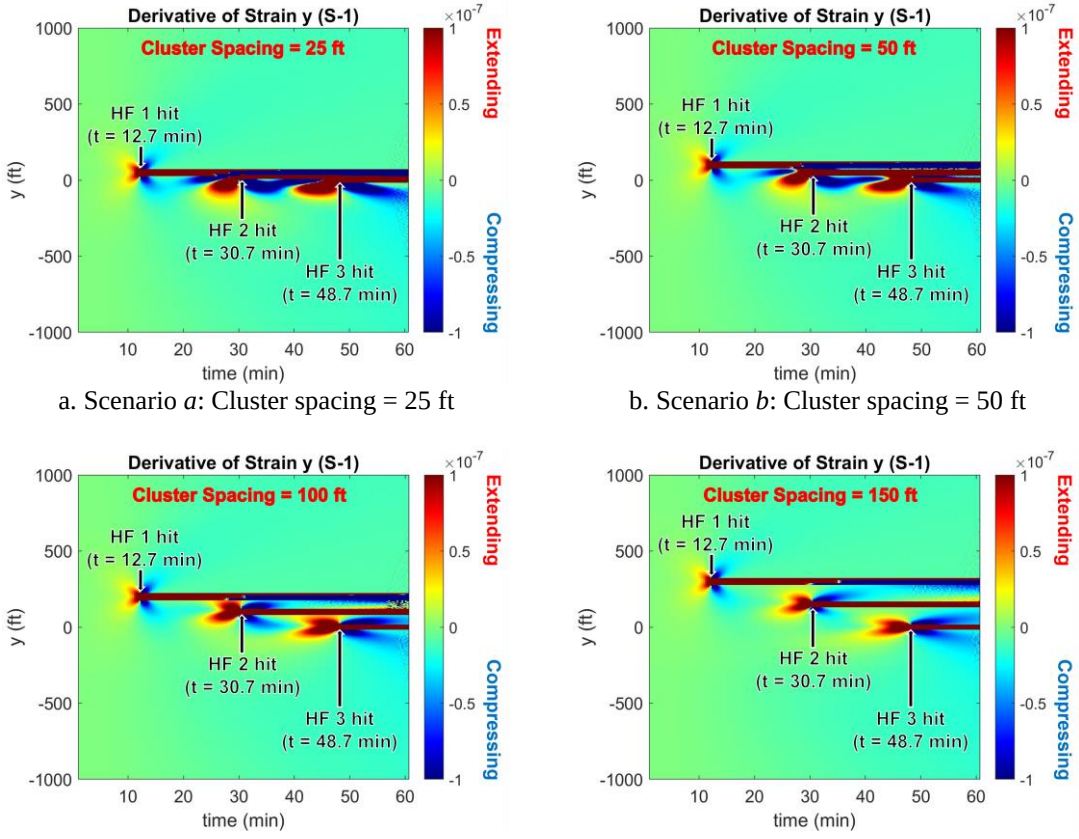

a. Scenario *a*: Cluster spacing = 25 ft

b. Scenario *b*: Cluster spacing = 50 ft

c. Scenario *c*: Cluster spacing = 100 ft

d. Scenario *d*: Cluster spacing = 150 ft

Figure 3.19–LF-DAS results of four cluster spacing scenarios (i.e., 25, 50, 100, and 150 ft) in this study, consisting of three hydraulic fractures.

LF-DAS dataset indicates that HF 1, 2, and 3 hit monitor well at 12. 7, 30.7, and 48.7 min, respectively.

Figure 3.20 shows the second derivative of stress acquired by a channel located at y = -75 ft (closer to HF 3), and I note that cluster spacing may impact hit moment identification using this method. Three spikes (i.e., hits) are observed using small cluster spacing (i.e., 25 and 50 ft), and just one (associated with HF 3) applying large spacing (i.e., 100 and 150 ft).

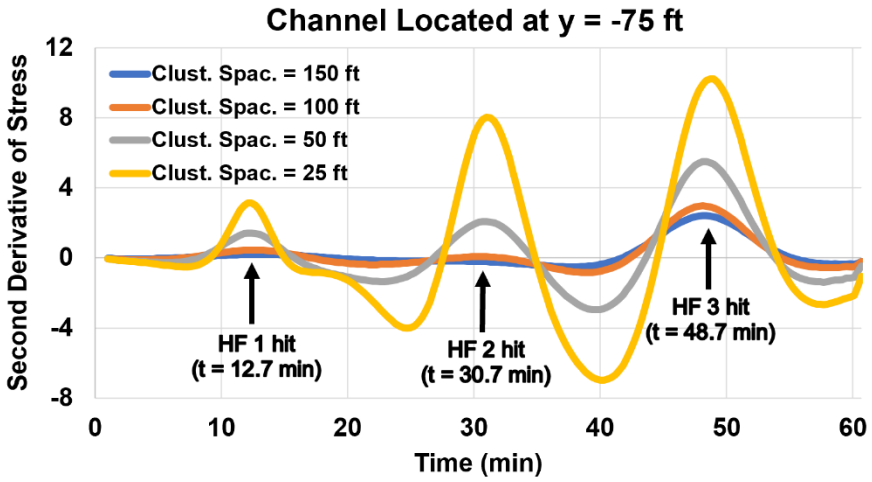

Figure 3.20–Plot of the second derivative of stress acquired by channel located at y = -75 ft.

Field data has a significant level of noise that is not observed in synthetic datasets. Therefore, large time intervals should be considered deriving field BHPG (i.e., smoothness process) in order to properly use this variable identifying the fracture hit instant.

3.2.5. Stress Shadow Transmissibility

In this section, I model a single hydraulic fracture considering a cross-well fiber deployment with the operation and monitor wells 700 ft apart (fracture propagation speed is 22.8 ft/min). **Figure 3.21** presents DSS and LF-DAS results using 10 m fiber gauge length.

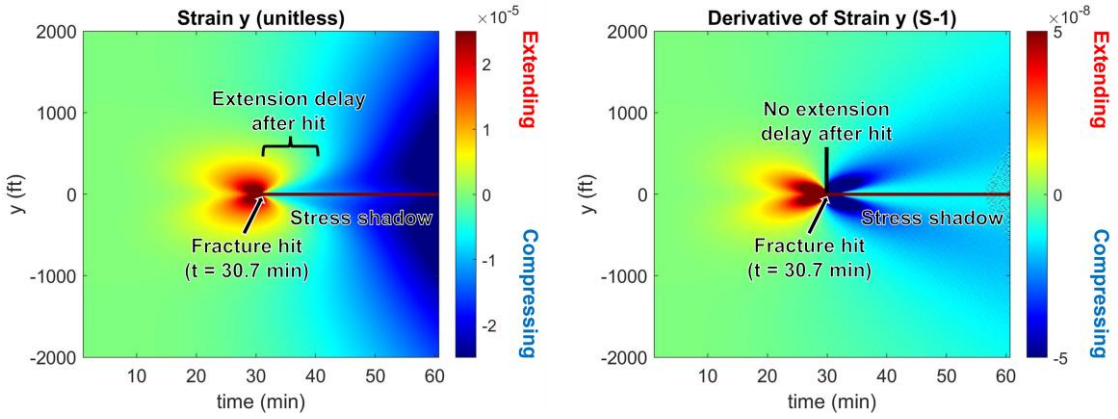

a. Distributed Strain Sensing (DSS)

b. Low-Frquency Distributed Acoustic Sensing (LF-DAS)

Figure 3.21–(a) DSS and (b) LF-DAS modeling results of a single hydraulic fracture. Following fracture hit at time = 30.7 min, DSS waterfall plot indicates that the extension sign surrounding opening fracture delays before switching to compression. This phenomenon is not observed in the LF-DAS plot, which presents an immediate polarity change above and below the fracture face.

In **Figure 3.22**, I plot stress of 10 time steps after the fracture hit (time = 30.7 min) against distance from the fracture corridor. Stress drops following a nearly exponential trend as the distance from fracture increases (i.e., stress transmissibility), and stress at the fracture face (distance = 0 ft) is an estimate of net pressure. A particular event occurs at early time steps following the hit instant (i.e., from time = 33.7 to 42.7 min): stress drops and rises near the fracture face. This anomaly is an effect of the heart-shaped pattern extension signature that is delayed before switching to compression after the fracture hit, and it appears only in the DSS waterfall plot (**Figure 3.21a**).

Many tightly spaced fractures have been observed by Raterman et al. (2018) and Fu et al. (2021) in the Eagle Ford and Midland Basin pilots (**Figure 3.23** and **Figure 3.24**), respectively. However, the physics governing this phenomenon is not clear yet. When the fracture approaches the fiber, extension energy represented by the heart-shaped pattern in fiber-optic strain datasets is generated. Following the fracture hit, absolute strain synthetic data in **Figure 3.21a** shows residue of this extension sign near the main hydraulic fracture, which is an indication that rock might be failing in this region. Thus, I suspect that fracture swarms can be created with the heart-shaped pattern residue energy.

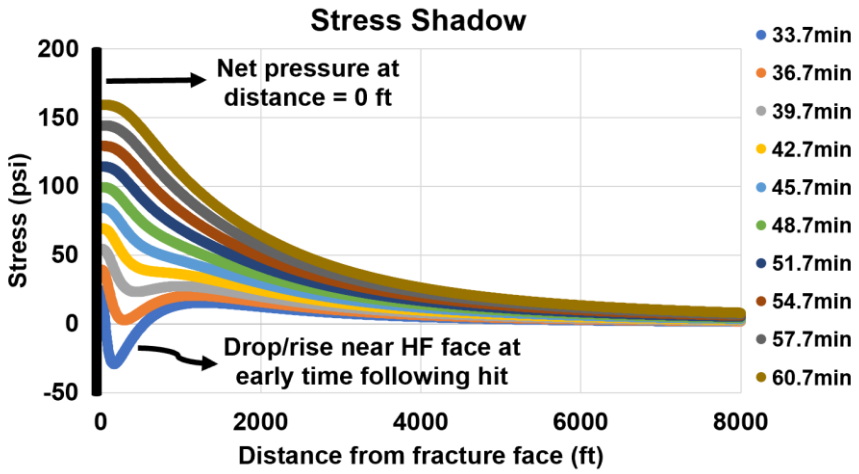

Figure 3.22– Stress of 10 time steps after fracture hit versus distance from fracture face (stress shadow transmissibility).

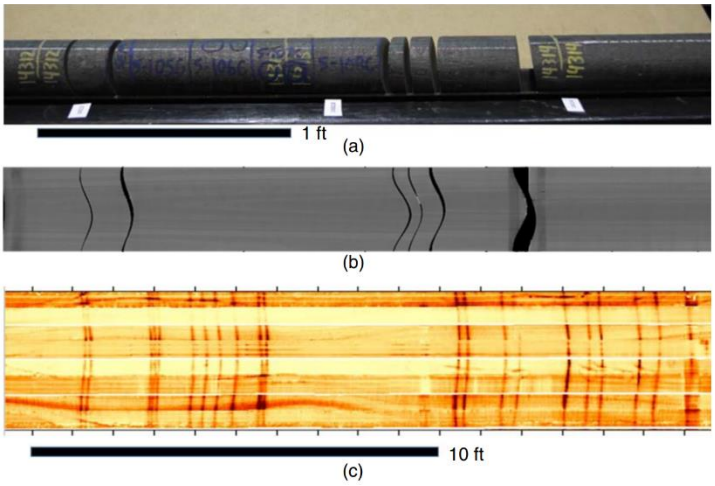

Figure 3.23–Fractures observed in the Eagle Ford pilot. (a) Dipping fractures in the core; (b) Computed Tomography (CT) scan image of the same section of core shown in a; (c) 18 ft of an image log taken from the same well showing several closely spaced fractures. Adapted from Raterman et al. (2018).

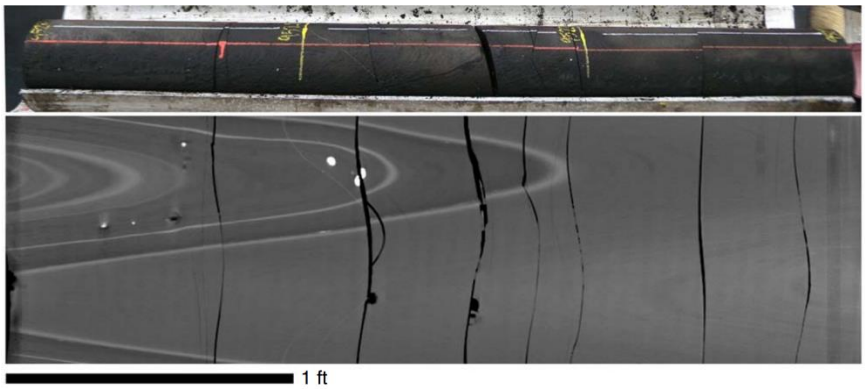

Figure 3.24–Fractures observed in Midland Basin pilot. Top: 3-ft long core-back sample containing eight parallel/subparallel fractures. Bottom: CT scan image of corresponding core sample. Adapted from Fu et al. (2021).

3.3. Deep Learning Algorithm and Fracture Width Estimation

In this project I work with two datasets representing scenarios consisting of fractures failing in tensile mode. Cases 1 and 2 are composed by one and three hydraulic fractures, respectively. In both cases the lateral section (1000 ft) of horizontal wells (i.e., operation and monitor) is placed along y axis, and 13 monitor wells are deployed in increments of 50 ft between X = 0 ft and X = 600 ft.

3.3.1. Case 1: Single Hydraulic Fracture

Fracture propagation spans approximately 2 hours in case 1, and the axial displacement waterfall plot for each monitor well is composed by 1,050,840 grid points (**Figure 3.25**). Thus, total dataset consisting of 13 monitor wells have 13,660,920 observations normally distributed (**Figure 3.26**).

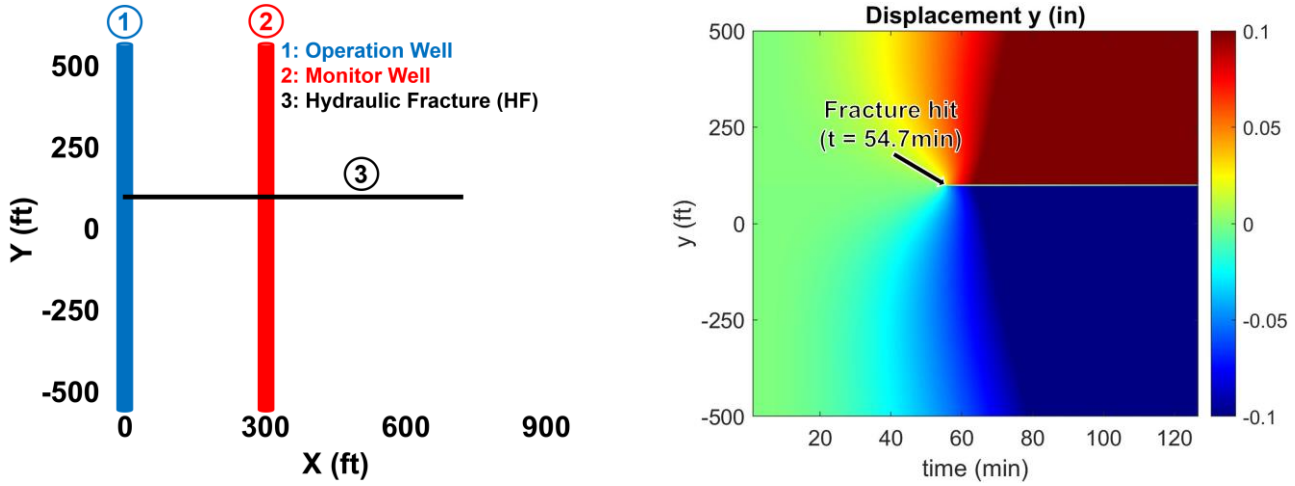

a. Map view of lateral section of horizontal wells distancing 300 ft.

b. True axial displacement generated with DDM code.

Figure 3.25–(a) Map view of scenario composed by single hydraulic fracture located at y = 100 ft where operation and monitor wells are distancing 300 ft, and (b) corresponding true axial displacement obtained with DDM code.

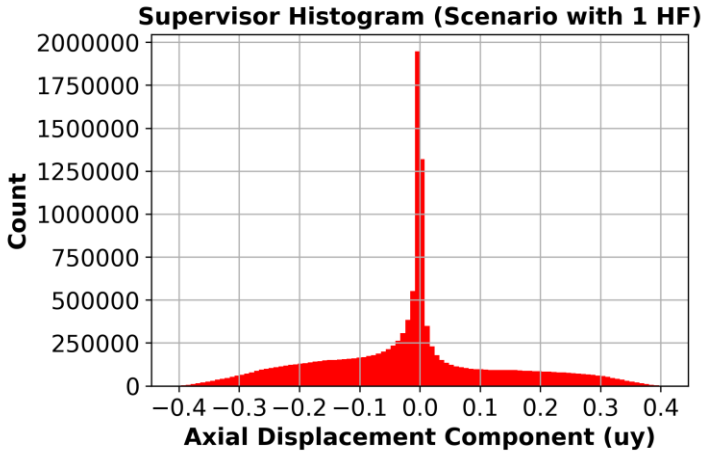

Figure 3.26–Histogram of axial displacement (machine learning algorithm supervisor variable) of scenario composed by single hydraulic fracture. The total number of observations is 13,660,920 (normal distribution), with magnitudes ranging between -0.4 and +0.4 in, and greatest concentration around 0.

During training stage of the DL model, 12,610,080 observations are used from 12 monitor wells (X = 0, 50, 100, 150, 200, 250, 350, 400, 450, 500, 550, 600 ft) in order to develop an algorithm able to estimate tangent displacement component (strain fields) for any spatio-temporal input (X, Y and time). For each epoch (total n° of epochs: 1000) I test the trained model predicting u_y of single monitor well (n° of observations: 1,050,840)

located at X = 300 ft. This phase is performed avoiding overfitting, and L2 loss continues pretty much steady after a significant drop at the beginning of process (i.e., before 200 epochs) (**Figure 3.27**). The magnitude of loss function might reduce even more if a variable learning rate is applied (i.e., learning rate scheduler).

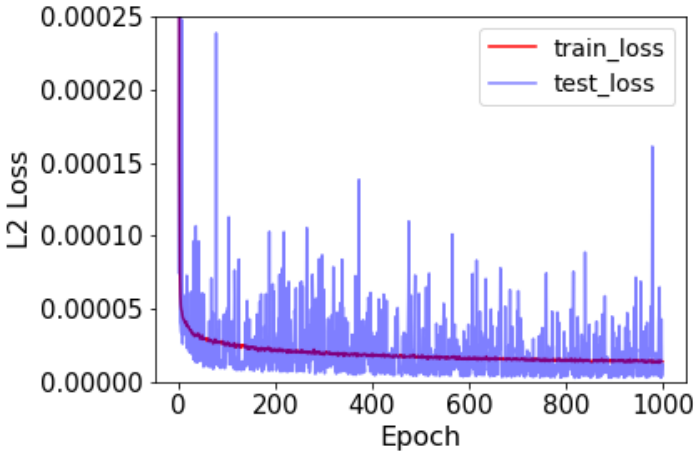

Figure 3.27–Plot of L2 loss against n° of epochs obtained during training stage of dataset representing scenario composed by single hydraulic fracture. There is pretty much no overfitting and greatest reduction in error function occurs at the phase onset.

Once the spatio-temporal machine learning scheme is developed (training stage is completed), official testing stage is performed predicting axial displacement along monitor well placed at X = 300 ft (**Figure 3.28a**). Comparing predicted and true u_y values (**Figure 3.28b**), I observe that the relative error is negligible in the entire waterfall plot area, except at initial time steps where fracture treatment starts at operation well and magnitude of axial displacement collected at monitor well is very small on the order of 10^{-6} or even lower. I suspect that such errors may be a consequence of the L2 loss function used training the DL model. Since I'm working with tiny outputs at initial times, squaring the difference between true and predicted values can result in negligible errors even when the magnitude of these elements is far from close, consequently some weights and biases of ANN may be barely updated during backpropagation phase and algorithm will tend to don't present an optimum performance in such regions.

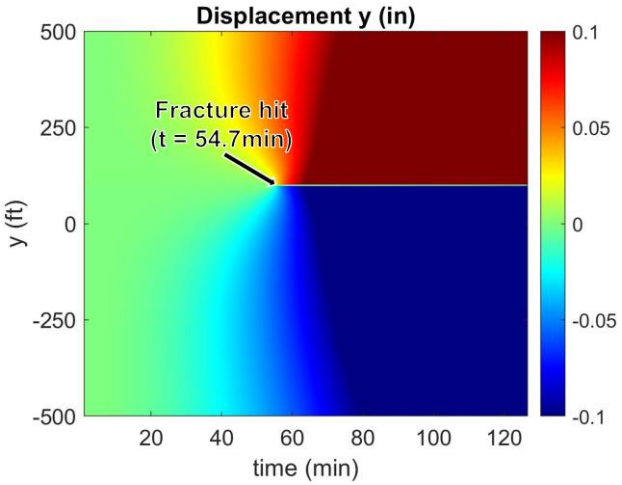

a. Predicted u_y at X = 300 ft.

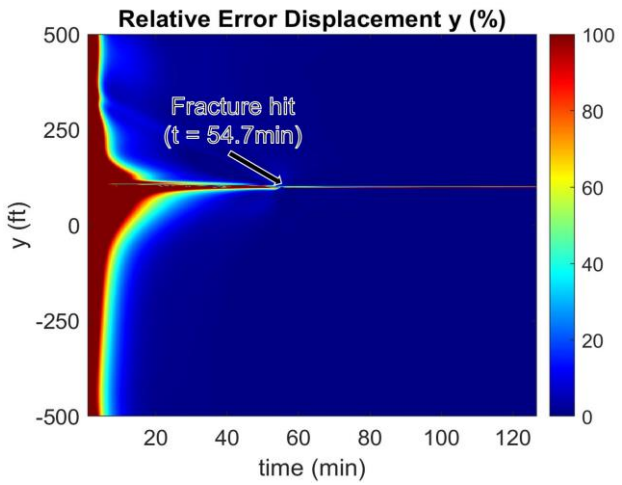

b. Relative error between predicted and true u_y values at X = 300 ft.

Figure 3.28–(a) Predicted u_y at monitor well location (X = 300 ft) using developed spatio-temporal machine learning scheme. (b) Relative error between predicted and true u_y at X = 300 ft. DL model has an overall consistent performance: (1) error is negligible in the entire waterfall plot region (except at early time steps); and (2) instant of fracture hit is correctly captured (t = 54.7 min).

Strain rate is calculated at X = 300 ft deriving predicted tangent displacement component sequentially in space and time (**Figure 3.29**). As expected, classic features associated with LF-DAS datasets are captured: (1) heart-shaped pattern from a fracture approaching the fiber; (2) fracture hit; and (3) stress shadow (i.e., compression zone adjacent to an opening fracture).

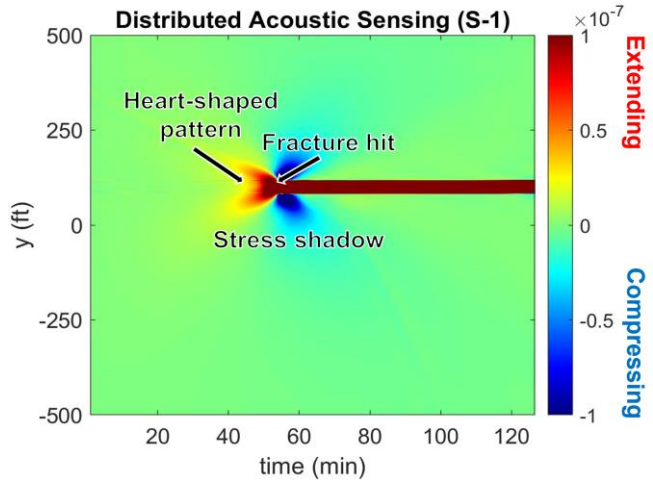

Figure 3.29–LF-DAS data calculated at X = 300 ft based on estimated u_y with developed spatio-temporal machine learning model (case 1). Classic features are observed: (1) hart-shaped pattern; (2) fracture hit; and (3) stress shadow.

Starting at the hit instant in monitor well placed at X = 300 ft (t = 54.7 min), I estimate fracture width along time measuring the discontinuity length exhibited in the plot of axial displacement predicted by developed DL model versus channel location ("discontinuity length" method). Predicted width present a rising trend (**Figure 3.30**), which is an expected tendency since net pressure used in DDM simulator generating synthetic data increases constantly in time. Relative error between predicted and true width acquired from DDM code drops substantially reaching values near 0% right after an initial 15% at fracture hit moment.

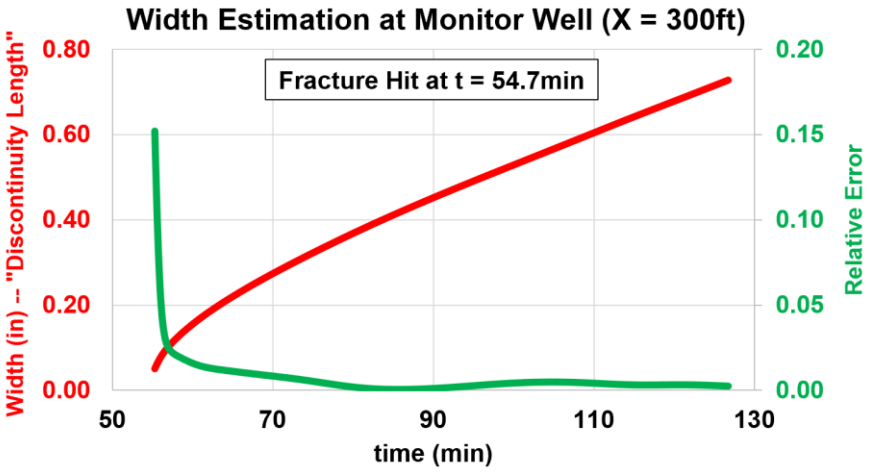

Figure 3.30–Results obtained following fracture hit (t = 54.7 min) at monitor well location (X = 300 ft). Red curve shows upward trend of predicted fracture width (estimated using proposed "discontinuity length" method), while green curve displays the relative error between predicted and true widths falling near 0% after an initial 15% at fracture hit instant.

I apply the developed spatio-temporal machine learning scheme predicting axial displacement in multiple locations from X = 300 to near 700 ft (includes extrapolation procedure since DL model is trained with data up to X = 600 ft). Acquired data is used to estimate fracture width along time in each position applying the "discontinuity length" method proposed in this work (**Figure 3.31**). For each time step an elliptic curve resembling the hydraulic fracture shape is formed. Finally, I calculate the error between predicted and true width generated with DDM code (**Figure 3.32**) and observe that its magnitude decreases toward 0% in each X point as time goes up (i.e., right after fracture hit). The model developed with synthetic data is an incentive for the deployment of multiple monitor wells in the field to enhance beyond the near wellbore region geometric characterization of created fracture systems.

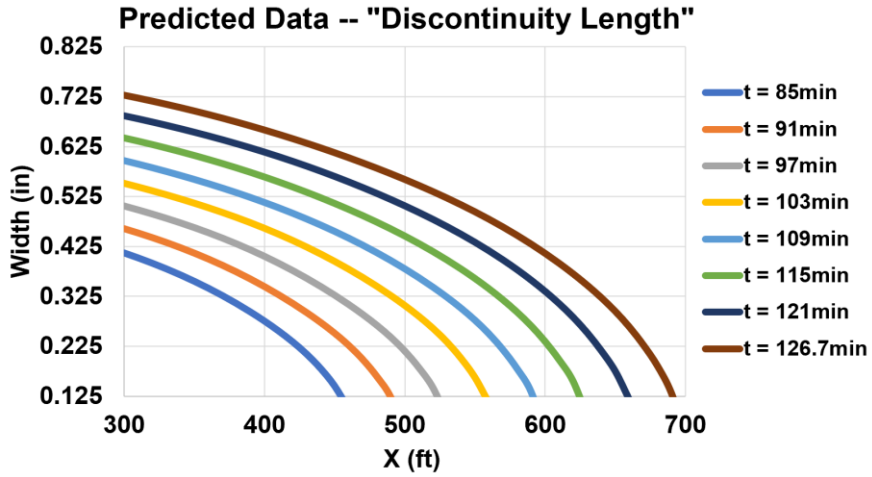

Figure 3.31–Plot of predicted fracture width (estimated using proposed "discontinuity length" method and data obtained from developed DL model) against position (X ranges from 300 to near 700 ft) for 8 consecutive time steps (t varies from 85 to 126.7 min). For all time steps, curves have an elliptic shape resembling fracture contour.

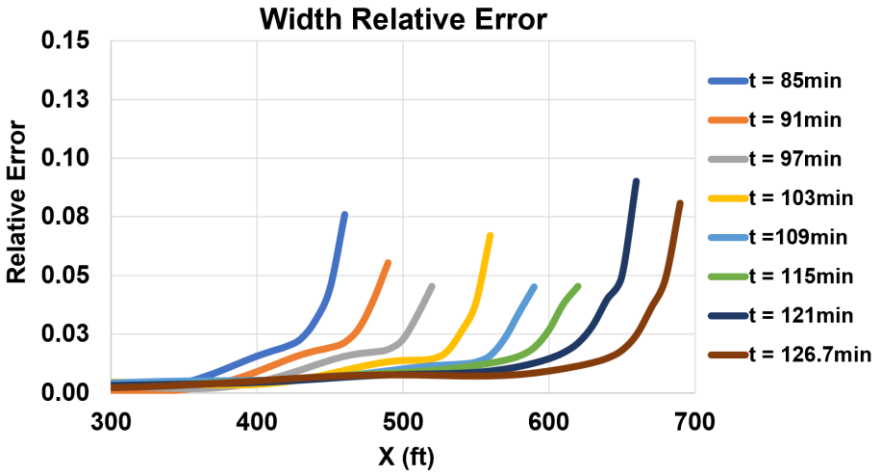

Figure 3.32–Plot of relative error between predicted width (estimated using proposed "discontinuity length" method and data obtained from developed DL model) and the true one (generated with DDM code) versus location (X ranges from 300 to near 700 ft) for 8 consecutive time steps (t varies from 85 to 126.7 min). Magnitude of error drops near 0% in each X location as time goes up (i.e., right after fracture hit).

3.3.2. Case 2: Multiple Hydraulic Fractures

Fracture propagation spans approximately 1 hour in case 2 (faster than case 1), and the axial displacement waterfall plot for each monitor well is composed by 500,400 grid points

(**Figure 3.33**). Thus, total dataset consisting of 13 monitor wells have 6,505,200 observations normally distributed (less than case 1) (**Figure 3.34**).

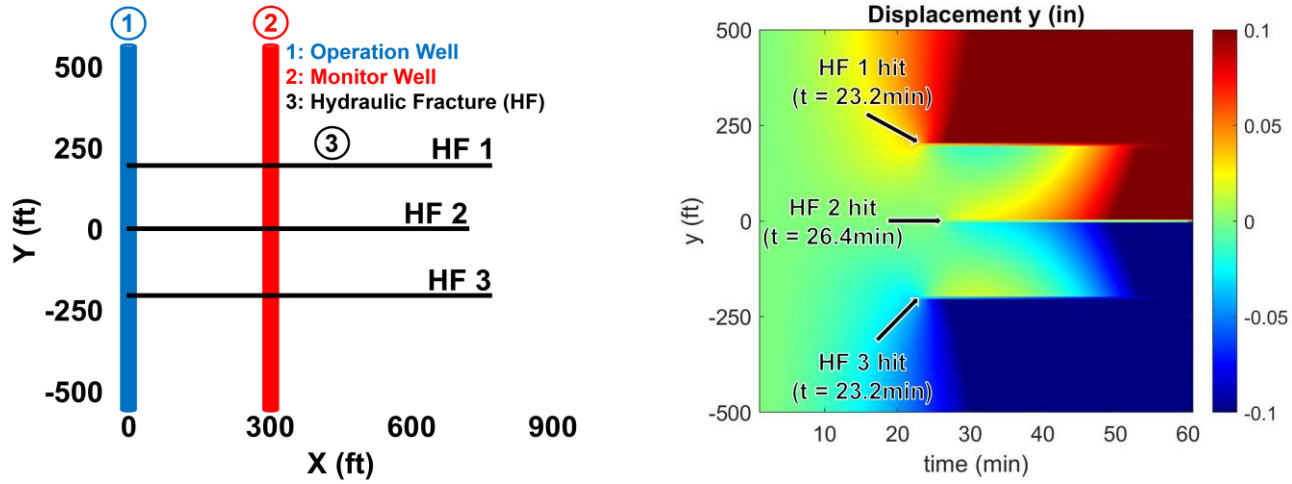

a. Map view of lateral section of horizontal wells distancing 300ft.

b. True axial displacement generated with DDM code.

Figure 3.33–(a) Map view of scenario composed by 3 hydraulic fractures located at y = -200, 0, +200 ft where operation and monitor wells are distancing 300 ft, and (b) corresponding true axial displacement obtained with DDM code.

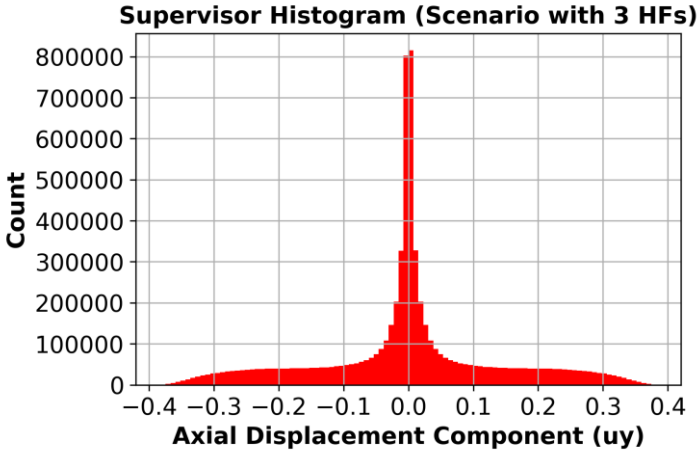

Figure 3.34–Histogram of axial displacement (machine learning algorithm supervisor variable) of scenario composed by 3 hydraulic fractures. The total number of observations is 6,505,200 (normal distribution), with magnitudes ranging between -0.4 and +0.4 in, and greatest concentration around 0.

During training stage of the DL model, 6,004,800 observations are used from 12 monitor wells (X = 0, 50, 100, 150, 200, 250, 350, 400, 450, 500, 550, 600 ft) in order to develop an algorithm able to estimate tangent displacement component (strain fields) for

any spatio-temporal input (X, Y and time). For each epoch (total n° of epochs: 1000) I test the trained model predicting u_y of single monitor well (n° of observations: 500,400) located at X = 300 ft. This phase is performed avoiding overfitting, and the loss function (i.e., L1 loss) drops continually throughout the process (**Figure 3.35**).

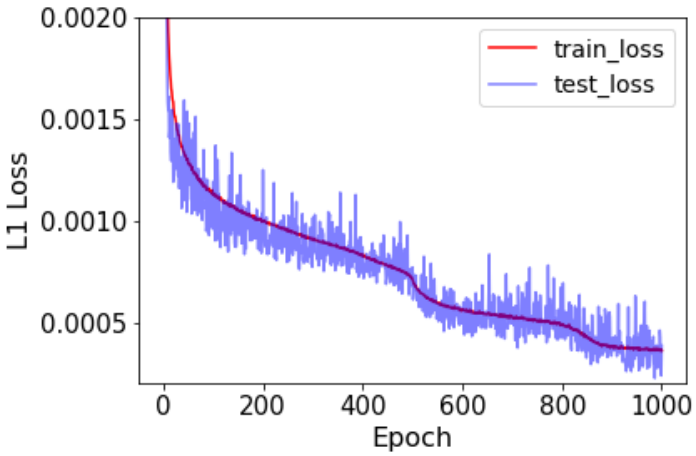

Figure 3.35–Plot of L1 loss against n° of epochs obtained during training stage of dataset representing scenario composed by 3 hydraulic fractures. There is pretty much no overfitting and error function drops consistently as n° of epochs increases.

Once the spatio-temporal machine learning scheme is developed (training stage is completed), official testing stage is performed predicting axial displacement along monitor well placed at X = 300 ft (**Figure 3.36a**). Comparing predicted and true u_y values (**Figure 3.36b**), I observe that the relative error is negligible in the entire waterfall plot area, except at initial time steps where fracture treatment starts at operation well and magnitude of axial displacement collected at monitor well is very small on the order of 10^{-6} or even lower.

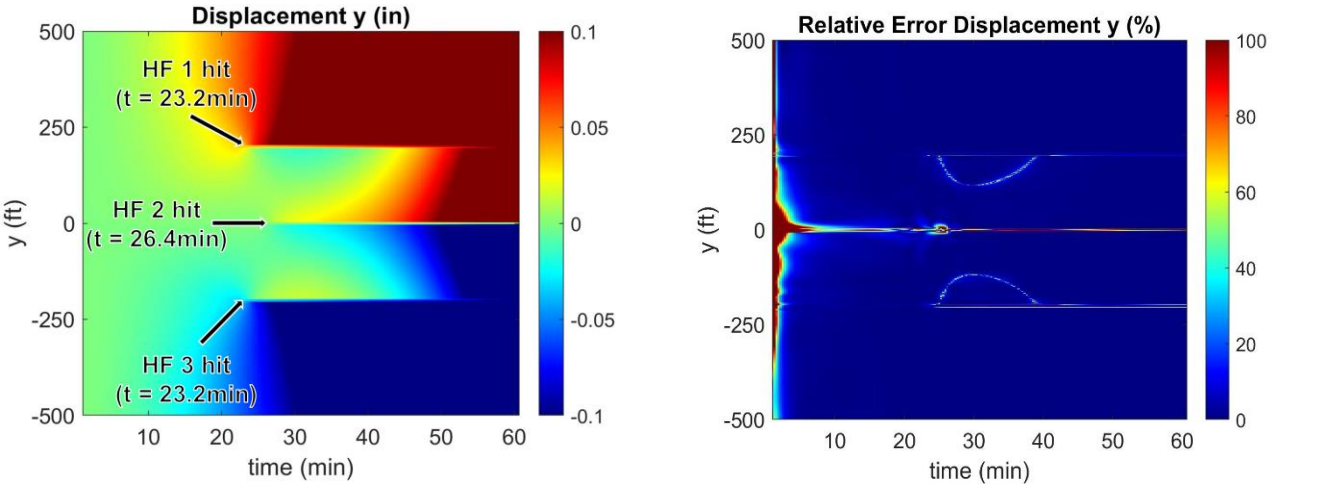

a. Predicted u_y at X = 300 ft.

b. Relative error between predicted and true u_y values at X = 300 ft.

Figure 3.36–(a) Predicted u_y at monitor well location (X = 300 ft) using developed spatio-temporal machine learning scheme. (b) Relative error between predicted and true u_y at X = 300 ft. DL model has an overall consistent performance: (1) error is negligible in the entire waterfall plot region (except at extremely early time steps); and (2) instant of fracture hit is correctly captured (HFs 1 and 3 at t = 23.2 min, and HF 2 at t = 26.4 min).

Comparing cases 1 and 2 waterfall plots of relative error specifically at early time steps, the latter presents much shorter region with data mismatch even though its DL model is trained with smaller dataset size representing a more complex fracturing scenario (i.e., 3 hydraulic fractures). I suspect that the major impact in case 2 results can be attributed to the application of L1 instead of L2 loss. Since I'm working with tiny outputs at initial times, errors estimated taking the absolute difference between true and predicted values will have a greater influence on loss function than the ones calculated by the squared difference method. Consequently, the updating process of ANN weights and biases (extremely dependent on loss function magnitude) during backpropagation phase will tend to be better executed leading the algorithm to present a superior performance.

Strain rate is calculated at X = 300 ft deriving predicted tangent displacement component sequentially in space and time (**Figure 3.37**). As expected, classic features associated with LF-DAS datasets are captured: (1) heart-shaped pattern from a fracture approaching the fiber; (2) fracture hit; and (3) stress shadow (i.e., compression zone adjacent to an opening fracture).

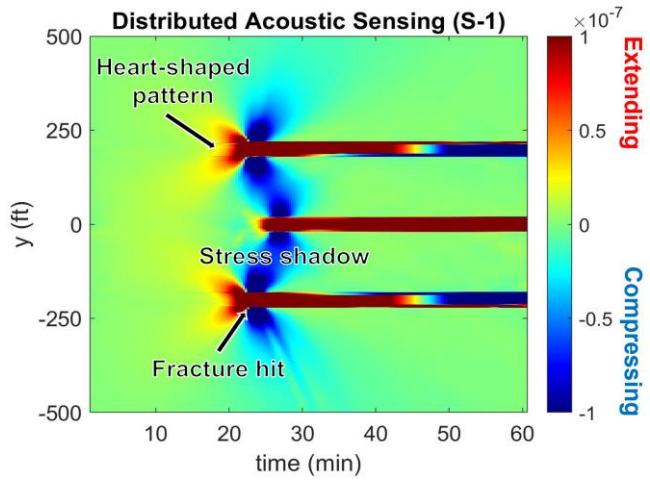

Figure 3.37–LF-DAS data calculated at X = 300 ft based on estimated u_y with developed spatio-temporal machine learning model (case 2). Classic features are observed: (1) hart-shaped pattern; (2) fracture hit; and (3) stress shadow.

3.4. Fracture Width Estimation Using Strain Dataset from the Stress Shadow Zone

Propagation of fracture systems is characterized in LF-DAS waterfall plots by the fracture corridor and the stress shadow region, which are represented by extension and compression signs, respectively (**Figure 3.38**). The evolution of stress shadow zone is the immediate effect of fracture opening (i.e., width generation), therefore in this work I develop a machine learning model using synthetic data to estimate fracture width at the monitor well location based on strain fields from the stress shadow region.

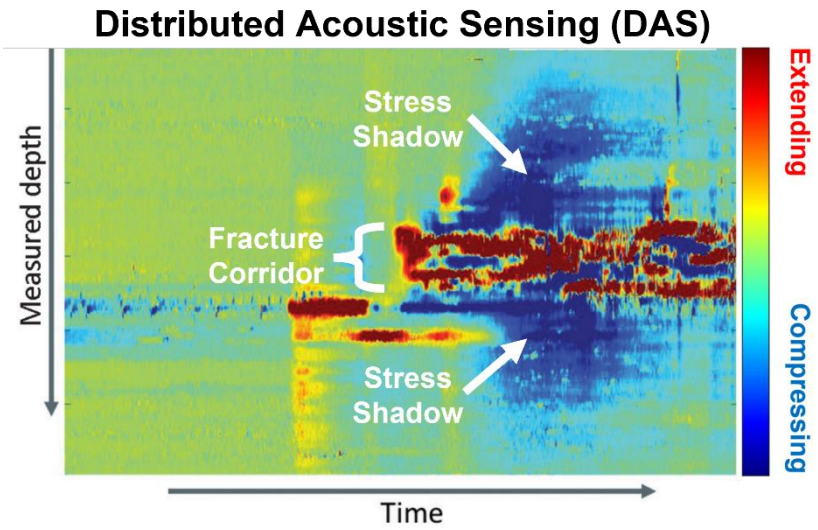

Figure 3.38–LF-DAS waterfall plot detailing the fracture corridor and stress shadow region. Adapted from Jin and Roy (2017).

The strain response obtained in the field by distributed fiber-optics sensing technology is represented by a complex mixture of extension and compression signs. This dataset does not provide any direct indication of fracture width magnitude. Therefore, the great benefit associated with the machine learning model created in this project is the potential fracture width inversion from field data.

Estimation of fracture width at the monitor well location from fiber-optic strain response in the stress shadow zone is a regression problem. Thus, I use four different supervised machine learning algorithms in this work: multilinear regression, support vector regression (SVR), artificial neural network (ANN) and random forest.

The model inputs are phase change (units of LF-DAS data collected in the field) of ten channels in the stress shadow zone, and the output is fracture width of 2400 observations (**Figure 3.39**).

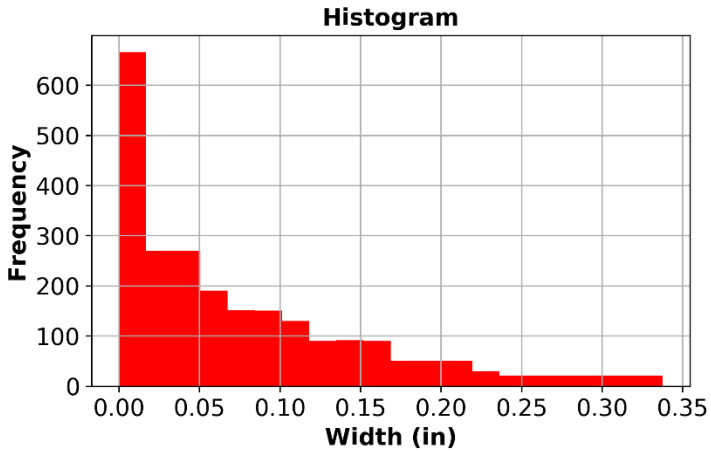

Figure 3.39–Histogram of fracture width (output variable) of machine learning model. The total number of observations is 2400 (log-normal distribution), with magnitudes ranging between 3.3 x 10^{-5} and 0.34 in.

In data wrangling stage I perform feature standardization ($\mu = 0$ and $std = 1$) before applying principal component analysis (PCA) to reduce the problem dimensionality. The first two principal components (PC1 and PC2) with explained variance of 99% are selected to be used as inputs in the machine learning algorithm. Therefore, applying PCA the number of features is reduced from ten to two.

In data splitting, 70% of data is used for training and 30% for testing.

The multilinear regression algorithm has no regularization (i.e., lasso, ridge and elastic net) technique. I use radial kernel with support vector regression. The artificial neural network model has three hidden layers, each with three neurons; LeakyRelu ($\alpha = 0.05$) is the nonlinear activation function applied in each hidden layer; I select the adaptive moment estimation (*Adam*) as optimizer; Batch size is 2 and number of epochs is 500. The nonlinear random forest algorithm has 500 trees, and a single feature is selected as split candidate. The pairplots comparing true and predicted width values applying the four algorithms with testing dataset are shown in **Figure 3.40**.

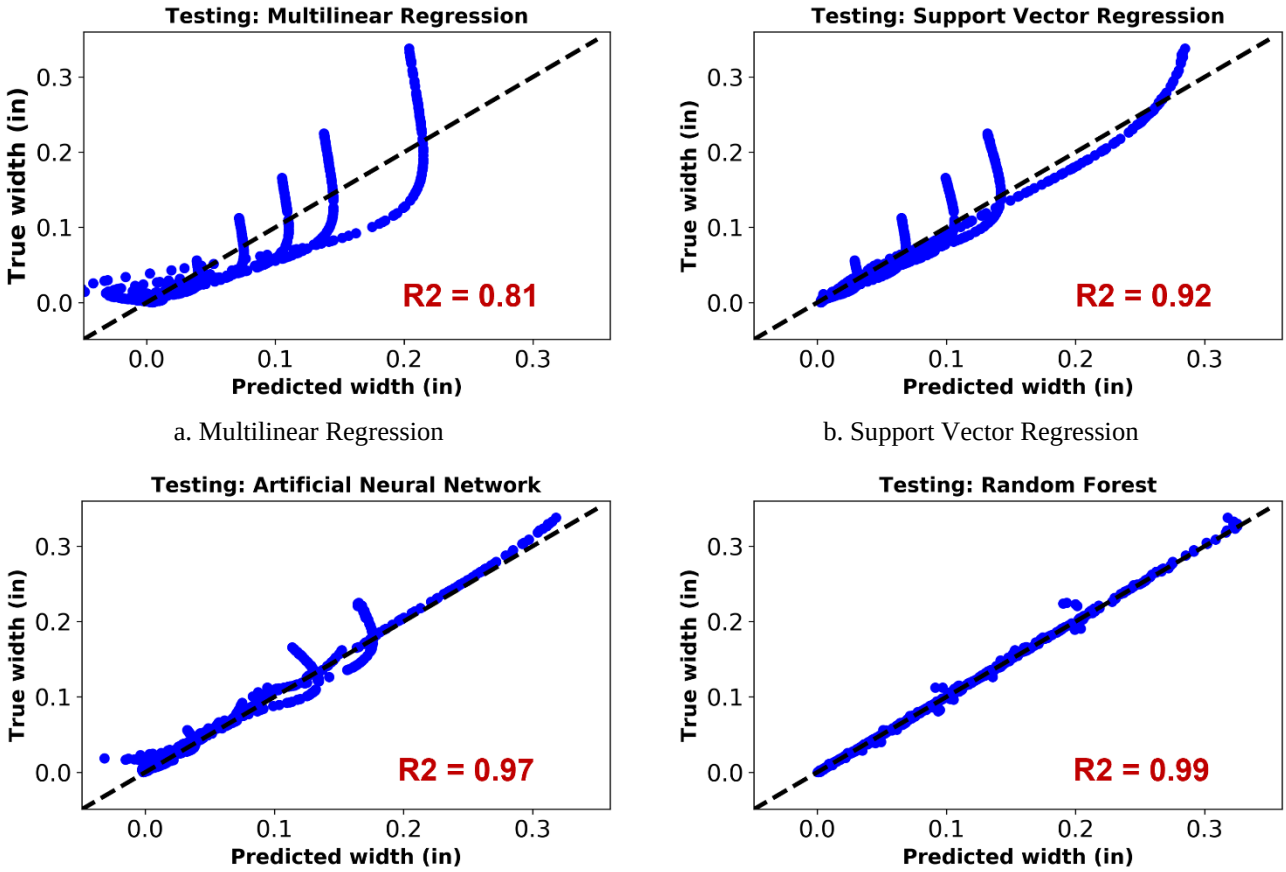

a. Multilinear Regression

b. Support Vector Regression

c. Artificial Neural Network

d. Random Forest

Figure 3.40–Pairplots comparing true and predicted width values applying multilinear regression, SVR, ANN and random forest algorithms with the testing dataset. The R2 metric indicates random forest as champion model.

The model performance in testing stage is evaluated using R2 metric. Results indicate that the linear model (i.e., multilinear regression) width predictions are not as good as expected, R2 is the smallest (0.81). The application of machine learning algorithms incorporating nonlinearities (i.e., SVR with radial kernel, ANN and random forest) leads R2 values to increase up to 0.99 with random forest (champion model). This is an indication that width estimation using strain fields from the stress shadow zone is a nonlinear problem. **Table 3.8** details the R2 and mean squared error (MSE) of each machine learning algorithm.

Table 3.8–Performance results of multilinear regression, SVR, ANN and random forest algorithms with testing dataset.

Machine Leaning Algorithm	R2	MSE
Multilinear Regression	0.81	1.1×10^{-3}
Support Vector Regression	0.92	4.7×10^{-4}
Artificial Neural Network	0.97	1.6×10^{-4}
Random Forest	0.99	9.5×10^{-6}

Results obtained with the random forest model are promising, which makes this algorithm a great candidate for field applications (physics-based machine learning framework) estimating fracture width in an approximate real-time fashion. This fact is paramount to production optimization since fracture treatment parameters may be modified during the treatment based on fracture geometry estimates.

4. CONCLUSIONS

Acoustic fiber-optics is an emerging surveillance technology in hydraulic fracturing treatments with acceptance expanding rapidly. This fact can be attributed to strain data versatility and wealth of detail, which have the potential to improve completion design and optimize production of unconventional reservoirs. However, field data carries complexities that puzzle engineers and geoscientists and limit them from fully exploring the richness of DSS/LF-DAS. In this work, I show that simulations applying forward modeling can provide a substantial perspective to specialists interpreting strain datasets.

Below I highlight the main observations of this work:

1. The analytical solution confirms important known trends. Single hydraulic fracture failing in tensile mode propagates faster in the following cases: (1) high Young's modulus; (2) high injection rate; and (3) low fluid viscosity.
2. The analytical solution indicates that strain datasets are sensitive to parameters associated with hydraulic fracturing treatments, and consequently, field data may be used inferring rock/fluid properties.
3. The incorporation of shear failure in numerical simulation points out the significant impact natural fractures may have on DSS/LF-DAS datasets, which is often interpreted solely in terms of opening fractures.
4. A large fiber gauge length can mask strain data richness, and I recommend the application of small values in field operations if the primary purpose is to investigate in detail signal arrivals at monitor well.
5. Natural fractures influence stress shadowing effect and consequently the generation of throughgoing hydraulic fractures from different clusters (i.e., cluster efficiency).
6. No sign of fracture closing on LF-DAS time history plots (i.e., corridor compression) when pumping is over indicates that the fracture system continues to propagate.

7. The second derivative of stress (BHPG response) can help us identify the fracture hit moment.
8. Stress shadow transmissibility follows a nearly exponential trend. The model framework may be used to determine the approximate cluster spacing that creates evenly growing fractures contacting the maximum reservoir area.
9. The heart-shaped pattern residue energy near the main hydraulic fracture after the hit (observed in DSS data), may be the mechanism linked to the generation of fracture swarms present in the Eagle Ford and Midland Basin pilots.
10. The deep learning model demonstrates value of multiple monitor wells in the field, improving fracture geometry characterization by estimating widths in multiple locations as a function of time.
11. Strain dataset from the stress shadow region is an important source of information associated with throughgoing hydraulic fractures. In this work, I show that it can be used with the support of a machine learning model to estimate fracture width (random forest algorithm provides the best results).

4.1. Recommendations for Future Work

To address important aspects of fiber-optics surveillance technology in hydraulic fracturing operations that are out of the scope of this project, I recommend the following future studies:

1. Extend the numerical solution to 3D space to model strain fields considering the monitor well in vertical/slanted orientations, and the horizontal operation/monitor well pair in different layers to determine the minimum principal stress impact on strain results.
2. Develop a numerical solution accounting for proppant transport modeling to determine how it may impact strain fields generated during fracturing operations, and if fiber-optics strain response has the potential to be used to estimate the effective conductivity of fracture systems.

3. Use field data in the testing stage of the machine learning model developed to estimate fracture width based on strain fields from the stress shadow zone. In addition, define a methodology to determine the confidence interval of fracture width values obtained from field data.

REFERENCES

Alanis, A., Daniel, N. A., and Franco, C. L. 2019. *Artificial Neural Networks for Engineering Applications,* first edition. Saint Louis, MO: Elsevier.

Al-Muntasheri, G. A., Liang, F., and Hull, K. L. 2017. Nanoparticle-Enhanced Hydraulic-Fracturing Fluids: A Review. *SPE Production & Operations* **32** (02): 186-195. https://doi.org/10.2118/185161-PA.

Bahi, M. and Batouch, M. 2018. Deep Learning for Ligand-Based Virtual Screening in Drug Discovery. Paper presented at the 3rd International Conference on Pattern Analysis and Intelligent Systems (PAIS), Tebessa, Algeria, 24-25 October. https://doi.org/10.1109/PAIS.2018.8598488.

Bishop, C. M. 2006. *Pattern Recognition and Machine Learning*, first edition. New York: Springer.

Bourne, S., Hindriks, K., Savitski, A. A., Ugueto, G. A., and Magdalena, W. 2021. Inference of Induced Fracture Geometries Using Fiber-Optic Distributed Strain Sensing in Hydraulic Fracture Test Site 2. Paper presented at the SPE/AAPG/SEG Unconventional Resources Technology Conference, Houston, Texas, USA, 26-28 July. URTEC-2021-5472-MS. https://doi.org/10.15530/urtec-2021-5472.

Brankovic, M., Gildin, E., Gibson, R. L., and Everett, M. E. 2021. A Machine Learning-Based Seismic Data Compression and Interpretation Using a Novel Shifted-Matrix. *Applied Sciences* **11** (11): 4874. https://doi.org/10.3390/app11114874.

Cipolla, C., Wolters, J., McKimmy, M., Miranda, C., Hari-Roy, S., Kechemir, A., and Gupta, N. 2022a. Observation Lateral Project: Direct Measurement of Far-Field Drainage in the Bakken. *SPE Production & Operations* 1-15. SPE-209164-PA. https://doi.org/10.2118/209164-PA.

Cipolla, C., McKimmy, M., Hari-Roy, S., Wolters, J., Haffener, J., Haustveit, K., and Almasoodi, M. 2022b. Evaluating Stimulation Effectiveness with Permanent Optical Fiber and Sealed Wellbore Pressure Monitoring: Bakken Shale Case Study. *SPE Drilling & Completion* 1-9. SPE-209129-PA. https://doi.org/10.2118/209129-PA.

Crouch, S. L. 1976. Solution of plane elasticity problems by the displacement discontinuity method. I. Infinity body solution. *International Journal for Numerical Methods in Engineering* **10** (2): 301-343. https://doi.org/10.1002/nme.1620100206.

Crouch, S. L. and Starfield, A. M. 1983. *Boundary element methods in solid mechanics*, first edition. London: George Allen & Unwin.

Curtis, J. B. 2002. Fractured Shale-Gas Systems. *AAPG Bulletin* **86** (11): 1921–1938. https://doi.org/10.1306/61EEDDBE-173E-11D7-8645000102C1865D.

Dalamarinis, P., Mueller, P., Logan, D., Glascock, J., and Broll, S. 2020. Real-Time Hydraulic Fracture Optimization Based on the Integration of Fracture Diagnostics and Reservoir Geomechanics. Paper presented at the SPE/AAPG/SEG Unconventional Resources Technology Conference, Virtual, 20-22 July. URTEC-2020-2786-MS. https://doi.org/10.15530/urtec-2020-2786.

Daley, T., Miller, D., Dodds, K., Cook, P., and Freifeld, B. 2016. Field testing of modular borehole monitoring with simultaneous distributed acoustic sensing and geophone vertical seismic profiles at Citronelle, Alabama. *Geophysical Prospecting* **64** (5): 1318-1334. https://doi.org/10.1111/1365-2478.12324.

Dickenson, P., Brants-Menard, S., Telsey, M., Stanbridge, A., Wilson, C., Akin, J., Roman, N., Anifowoshe, O., Yates, M. E., Carney, B. J., Costello, I., Hewitt, J., and Warner, R. 2016. Real-Time Interactive Remote Display of DTS and DAS Data for Well Treatment Optimization. Paper presented at the SPE Intelligent Energy International Conference and Exhibition, Aberdeen, Scotland, UK, 6-8 September. SPE-181065-MS. https://doi.org/10.2118/181065-MS.

Economides, M. J. and Nolte, K. G. 1989. *Reservoir Stimulation*, second edition. Englewood Cliffs, New Jersey: Prentice Hall.

Elliott, B., Zheng, S., Russel, R., Sharma, M., Haustveit, K., and Haffner, J. 2022. Integration of Sealed Wellbore Pressure Monitoring Responses with Wellbore Strain and Deformation Measurements for Fracture Diagnostics. Paper presented at the SPE Hydraulic Fracturing Technology Conference and Exhibition, The Woodlands, Texas, USA, 1-3 February. SPE-209120-MS. https://doi.org/10.2118/209120-MS.

Febus Optics. 2019. Distributed Fiber Optic Sensing for Geophysics: What are we really measuring? https://www.febus-optics.com/en/ (accessed March 2020).

Filev, M., Soldatov, V., Novikov, I., Xu, J., Ovchinnikov, K., Belova, A., and Drobot, A. 2021. Technology for Determining the Inflow from Near and Far Zones of Fractures During Hydraulic Fracturing by Chemical Tracers in a Production Well. Paper presented at the International Petroleum Technology Conference, Virtual, 23 March - 1 April. IPTC-21357-MS. https://doi.org/10.2523/IPTC-21357-MS.

Fragachan, F., Omer, M., and Huang, J. 2019. Uniform Fracture Growth from Horizontal Wells with Multistage Plug-and-Perf: An Application of Engineered Solid Particulate Diverters. Paper presented at the Abu Dhabi International Petroleum Exhibition & Conference, Abu Dhabi, UAE, 11-14 November. SPE-197970-MS. https://doi.org/10.2118/197970-MS.

Fu, W., Morris, J. P., Fu, P., Huang, J., Sherman, C. S., Settgast, R. R., and Ryerson, F. J. 2021. Developing Upscaling Approach for Swarming Hydraulic Fractures Observed at Hydraulic Fracturing Test Site through Multiscale Simulations. *SPE Journal* **26** (5): 2670-2684. SPE-199689-PA. https://doi.org/10.2118/199689-PA.

Gale, J. F. W. and Holder, J. 2010. Natural fractures in some US shales and their importance for gas production. *Geological Society, London, Petroleum Geology Conference series* **7** (1): 1131-1140. https://doi.org/10.1144/0071131.

Gale, J. F. W., Laubach, S. E., Olson, J. E., Eichhubl, P., and Fall, A. 2014. Natural fractures in shale: A review and new observations. *AAPG Bulletin* **98** (11): 2165–2216. https://doi.org/10.1306/08121413151.

Gamboa, E. S. 2014. *Natural Fracture Characterization by Source Mechanism Estimation and Semi-Stochastic Generation of Discrete Fracture Networks Using Microseismic and Core Data*. Master's Thesis, Texas A&M University, College Station, Texas (December 2014).

Géron, A. 2019. *Hands-on machine learning with Scikit-Learn, Keras and TensorFlow: concepts, tools, and techniques to build intelligent systems*, second edition. Sebastopol, CA: O'Reilly.

Gurjao, K. G. R., Gildin, E., Gibson, R., and Everett, M. 2021. Modeling of Distributed Strain Sensing (DSS) and Distributed Acoustic Sensing (DAS) Incorporating Hydraulic and Natural Fractures Interaction. Paper presented at the SPE/AAPG/SEG Unconventional Resources Technology Conference, Houston, Texas, USA, 26-28 July. URTEC-2021-5414-MS. https://doi.org/10.15530/urtec-2021-5414.

Gurjao, K. G. R., Gildin, E., Gibson, R., and Everett, M. 2022a. Estimation of Far-Field Fiber Optics Distributed Acoustic Sensing (DAS) Response Using Spatio-Temporal Machine Learning Schemes and Improvement of Hydraulic Fracture Geometric Characterization. Paper presented at the SPE Hydraulic Fracturing Technology Conference and Exhibition, The Woodlands, Texas, USA, 1-3 February. SPE-209119-MS. https://doi.org/10.2118/209119-MS.

Gurjao, K. G. R., Gildin, E., Gibson, R., and Everett, M. 2022b. Investigation of Strain Fields Generated by Hydraulic Fracturing with Analytical and Numerical Modeling of Fiber Optic Response. *SPE Reservoir Evaluation & Engineering* (in press; published online 11 February 2022). SPE-206049-PA. https://doi.org/10.2118/206049-PA.

Gutierrez, G., Sanchez, A., Rios, A., and Argüello, L. 2010. Microseismic Hydraulic Fracture Monitoring to Determine the Fracture Geometry in Coyotes Field, Chicontepec. Paper presented at the SPE Latin American and Caribbean Petroleum Engineering Conference, Lima, Peru, 1-3 December. SPE-139155-MS. https://doi.org/10.2118/139155-MS.

Hartog, A. H. 2017. *An introduction to distributed optical fibre sensors*. Boca Raton, FL: CRC press.

Hastie, T., Tibshirani, R., and Friedman, J. 2009. *The Elements of Statistical Learning: Data Mining, Inference, and Prediction*, second edition. New York: Springer.

Haustveit, K., Elliott, B., and Roberts, J. 2022. Empirical Meets Analytical-Novel Case Study Quantifies Fracture Stress Shadowing and Net Pressure Using Bottom Hole Pressure and Optical Fiber. Paper presented at the SPE Hydraulic Fracturing Technology Conference and Exhibition, The Woodlands, Texas, USA, 1-3 February. SPE-209128-MS. https://doi.org/10.2118/209128-MS.

Haustveit, K., Elliott, B., Haffener, J., Ketter, C., O'Brien, J., Almasoodi, M., Moos, S., Klaassen, T., Dahlgren, K., Ingle, T., Roberts, J., Gerding, E., Borell, J., Sharma, S., and Deeg, W. 2020. Monitoring the Pulse of a Well Through Sealed Wellbore Pressure Monitoring, a Breakthrough Diagnostic With a Multi-Basin Case Study. Paper presented at the SPE Hydraulic Fracturing Technology Conference and Exhibition, The Woodlands, Texas, USA, 4-6 February. SPE-199731-MS. https://doi.org/10.2118/199731-MS.

Hickey, M. S., Trevino, S., and Everett, M. E. 2017. Monitoring Hydraulic Fracturing Fluid Movement using Ground-Based Electromagnetics, with Applications to the Anadarko Basin and the Delaware Basin / NW Shelf. Paper presented at the SPE/AAPG/SEG Unconventional Resources Technology Conference, Austin, Texas,

USA, 24-26 July. URTEC-2690022-MS. https://doi.org/10.15530/URTEC-2017-2690022.

Holley, E. H. and Kalia, N. 2015. Fiber-optic Monitoring: Stimulation Results from Unconventional Reservoirs. Paper presented at the SPE/AAPG/SEG Unconventional Resources Technology Conference, San Antonio, Texas, USA, 20-22 July. URTEC-2151906-MS. https://doi.org/10.15530/URTEC-2015-2151906.

Huang, K., Hussain, A., Wang, Q., and Zhang, R. 2019. *Deep Learning: Fundamentals, Theory and Applications*, first edition. Cham: Springer Nature Switzerland AG.

Huckabee, P., Ledet, C., Ugueto, G., Tolle, J., and Mondal, S. 2021. Practical Design Considerations for Stage Length, Perforation Clusters and Limited Entry Pressure Intensities. Paper presented at the SPE Hydraulic Fracturing Technology Conference and Exhibition, Virtual, 4-6 May. SPE-204185-MS. https://doi.org/10.2118/204185-MS.

Hull, R. A., Meek, R., Bello, H. 2017. Case History of DAS Fiber-Based Microseismic and Strain Data, Monitoring Horizontal Hydraulic Stimulations Using Various Tools to Highlight Physical Deformation Processes (Part A). Paper presented at the SPE/AAPG/SEG Unconventional Resources Technology Conference, Austin, Texas, USA, 24-26 July. URTEC-2695282-MS. https://doi.org/10.15530/URTEC-2017-2695282.

Ichikawa, M., Uchida, S., Katou, M., Kurosawa, I., Tamura, K., Kato, K., Ito, Y., de Groot, M., Hara, S. 2020. Case Study of Hydraulic Fracture Monitoring Using Multiwell Integrated Analysis Based on Low-Frequency DAS Data. *The Leading Edge* **39** (11): 794-800. https://doi.org/10.1190/tle39110794.1.

Jamaloei, B. Y. 2021. A review of plug-and-perforate, ball-and-seat, and single-entry pinpoint fracturing performance in the unconventional montney reservoir. *Journal of*

Petroleum Exploration and Production **11** (3): 1155-1183. https://doi.org/10.1007/s13202-021-01085-6.

James, G., Witten, D., Hastie, T., and Tibshirani, R. 2021. *An Introduction to Statistical Learning: with Applications in R*, second edition. New York: Springer.

Jin, G. and Roy, B. 2017. Hydraulic-fracture geometry characterization using low-frequency DAS signal. *The Leading Edge* **36** (12): 975-980. https://doi.org/10.1190/tle36120975.1.

Jin, G., Ugueto, G., Wojtaszek, M., Guzik, A., Jurick, D., and Kishida, K. 2021. Novel Near-Wellbore Fracture Diagnosis for Unconventional Wells Using High-Resolution Distributed Strain Sensing during Production. *SPE Journal* **26** (5): 3255–3264. SPE-205394-PA. https://doi.org/10.2118/205394-PA.

Johannessen, K., Drakeley, B., and Farhadiroushan, M. 2012. Distributed Acoustic Sensing - A New Way of Listening to Your Well/Reservoir. Paper presented at the SPE Intelligent Energy International, Utrecht, The Netherlands, 27-29 March. SPE-149602-MS. https://doi.org/10.2118/149602-MS.

Karrenbach, M., Kahn, D., Cole, S., Ridge, A., Boone, K., Rich, J., Silver, K., and Langton, D. 2017. Hydraulic-fracturing-induced strain and microseismic using in situ distributed fiber-optic sensing. *The Leading Edge* **36** (10): 837-844. https://doi.org/10.1190/tle36100837.1.

Kechavarzi, C., Pelecanos, L., Nicholas, D. B., and Soga, K. 2019. Distributed fibre optic sensing for monitoring reinforced concrete piles. *Geotechnical Engineering Journal of the SEAGS & AGSSEA* **50** (2): 43-51.

Koelman, J. M. V. A., Lopez, J. L., and Potters, J. H. H. M. 2011. Fiber Optic Technology for Reservoir Surveillance. Paper presented at the International Petroleum Technology

Conference, Bangkok, Thailand, 15-17 November. IPTC-14629-MS. https://doi.org/10.2523/IPTC-14629-MS.

Krizhevsky, A., Sutskever, I., and Hinton, G. E. 2017. ImageNet Classification with Deep Convolutional Neural Networks. *Communications of the ACM* **60** (6): 84-90. https://doi.org/10.1145/3065386.

Li, X., Zhang, J., Grubert, M., Laing, C., Chavarria, A., Cole, S., and Oukaci, Y. 2020. Distributed Acoustic and Temperature Sensing Applications for Hydraulic Fracture Diagnostics. Paper presented at the SPE Hydraulic Fracturing Technology Conference and Exhibition, The Woodlands, Texas, USA, 4-6 February. SPE-199759-MS. https://doi.org/10.2118/199759-MS.

Liang, F., Sayed, M., Al-Muntasheri, G., and Chang, F. F. 2015. Overview of Existing Proppant Technologies and Challenges. Paper presented at the SPE Middle East Oil & Gas Show and Conference, Manama, Bahrain, 8-11 March. SPE-172763-MS. https://doi.org/SPE-172763-MS.

Lindsey, N. J. and Martin, E. R. 2021. Fiber-Optic Seismology. *Annual Review of Earth and Planetary Sciences* **49** (1): 309 – 336. https://www.annualreviews.org/doi/10.1146/annurev-earth-072420-065213.

Lindsey, N. J., Rademacher, H., and Ajo-Franklin, J. B. 2020. On the broadband instrument response of fiber-optic DAS arrays. *Journal of Geophysical Research: Solid Earth* **125** (2), e2019JB018145. https://doi.org/10.1029/2019JB018145.

Liu, Y., Wu, K., Jin, G., Moridis, G. J., Kerr, E., Scofield, R., and Johnson, A. 2020. Strain and Strain-Rate Responses Measured by LF-DAS and Corresponding Features for Fracture-Hit Detection during Multiple-Fracture Propagation in Unconventional Reservoirs. Paper presented at the SPE/AAPG/SEG Unconventional Resources Technology Conference, Virtual, 20-22 July. URTEC-2020-2948-MS. https://doi.org/10.15530/urtec-2020-2948.

Liu, Y., Wu, K., Jin, G., and Moridis, G. 2021a. Hydraulic-Fracture-Width Inversion Using Low-Frequency Distributed-Acoustic-Sensing Strain Data—Part I: Algorithm and Sensitivity Analysis. *SPE Journal* **26** (1): 359–371. SPE-204225-PA. https://doi.org/10.2118/204225-PA.

Liu, Y., Wu, K., Jin, G., and Moridis, G. 2021b. Hydraulic-Fracture-Width Inversion Using Low-Frequency Distributed-Acoustic-Sensing Strain Data Part II: Extension for Multifracture and Field Application. *SPE Journal* **26** (5): 2703–2715. SPE-205379-PA. https://doi.org/10.2118/205379-PA.

Malone, T. W., Rus, A., and Laubacher, R. 2020. Artificial intelligence and the future of work. Massachusetts Institute of Technology Report.

Mantell, M. E., Mercer, A., Jackson, J. B., Murphy, D. J., Conaway, J., Machovoe, S. R., Stokes, J., and Elliott, M. 2022. Application of Disposable Fiber Technology to Evaluate Far-Field Communication and Fracture Performance in the Marcellus Shale. Paper presented at the SPE Hydraulic Fracturing Technology Conference and Exhibition, The Woodlands, Texas, USA, 1-3 February. SPE-209148-MS. https://doi.org/10.2118/209148-MS.

Mateeva, A., Lopez, J., Potters, H., Mestayer, J., Cox, B., Kiyashchenko, D., Wills, P., Grandi, S., Hornman, K., Kuvshinov, B., Berlang, W., Yang, Z., and Detomo, R. 2014. Distributed acoustic sensing for reservoir monitoring with vertical seismic profiling. *Geophysical Prospecting* **62** (4): 679-692. https://doi.org/10.1111/1365-2478.12116.

McKimmy, M., Hari-Roy, S., Cipolla, C., Wolters, J., Jackson, H., and Kyle, H. 2022. Hydraulic Fracture Geometry, Morphology, and Parent-Child Interactions: Bakken Case Study. Paper presented at the SPE Hydraulic Fracturing Technology Conference and Exhibition, The Woodlands, Texas, USA, 1-3 February. SPE-209162-MS. https://doi.org/10.2118/209162-MS.

Molenaar, M. M., Hill, D. J., Webster, P., Fidan, E., and Birch, B. 2012. First Downhole Application of Distributed Acoustic Sensing for Hydraulic-Fracturing Monitoring and Diagnostics. *SPE Drilling and Completion* **27** (1): 32–38. SPE-140561-PA. https://doi.org/10.2118/140561-PA.

Olson, J. E. 1990. *Fracture mechanics analysis of joints and veins. PhD Dissertation*, Stanford University, Stanford, California (December 1990).

Pakhotina, J., Sakaida, S., Zhu, D., and Hill, A. D. 2020. Diagnosing Multistage Fracture Treatments with Distributed Fiber-Optic Sensors. *SPE Production & Operations* **35** (4): 852–864. SPE-199723-PA. https://doi.org/10.2118/199723-PA.

Raterman, K. T., Farrell, H. E., Mora, O. S., Janssen, A. L., Gomez, G. A., Busetti, S., McEwen, J., Friehauf, K., Rutherford, J., Reid, R., Jin, G., Roy, B., and Warren, M. 2018. Sampling a Stimulated Rock Volume: An Eagle Ford Example. *SPE Res Eval & Eng* **21** (4): 927–941. SPE-191375-PA. https://doi.org/10.2118/191375-PA.

Richter, P., Parker, T., Woerpel, C., Wu, W., Rufino, R., and Farhadiroushan, M. 2019. Hydraulic fracture monitoring and optimization in unconventional completions using a high-resolution engineered fibre-optic Distributed Acoustic Sensor. *First Break* **37** (4): 63-68. https://doi.org/10.3997/1365-2397.n0021.

Romberg, E., Adams, A., Edwards, J., and Levon, T. 2021. Natural Fracture Dominated Distribution of Slurry During a Multi-Cluster Hydraulic Fracturing Stage: A Marcellus DAS/DTS Case Study. Paper presented at the SPE Hydraulic Fracturing Technology Conference and Exhibition, Virtual, 4-6 May. SPE-204192-MS. https://doi.org/10.2118/204192-MS.

Roudakov, V. and Rohwer, C. 2006. Successful Hydraulic Fracturing Techniques in Horizontal Wells for Sandstone Formations in the Permian Basin. Paper presented at the SPE Russian Oil and Gas Technical Conference and Exhibition, Moscow, Russia, 3-6 October. SPE-102370-MS. https://doi.org/10.2118/102370-MS.

Salah, M., Gabry, M., and El-Sebaee, M. 2017. Evaluation of Multistage Fracturing Stimulation Horizontal Well Completion Methods in Western Desert, Egypt. Paper presented at the SPE Middle East Oil & Gas Show and Conference, Manama, Kingdom of Bahrain, 6-9 March. SPE-183785-MS. https://doi.org/10.2118/183785-MS.

Samuel, A. L. 1967. Some Studies in Machine Learning Using the Game of Checkers. II—Recent Progress. *IBM Journal of Research and Development* **11** (6): 601-617. https://doi.org/10.1147/rd.116.0601.

Schofield, J., Rodriguez-Herrera, A., and Garcia-Teijeiro, X. 2015. Optimization of Well Pad & Completion Design for Hydraulic Fracture Stimulation in Unconventional Reservoirs. Paper presented at the EUROPEC, Madrid, Spain, 1-4 June. SPE-174332-MS. https://doi.org/10.2118/174332-MS.

Shahri, M., Tucker, A., Rice, C., Lathrop, Z., Ratcliff, D., McClure, M., and Fowler G. 2021. High Fidelity Fibre-Optic Observations and Resultant Fracture Modeling in Support of Planarity. Paper presented at the SPE Hydraulic Fracturing Technology Conference and Exhibition, Virtual, 4-6 May. SPE-204172-MS. https://doi.org/10.2118/204172-MS.

Sherman, C., Mellors, R., Morris, J., and Ryerson, F. 2019. Geomechanical modeling of distributed fiber-optic sensor measurements. *Interpretation* **7** (1): SA21-SA27. https://doi.org/10.1190/INT-2018-0063.1.

Silixa. 2019. Introduction to Distributed Sensing. https://silixa.com/ (accessed September 2019).

Sneddon, I. N. 1946. The distribution of stress in the neighbourhood of a crack in an elastic solid. *Proceedings of the Royal Society of London Series A* **187** (1009): 229–260. https://doi.org/10.1098/rspa.1946.0077.

Taleghani, A. D. and Olson, J. E. 2014. How Natural Fractures Could Affect Hydraulic-Fracture Geometry. *SPE Journal* **19** (1): 161–171. SPE-167608-PA. https://doi.org/10.2118/167608-PA.

Tan, Y., Wang, S., Rijken, M. C. M., Hughes, K., Ning, I. L. C., Zhang, Z., and Fang, Z. 2021. Geomechanical Template for Distributed Acoustic Sensing Strain Patterns during Hydraulic Fracturing. *SPE Journal* **26** (2): 627–638. SPE-201627-PA. https://doi.org/10.2118/201627-PA.

Ugueto, G. A., Todea, F., Daredia, T., Wojtaszek, M., Huckaabee, P. T., Reynolds, A., Liang, C., and Chavarria, J. A. 2019. Can You Feel the Strain? DAS Strain Fronts for Fracture Geometry in the BC Montney, Groundbirch. Paper presented at the SPE Annual Technical Conference and Exhibition, Calgary, Alberta, Canada, 30 September-2 October. SPE-195943-MS. https://doi.org/10.2118/195943-MS.

Ugueto, G. A., Haffener, J., Mondal, S., Satviski, A. A., Huckabee, P. T., and Haustveit, K. 2022. Spatial and Temporal Effects on Low Frequency DAS and Microseismic Implications on Hydraulic Fracture Geometry and Well Interactions. Paper presented at the SPE Hydraulic Fracturing Technology Conference and Exhibition, The Woodlands, Texas, USA, 1-3 February. SPE-209180-MS. https://doi.org/10.2118/209180-MS.

Valkó, P. and Economides, M. J. 1995. *Hydraulic fracture mechanics*, first edition. Chichester, England: John Wiley & Sons.

Wang, J., Tan, Y., Rijken, P., Liu, X., Singh, A., and Li, Y. 2021. Observations and Modeling of Fiber-Optics Strain on Hydraulic Fracture Height Growth in HFTS-2. Paper presented at the SPE/AAPG/SEG Unconventional Resources Technology Conference, Houston, Texas, USA, 26-28 July. URTEC-2021-5295-MS. https://doi.org/10.15530/urtec-2021-5295.

Weijers, L., Wright, C., Mayerhofer, M., Pearson, M., Griffin, L., and Weddle, P. 2019. Trends in the North American Frac Industry: Invention through the Shale Revolution. Paper presented at the SPE Hydraulic Fracturing Technology Conference and Exhibition, The Woodlands, Texas, USA, 5-7 February. SPE-194345-MS. https://doi.org/10.2118/194345-MS.

White, M., Friehauf, K., Cramer, D., Constantine, J., Zhang, J., Schmidt, S., Long, J., Mislan, P., Spencer, J., Meier, P., and Davis, E. 2020. One Stage Forward or Two Stages Back, What are We Treating? Identification of Internal Casing Erosion During Hydraulic Fracturing - A Montney Case Study Using Ultrasonic and Fiber-Optic Diagnostics. Paper presented at the SPE Annual Technical Conference and Exhibition, Virtual, 27-29 October. SPE-201734-MS. https://doi.org/10.2118/201734-MS.

Wiley, C., Barree, B., Eberhard, M., and Lantz, T. 2004. Improved Horizontal Well Stimulations in the Bakken Formation, Williston Basin, Montana. Paper presented at the SPE Annual Technical Conference and Exhibition, Houston, Texas, 26-29 September. SPE-90697-MS. https://doi.org/10.2118/90697-MS.

Wu, K. 2014. *Numerical modeling of complex hydraulic fracture development in unconventional reservoirs. PhD Dissertation*, The University of Texas at Austin, Austin, Texas (December 2014).

Wu, Y., Hull, R., Tucker, A., Rice, C., Richter, P., Wygal, B., Farhadiroushan, M., Trujillo, K., and Woerpel, C. 2021. Hydraulic Fracturing Diagnostics Utilizing Near and Far-Field Distributed Acoustic Sensing DAS Data Correspondences. Presented at the SPE Hydraulic Fracturing Technology Conference and Exhibition, Virtual, 4-6 May. SPE-204205-MS. https://doi.org/10.2118/204205-MS.

Yao, B. and Yang, H. 2016. Physics-driven Spatiotemporal Regularization for High-dimensional Predictive Modeling: A Novel Approach to Solve the Inverse ECG

Problem. *Scientific Reports* **6** (1): article number 39012. https://doi.org/10.1038/srep39012.

Zang, C., Jiang, H., Shi, S., Li, J., Zou, Y., Zhang, S., Tian, G., and Yang, P. 2022. An analysis of the uniformity of multi-fracture initiation based on downhole video imaging technology: A case study of Mahu tight conglomerate in Junggar Basin, NW China. *Petroleum Exploration and Development* **49** (2): 448-457. https://doi.org/10.1016/S1876-3804(22)60038-7.

Zhang, Z., Fang, Z., Stefani, J., DiSiena, J., Bevc, D., Ning, I. L. C., Hughes, K., and Tan, Y. 2020. Fiber Optic Strain Monitoring of Hydraulic Stimulation: Geomechanical Modeling and Sensitivity Analysis. Paper presented at the SPE/AAPG/SEG Unconventional Resources Technology Conference, Virtual, 20-22 July. URTEC-2020-2648-MS. https://doi.org/10.15530/urtec-2020-2648.

APPENDIX A

DISPLACEMENT DISCONTINUITY METHOD SUPPLEMENTARY EQUATIONS

Coordinate Transformation

Let xy be the global coordinate, and $\bar{x}\bar{y}$ (shear-normal) the local coordinate (**Figure A. 1**). The transformation of displacement and stress from global to local coordinate system can be done using the following equations:

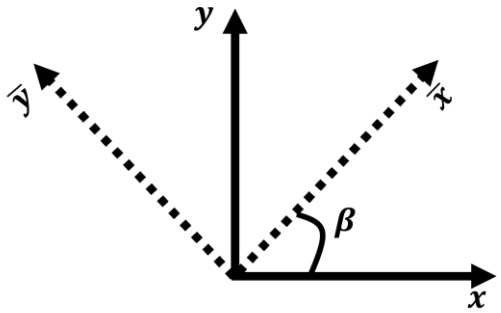

Figure A. 1–Global (xy) and local ($\bar{x}\bar{y}$) coordinate systems separated by the angle β.

Displacement

$$u_{\bar{x}} = u_x cos\beta + u_y sin\beta \,, \tag{A.1}$$

$$u_{\bar{y}} = -u_x sin\beta + u_y cos\beta \,, \tag{A.2}$$

Stress

$$\sigma_{\bar{x}\bar{x}} = \sigma_{xx} cos^2\beta + 2\sigma_{xy} sin\beta cos\beta + \sigma_{yy} sin^2\beta \,, \tag{A.3}$$

$$\sigma_{\bar{y}\bar{y}} = \sigma_{xx} sin^2\beta - 2\sigma_{xy} sin\beta cos\beta + \sigma_{yy} cos^2\beta \,, \tag{A.4}$$

$$\sigma_{\bar{x}\bar{y}} = -(\sigma_{xx} - \sigma_{yy}) sin\beta cos\beta + \sigma_{xy}(cos^2\beta - sin^2\beta) \,. \tag{A.5}$$

Boundary Influence Coefficients for Stress

$$A_{ns} = 2G[2f_{xy} sin^2\beta + f_{xx} sin2\beta - y(f_{xyy} cos2\beta + f_{yyy} sin2\beta)] \,, \tag{A.6}$$

$$A_{nn} = 2G[f_{yy} + y(f_{xyy}sin2\beta - f_{yyy}cos2\beta)]\,, \tag{A.7}$$

$$A_{ss} = 2G[-f_{xy}sin2\beta + f_{yy}cos2\beta - y(f_{xyy}sin2\beta - f_{yyy}cos2\beta)]\,, \tag{A.8}$$

$$A_{sn} = 2G\big[-y\big(f_{xyy}cos2\beta + f_{yyy}sin2\beta\big)\big]\,, \tag{A.9}$$

Where G is the shear modulus and can be calculated by:

$$G = \frac{E}{2(1+\upsilon)}\,. \tag{A.10}$$

Displacement and Stress in the Infinite/Elastic Body

Displacement

$$\begin{aligned} u_x^i = \sum_{j=1}^{N} & D_{\bar{x}}^j\big[2(1-\upsilon)f_y cos\beta - (1-2\upsilon)f_x sin\beta + y\big(f_{xy}sin\beta + f_{yy}cos\beta\big)\big] \\ & + D_{\bar{y}}^j\big[-(1-2\upsilon)f_x cos\beta - 2(1-\upsilon)f_y sin\beta + y\big(-f_{xy}cos\beta + f_{yy}sin\beta\big)\big]\,, \end{aligned} \tag{A.11}$$

$$\begin{aligned} u_y^i = \sum_{j=1}^{N} & D_{\bar{x}}^j\big[2(1-\upsilon)f_y sin\beta + (1-2\upsilon)f_x cos\beta - y\big(f_{xy}cos\beta + f_{xx}sin\beta\big)\big] \\ & + D_{\bar{y}}^j\big[-(1-2\upsilon)f_x sin\beta + 2(1-\upsilon)f_y cos\beta + y\big(-f_{xy}sin\beta + f_{xx}cos\beta\big)\big]\,, \end{aligned} \tag{A.12}$$

Stress

$$\begin{aligned} \sigma_{xx}^i = 2G\sum_{j=1}^{N} & D_{\bar{x}}^j\big[2f_{xy}cos^2\beta + f_{xx}sin2\beta + y\big(f_{xyy}cos2\beta - f_{yyy}sin2\beta\big)\big] \\ & + D_{\bar{y}}^j\big[f_{yy} + y(f_{xyy}sin2\beta + f_{yyy}cos2\beta)\big]\,, \end{aligned} \tag{A.13}$$

$$\begin{aligned} \sigma_{yy}^i = 2G\sum_{j=1}^{N} & D_{\bar{x}}^j\big[2f_{xy}sin^2\beta + f_{yy}sin2\beta - y\big(f_{xyy}cos2\beta - f_{yyy}sin2\beta\big)\big] \\ & + D_{\bar{y}}^j\big[f_{yy} - y(f_{xyy}sin2\beta + f_{yyy}cos2\beta)\big]\,, \end{aligned} \tag{A.14}$$

$$\begin{aligned} \sigma_{xy}^i = 2G\sum_{j=1}^{N} & D_{\bar{x}}^j\big[f_{xy}sin2\beta + f_{yy}cos2\beta + y\big(f_{xyy}sin2\beta + f_{yyy}cos2\beta\big)\big] \\ & + D_{\bar{y}}^j\big[-y(f_{xyy}cos2\beta - f_{yyy}sin2\beta)\big]\,. \end{aligned} \tag{A.15}$$

APPENDIX B

MODELING OF STRAIN FIELDS INCORPORATING HYDRAULIC AND NATURAL FRACTURE INTERACTIONS

I have modeled strain and strain rate responses of scenarios comprised by hydraulic and natural fractures considering two additional sensitivity analyses. The first sensitivity analysis with 3 different scenarios is performed varying natural fracture distribution and keeping constant its orientation (strike in 3D mode) and length. In this case the simulation accounts for 5, 10 and 20 natural fractures per cluster with ±40° orientation and 16.3 ft long. **Figure B. 1** presents adopted geometry of all 3 scenarios (*a*, *b* and *c*).

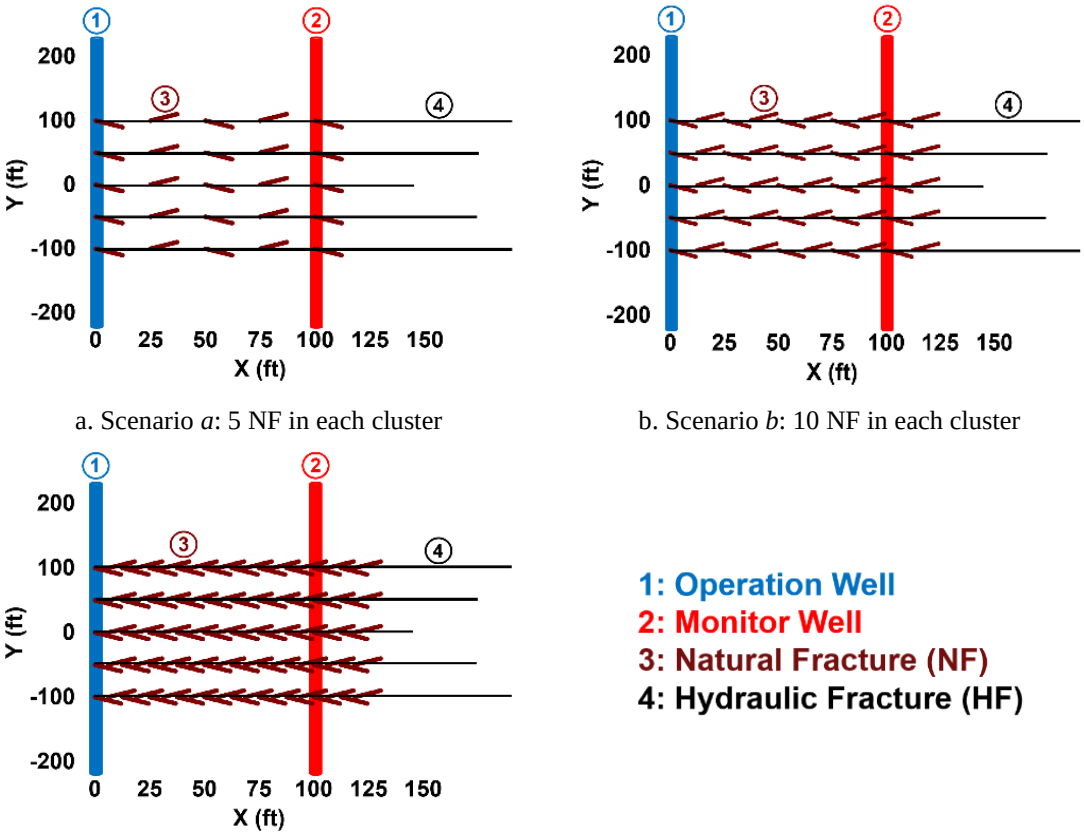

a. Scenario *a*: 5 NF in each cluster

b. Scenario *b*: 10 NF in each cluster

c. Scenario *c*: 20 NF in each cluster

Figure B. 1–Map view of lateral section of horizontal wells varying the number of NF.

DSS and LF-DAS modeling results of first sensitivity analysis are shown in **Figure B. 2**.

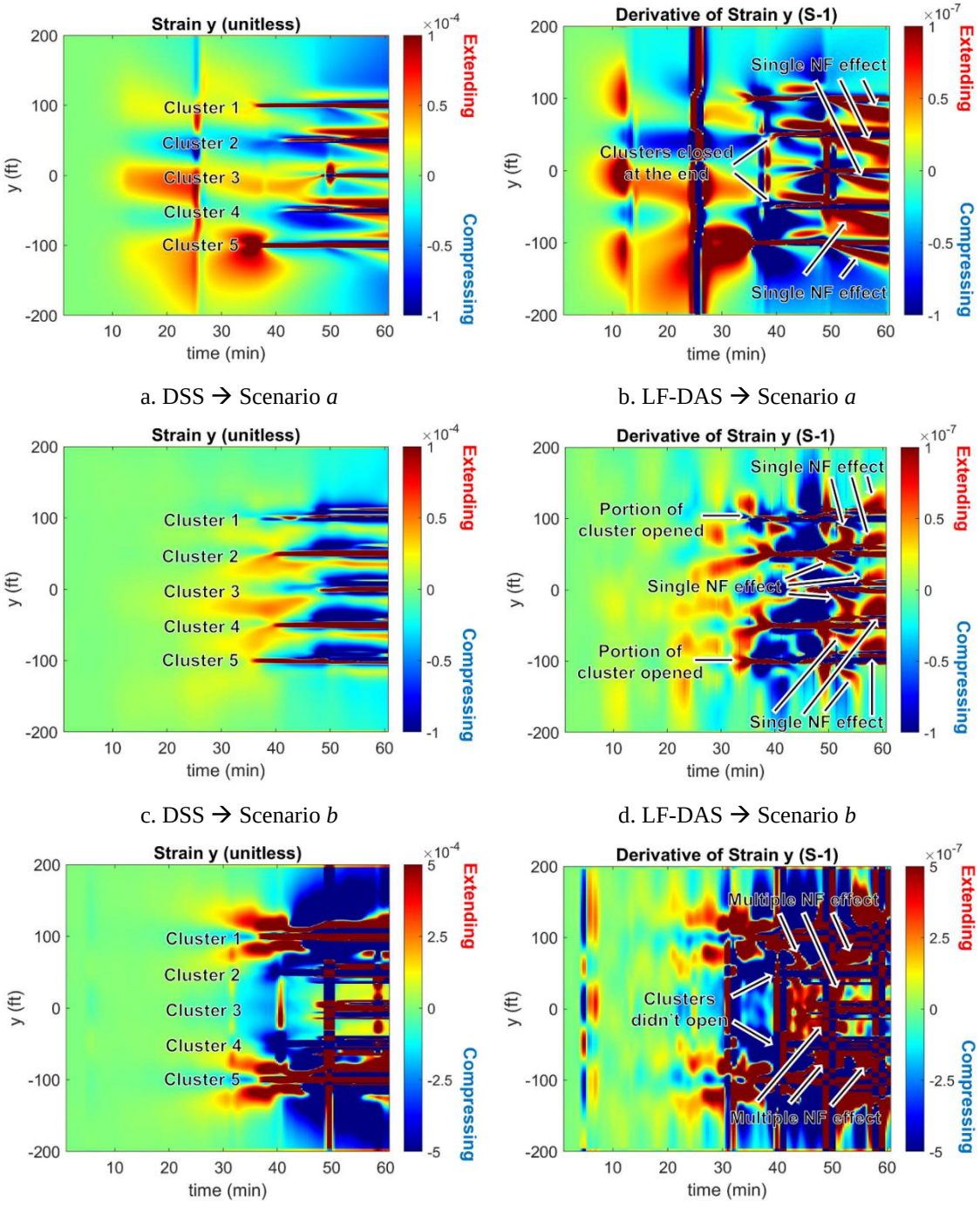

a. DSS → Scenario *a*

b. LF-DAS → Scenario *a*

c. DSS → Scenario *b*

d. LF-DAS → Scenario *b*

e. DSS → Scenario *c*

f. LF-DAS → Scenario *c*

Figure B. 2–DSS and LF-DAS modeling results of sensitivity analysis varying the number of NF.

DSS/LF-DAS waterfall plots in **Figure B. 2** present a great level of complexity compared to base case scenario (**Figure 3.9**) and generation of throughgoing hydraulic fractures from different clusters are affected by natural fractures.

Evaluation of LF-DAS results in **Figure B. 2** reveals the following aspects:

1. Scenarios *a* and *b*: For relatively small number of natural fractures in each perforation cluster (i.e., 5 or 10), geometrical details of such fractures are distinguishable in waterfall plots.
2. Scenario *c*: Increasing natural fracture distribution culminates in very complex outcomes to the point that fracture hits are difficult to be identified in waterfall plot. Therefore, sum of strain rate can be used as a tool to assist determining perforation cluster location (**Figure B. 3**). It is suspected that waterfall plot presents the commingle extension response of multiple natural fractures (lack of spatial resolution). It is important to mention that the magnitude of strain results increases in scenario *c*, therefore to avoid high saturation in **Figure B. 2e** and **Figure B. 2f** , I increase the magnitude of maximum and minimum limits of color bar.

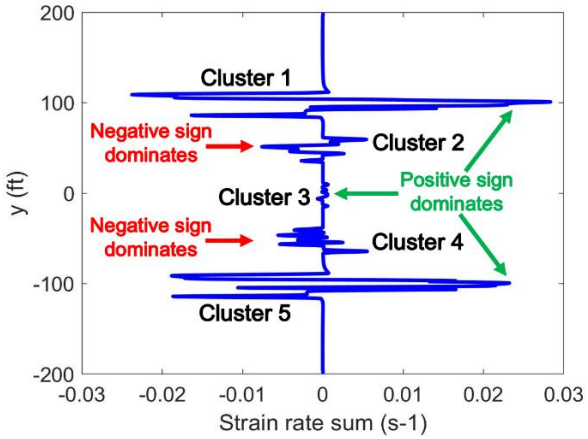

Figure B. 3–Strain rate sum for scenario *c* of sensitivity analysis varying the number of NF. Spikes aid determining cluster location.

I include complexity in the study by the design of a new environment with clusters composed by natural fractures with variable orientation. Natural fractures in clusters 1, 3 and 5 have ±50° and ±65° orientation angles while ±40° and ±55° in clusters 2 and 4.

The second sensitivity analysis with 4 different scenarios is performed varying natural fracture length and keeping constant its orientation (strike in 3D mode) and distribution. In this case the simulation accounts for 10 natural fractures per cluster with orientation as mentioned in the previous paragraph and length ranging from 2.8 ft to 29.6 ft. **Figure B. 4** presents adopted geometry of all 4 scenarios (*a*, *b*, *c* and *d*).

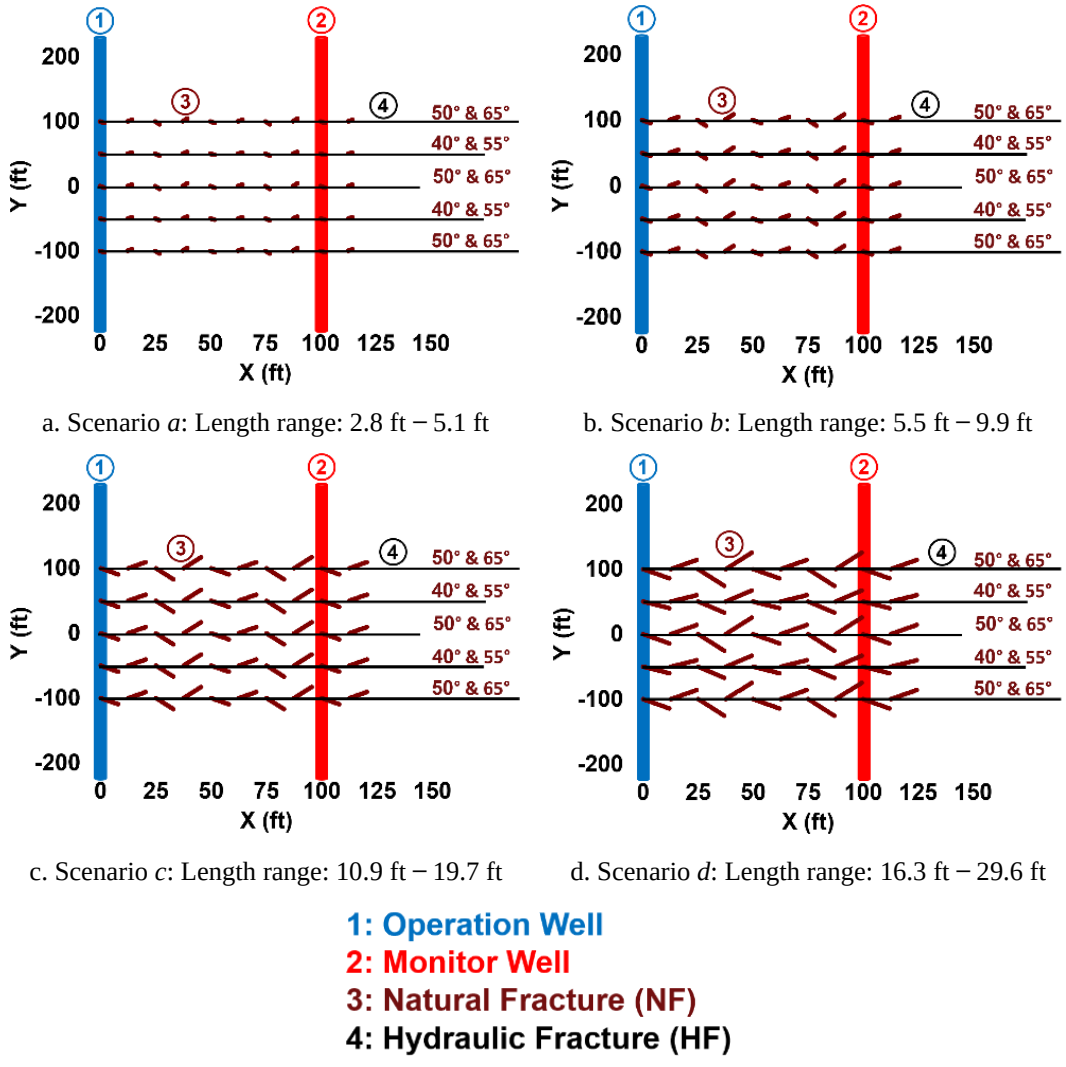

a. Scenario *a*: Length range: 2.8 ft − 5.1 ft

b. Scenario *b*: Length range: 5.5 ft − 9.9 ft

c. Scenario *c*: Length range: 10.9 ft − 19.7 ft

d. Scenario *d*: Length range: 16.3 ft − 29.6 ft

Figure B. 4–Map view of lateral section of horizontal wells varying NF length.

DSS and LF-DAS modeling results of second sensitivity analysis are shown in **Figure B. 5**.

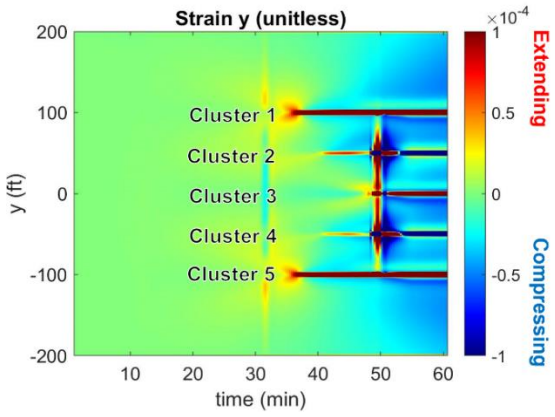

a. DSS → Scenario *a*

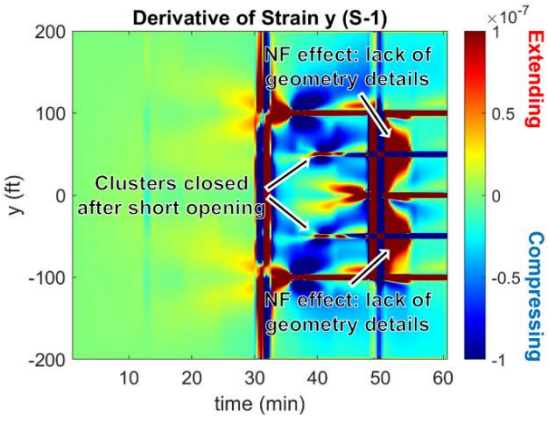

b. LF-DAS → Scenario *a*

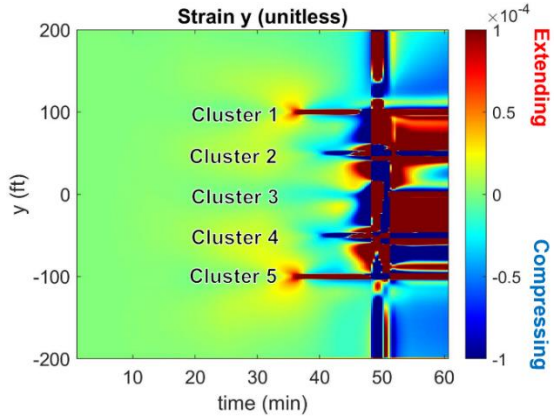

c. DSS → Scenario *b*

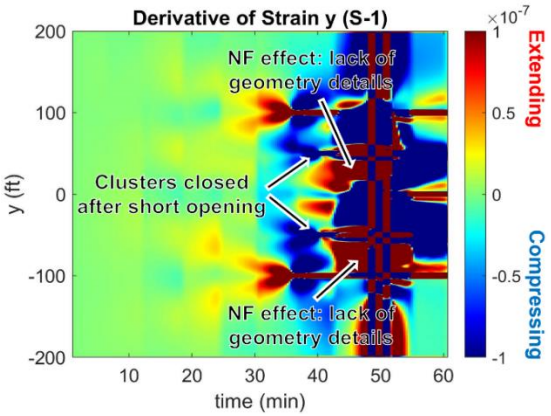

d. LF-DAS → Scenario *b*

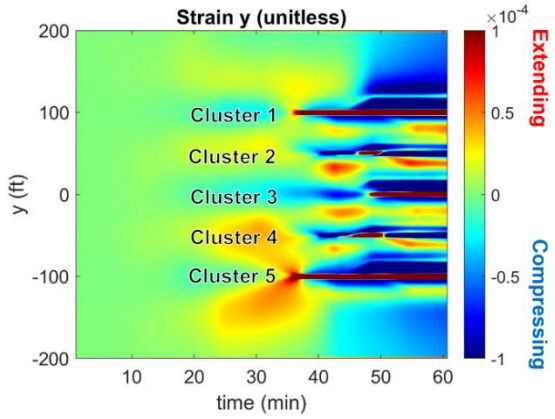

e. DSS → Scenario *c*

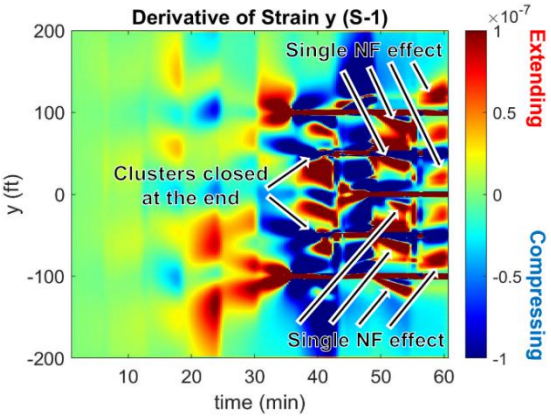

f. LF-DAS → Scenario *c*

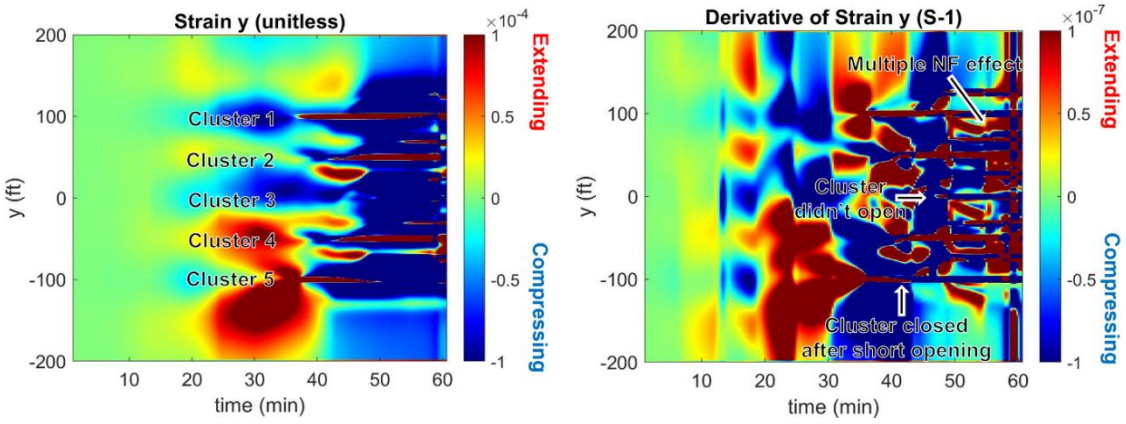

g. DSS → Scenario *d*

h. LF-DAS → Scenario *d*

Figure B. 5–DSS and LF-DAS modeling results of sensitivity analysis varying NF length.

Similarly to DSS/LF-DAS results obtained in the first sensitivity analysis, DSS/LF-DAS waterfall plots in the second sensitivity analysis (**Figure B. 5**) indicate that natural fractures have the potential to impact the generation of throughgoing hydraulic fractures from different clusters. Furthermore, the outcome of scenario *a* with shortest natural fractures does not exhibit great complexity compared with results of scenarios *b*, *c* and *d*.

Evaluation of LF-DAS results in **Figure B. 5** reveals the following aspects:

1. Scenarios *a* and *b*: Geometry details of natural fractures are not noticed in waterfall plots. It is suspected that natural fractures are too short that available spatial resolution is not enough to detect it.
2. Scenario *c*: Geometrical peculiarities of natural fractures are observed in waterfall plot, which is believed to be a result of natural fracture length increase to the point that available spatial resolution can detect it.
3. Scenario *d*: Shape of natural fractures cannot be clearly identified. It is suspected that as length increase to a certain degree, natural fractures of adjacent clusters will get close and consequently waterfall plot will tend to present commingle extension response of multiple natural fractures (lack of spatial resolution).

APPENDIX C

MONITOR WELL SENSITIVITY TO STRAIN SIGNAL ARRIVALS

This case is dedicated to study monitor well sensitivity to strain signal arrivals. The distance between monitor and operation wells is varied from 50 to 150 ft in intervals of 25 ft. Details regarding natural fracture distribution and geometry are described in **Table C. 1** and shown schematically in **Figure C. 1**.

Table C. 1–Natural fractures details.

Density per cluster	Length range	Orientation angle in clusters 1, 3 and 5	Orientation angle in clusters 2 and 4
10	16.3 – 29.6 ft	±50° and ±65°	±40° and ±55°

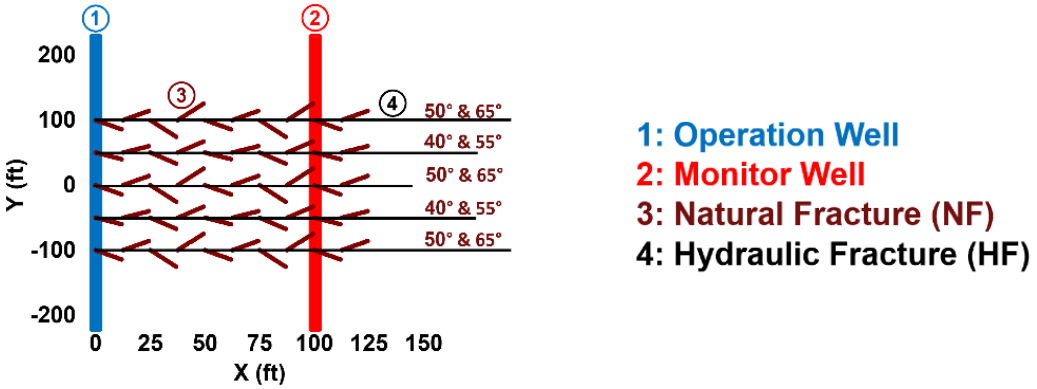

Figure C. 1–Map view of lateral section of horizontal wells showing a particular configuration with 100 ft well distance.

Figure C. 2 shows absolute strain and strain rate results for a simulation time span of 1 hour, which considers 5 different configuration distances between observation and treatment wells: 50, 75, 100, 125 and 150 ft. I observe a great level of complexity associated with the time history plots, which may have a relevant contribution of reactivation of planar discontinuities failing in shear mode. Moreover, I suspect that such complexities are detected as a consequence of the small gauge length (i.e., on the order of 1 m) applied in simulations.

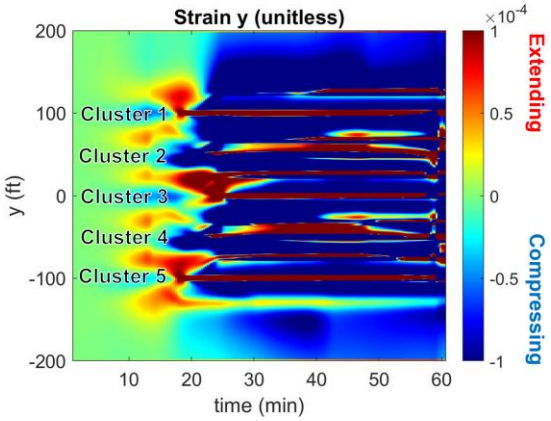

a. DSS → 50 ft well distance

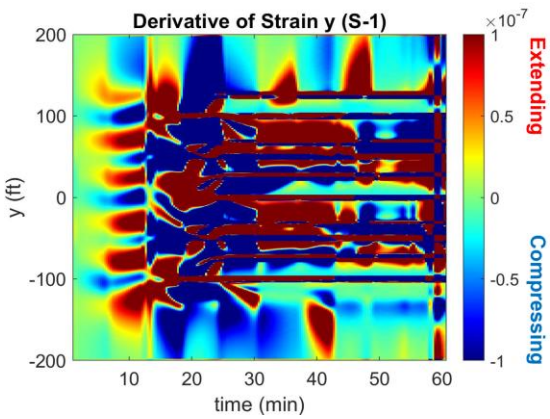

b. LF-DAS → 50 ft well distance

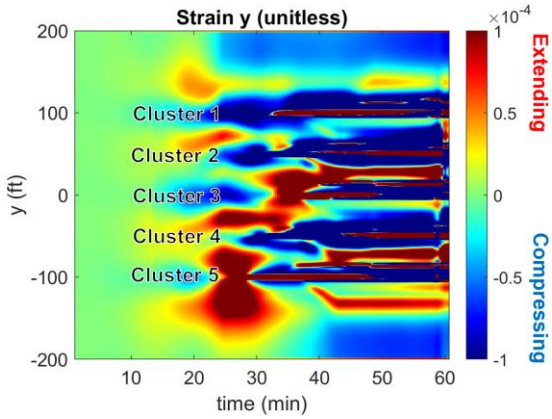

c. DSS → 75 ft well distance

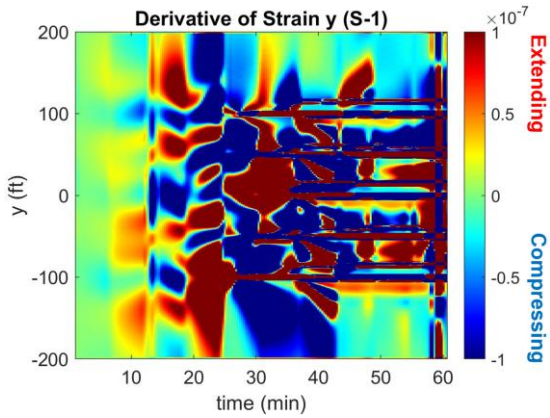

d. LF-DAS → 75 ft well distance

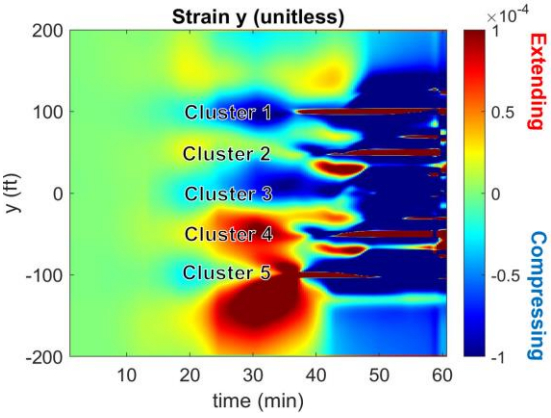

e. DSS → 100 ft well distance

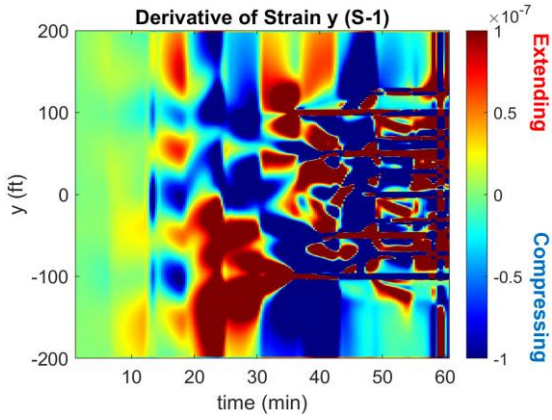

f. LF-DAS → 100 ft well distance

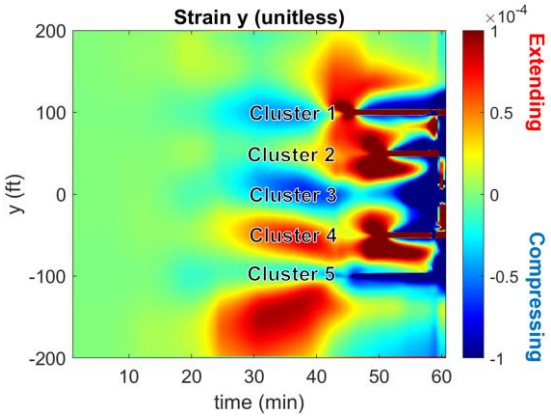

g. DSS → 125 ft well distance

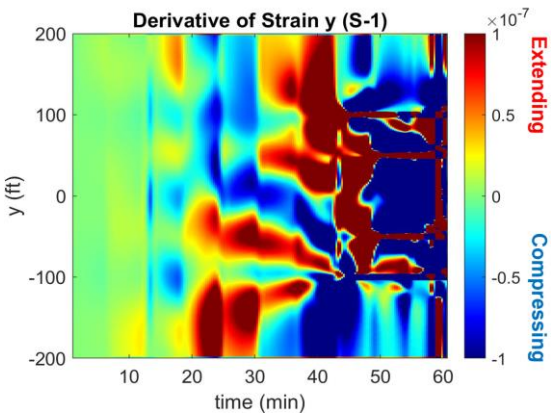

h. LF-DAS → 125 ft well distance

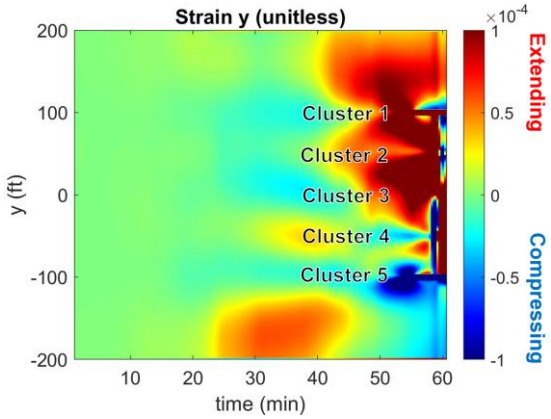

i. DSS → 150 ft well distance

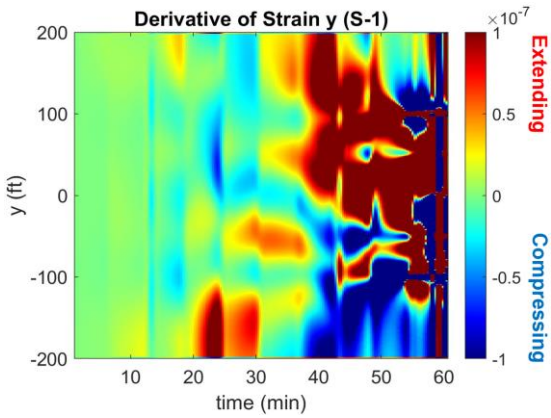

j. LF-DAS → 150 ft well distance

Figure C. 2–DSS and LF-DAS results varying distance between monitor and operation wells.

Comparing all 5 simulations, I note that extension and compression phenomenon as a consequence of fracture opening and slippage, are first identified in the case where distance between monitor and operation wells is the shortest (i.e., 50 ft) as seen in **Figure C. 2a** and **Figure C. 2b**. On the other hand, such attributes related to fracture propagation start to be observed lastly in the simulation where the distance between both wells is the largest (i.e., 150 ft), and consequently hydraulic fractures take the longest time to approach monitor well as seen in **Figure C. 2i** and **Figure C. 2j**. Therefore, I infer that DSS and LF-DAS responses obtained using the numerical technique are sensitive to a region near the monitor well, which is in accordance with the same type of data acquired by fiber-optics in the field (Wu et al., 2021).